



**NAVAL
POSTGRADUATE
SCHOOL**

MONTEREY, CALIFORNIA

THESIS

**QUANTIFYING SEASONAL SKILL IN COUPLED SEA
ICE MODELS USING FREEBOARD MEASUREMENTS
FROM SPACEBORNE LASER ALTIMETERS**

by

Kristine N. Bench

June 2016

Thesis Advisor:

Second Reader:

Andrew Roberts

Wieslaw Maslowski

Approved for public release; distribution is unlimited

THIS PAGE INTENTIONALLY LEFT BLANK

REPORT DOCUMENTATION PAGE			<i>Form Approved OMB No. 0704-0188</i>
<p>Public reporting burden for this collection of information is estimated to average 1 hour per response, including the time for reviewing instruction, searching existing data sources, gathering and maintaining the data needed, and completing and reviewing the collection of information. Send comments regarding this burden estimate or any other aspect of this collection of information, including suggestions for reducing this burden, to Washington headquarters Services, Directorate for Information Operations and Reports, 1215 Jefferson Davis Highway, Suite 1204, Arlington, VA 22202-4302, and to the Office of Management and Budget, Paperwork Reduction Project (0704-0188) Washington, DC 20503.</p>			
1. AGENCY USE ONLY (Leave blank)	2. REPORT DATE June 2016	3. REPORT TYPE AND DATES COVERED Master's thesis	
4. TITLE AND SUBTITLE QUANTIFYING SEASONAL SKILL IN COUPLED SEA ICE MODELS USING FREEBOARD MEASUREMENTS FROM SPACEBORNE LASER ALTIMETERS		5. FUNDING NUMBERS	
6. AUTHOR(S) Kristine N. Bench		8. PERFORMING ORGANIZATION REPORT NUMBER	
7. PERFORMING ORGANIZATION NAME(S) AND ADDRESS(ES) Naval Postgraduate School Monterey, CA 93943-5000		10. SPONSORING / MONITORING AGENCY REPORT NUMBER	
9. SPONSORING /MONITORING AGENCY NAME(S) AND ADDRESS(ES) N/A		12a. DISTRIBUTION / AVAILABILITY STATEMENT Approved for public release; distribution is unlimited	
11. SUPPLEMENTARY NOTES The views expressed in this thesis are those of the author and do not reflect the official policy or position of the Department of Defense or the U.S. Government. IRB Protocol number <u>N/A</u> .			
12b. DISTRIBUTION CODE			
13. ABSTRACT (maximum 200 words) <p>Satellites and several specially equipped scientific aircraft provide basin-wide altimetric measurements of sea ice freeboard, from which sea ice thickness can be estimated. Up to now, few methods have been developed to use these measurements to quantitatively assess the skill of predictive models of sea ice for the Arctic. This thesis addresses this problem, using measured freeboard from ICESat and Operation IceBridge (OIB). Output from the Regional Arctic System Model (RASM) is used to demonstrate applicability of both variance- and correlation-weighted skill scores of freeboard that quantify model skill and take measurement error into account. The techniques are demonstrated using two different RASM configurations, one using Elastic-Viscous-Plastic (EVP) ice mechanics, the other using the Elastic-Anisotropic-Plastic (EAP) rheology, both simulated for 2004 and 2007, during which ICESat was in operation. RASM variance skill scores ranged from 0.712 to 0.824 and correlation skill scores were between 0.319 and 0.511. The skill scores were calculated for monthly periods and require little adaption to be applicable for monthly to decadal Navy forecasts of the Arctic. This will help improve sea ice prediction by quantifying model limitations and thus maximize the usefulness of ICESat-2 freeboard measurements after that satellite is launched next year.</p>			
14. SUBJECT TERMS Arctic, climate change, Regional Arctic System Model, altimetry measurements, sea ice, sea ice thickness, freeboard, ICESat, ICESat-2, climate model, coupled model, Operation IceBridge		15. NUMBER OF PAGES 147	16. PRICE CODE
17. SECURITY CLASSIFICATION OF REPORT Unclassified	18. SECURITY CLASSIFICATION OF THIS PAGE Unclassified	19. SECURITY CLASSIFICATION OF ABSTRACT Unclassified	20. LIMITATION OF ABSTRACT UU

NSN 7540-01-280-5500

Standard Form 298 (Rev. 2-89)
Prescribed by ANSI Std. Z39-18

THIS PAGE INTENTIONALLY LEFT BLANK

Approved for public release; distribution is unlimited

**QUANTIFYING SEASONAL SKILL IN COUPLED SEA ICE MODELS USING
FREEBOARD MEASUREMENTS FROM SPACEBORNE LASER ALTIMETERS**

Kristine N. Bench
Lieutenant, United States Navy
B.S., United States Naval Academy, 2006

Submitted in partial fulfillment of the
requirements for the degree of

**MASTER OF SCIENCE IN METEOROLOGY AND PHYSICAL
OCEANOGRAPHY**

from the

NAVAL POSTGRADUATE SCHOOL
June 2016

Approved by: Andrew Roberts
Thesis Advisor

Wieslaw Maslowski
Second Reader

Peter Chu
Chair, Department of Oceanography

THIS PAGE INTENTIONALLY LEFT BLANK

ABSTRACT

Satellites and several specially equipped scientific aircraft provide basin-wide altimetric measurements of sea ice freeboard, from which sea ice thickness can be estimated. Up to now, few methods have been developed to use these measurements to quantitatively assess the skill of predictive models of sea ice for the Arctic. This thesis addresses this problem, using measured freeboard from ICESat and Operation IceBridge (OIB). Output from the Regional Arctic System Model (RASM) is used to demonstrate applicability of both variance- and correlation-weighted skill scores of freeboard that quantify model skill and take measurement error into account. The techniques are demonstrated using two different RASM configurations, one using Elastic-Viscous-Plastic (EVP) ice mechanics, the other using the Elastic-Anisotropic-Plastic (EAP) rheology, both simulated for 2004 and 2007, during which ICESat was in operation. RASM variance skill scores ranged from 0.712 to 0.824 and correlation skill scores were between 0.319 and 0.511. The skill scores were calculated for monthly periods and require little adaption to be applicable for monthly to decadal Navy forecasts of the Arctic. This will help improve sea ice prediction by quantifying model limitations and thus maximize the usefulness of ICESat-2 freeboard measurements after that satellite is launched next year.

THIS PAGE INTENTIONALLY LEFT BLANK

TABLE OF CONTENTS

I.	INTRODUCTION.....	1
A.	WHY IS ARCTIC SEA ICE IMPORTANT?	4
1.	Arctic Sea Ice Characteristics.....	4
2.	Sea Ice Energy Balance	6
B.	CONSEQUENCES OF A CHANGING ARCTIC ENVIRONMENT.....	11
C.	UNITED STATES' INTEREST IN THE CHANGING ARCTIC ENVIRONMENT.....	14
D.	U.S. NAVY RELEVANCE.....	17
II.	PREVIOUS WORK ON SEA ICE.....	21
A.	ARCTIC SEA ICE THICKNESS.....	21
B.	SEA ICE THICKNESS UNCERTAINTY	25
C.	A BRIEF SUMMARY OF OBSERVATIONS AND MODELING OF THE ARCTIC	27
D.	ALTIMETRIC OBSERVATIONS.....	28
1.	ICESAT.....	29
2.	Operation IceBridge	33
3.	ICESat-2.....	35
E.	SEA ICE MODELS	36
1.	Advances in Sea Ice Modeling Since 1970	37
2.	LIMITATIONS OF COUPLED MODELS.....	44
3.	Los Alamos Sea Ice Model (CICE) and Its Use in This Study.....	45
F.	INTENT TO STUDY	46
III.	MODEL DESCRIPTION AND METHODS	49
A.	OBJECTIVE	49
B.	THE REGIONAL ARCTIC SYSTEM MODEL	49
C.	ICESAT-2 EMULATOR.....	53
D.	CHARACTERIZING SPATIAL RELATIONSHIPS IN FREEBOARD	57
E.	APPLYING THESE METHODS TO UNDERSTAND SKILL IN MODELS.....	60
IV.	BIAS IN OBSERVATIONS AND IN MODELS USING ALTIMETRICALLY DERIVED SEA ICE FREEBOARD.....	63
A.	OVERVIEW.....	63

B.	ICESAT-2 TEST EMULATOR	63
1.	ICESAT AND OIB SPECTRAL ANALYSIS	68
2.	Discussion.....	74
C.	INITIAL ICESAT EMULATOR RESULTS	75
D.	FINAL ICESAT/ICESAT-2 EMULATOR DESIGN— EXAMPLES FROM 2004 AND 2007	85
V.	CONCLUSION: METRICS FOR EVALUATING SEA ICE MODELS USING SATELLITE ALTIMETRY	97
A.	CULMINATION OF THIS THESIS: SKILL SCORES FOR SEA ICE MODELS USING LASER ALTIMETERS.....	97
B.	CONCLUSIONS	99
C.	RECOMMENDATIONS FOR FUTURE STUDIES.....	101
APPENDIX ADDITIONAL ICESAT-2 EMULATOR RESULTS		103
LIST OF REFERENCES		111
INITIAL DISTRIBUTION LIST		121

LIST OF FIGURES

Figure 1.	Northern Hemisphere extent anomalies, September 2015. Source: NSIDC (2016). The Northern Hemisphere sea ice extent for the month of September 2015 is declining at a rate of $-13.4 \pm 2.7\%$ per decade since the late 1970s. The mean sea ice extent is 6.5 million square kilometers.....	1
Figure 2.	Northern Hemisphere extent anomalies, March 2016. Source: NSIDC (2016). The Northern Hemisphere sea ice extent for the month of March 2016 is declining at a rate of $-2.7 \pm 0.5\%$ per decade since the late 1970s. The March mean sea ice extent is 15.5 million square kilometers.....	2
Figure 3.	A ridge and lead in the Beaufort Sea, March 2016. Figure 3a is an image of a pressure ridge in the Beaufort Sea. Figure 3b is an image of a developing lead, horizontally tilted.	5
Figure 4.	Sea ice ridges in the Beaufort Sea, March 2016. This image of a sea ice floe was captured north of Prudhoe Bay, Alaska, and depicts the development of a sea ice ridge.....	6
Figure 5.	Leads in sea ice in the Beaufort Sea, March 2016. This image of a sea ice floe is north of Prudhoe Bay, Alaska, and depicts leads between the floes.....	6
Figure 6.	Albedo of sea ice. Source: Perovich (1996). The scale represents the albedo of sea ice in differing physical states. Measurements were conducted by Perovich during a spring to summer season transition to observe the albedos associated with the changes in the physical states of sea ice.....	8
Figure 7.	Annual evolution of sea ice albedo. Source: Perovich and Polashenski (2012). Time series sea ice albedo from the winter season to fall freeze up. The red line represents first year ice and the seven associated phases. The blue line represents multi-year ice.....	9
Figure 8.	March sea ice categorized by age. Source: Perovich et al. (2015). Between the years 1981–2015, there has been a decline in multi-year ice and a shift to more first year ice.....	10
Figure 9.	Linear Trend (%/year) of solar heat flux into the Arctic Ocean. Source: Perovich (2007). The color scale represents average percent per year increase of heat input into the Arctic Ocean, with the largest increase in the Chukchi Sea.....	11

Figure 10. Arctic and global mean annual surface air temperature anomaly between the years 1900–2014. Source: NOAA (2016). The mean annual surface temperature, relative to the 1981–2010 mean, for the Arctic region has an increasing positive trend since the 1980s. The rate at which the Arctic surface temperatures are increasing is twice the rate of increase in global surface temperatures.....12

Figure 11. Trans-polar sea routes decreased sea ice extent. Source: Arctic Roadmap (2014). With the decline in sea ice, shipping routes through the Arctic Ocean may provide the opportunity for trans-polar maritime routes and increased maritime activities.13

Figure 12. Map of the Arctic nations. Source: National Science Foundation (1998). The United States, Canada, Russia, Norway, Denmark, Finland, Sweden, and Iceland are the eight Arctic nations that encircle the Arctic Ocean. Russia has the longest coastline in the region and about two-thirds of Canada's marine coastline lies within the Arctic.....15

Figure 13. Arctic territorial claims. Source: Encyclopedia Britannica (2010). The Arctic territorial claims by the Arctic States. The red line represents the 200 nautical miles EEZ as authorized by UNCLOS. Russia's proposed claim extends toward the North Pole, into international waters. Russia considers the Lomonosov ridge as an extension of the Siberian continental shelf.16

Figure 14. Russian Military Bases within the Arctic Circle since 2014. Source: Center for Strategic and International Studies (2015) and New York Times (2015). Russia has established an Arctic command with the intent of re-opening former airfields and bases.18

Figure 15. Central Arctic sea ice growth rates relative to ice thickness. Source: Thorndike et al. (1975). Sea ice growth rate, the thermodynamic thickening of sea ice, is dependent upon sea ice thickness. Thinner ice has a larger growth rate than perennial ice.....22

Figure 16. Monthly variation in sea ice growth rates for multi-year and first-year ice. Source: Thorndike et al. (1975). Thin sea ice responds to changes in the atmospheric heat fluxes faster than thicker ice for both the growth and melt phases. This is evident by the significantly larger growth and melt rates of thin ice, and earlier onset of each process, whereas the thicker ice responds to atmospheric fluxes at a much slower rate and at a later time period. The growth rate of thick sea ice does not increase until November, compared to thin ice, which begins the growth phase mid-August.....23

Figure 17.	The sea ice thickness distribution $g(h_i)$. Source: Hutchings et al. (2008). On April 5 and 9, 2007, an airborne LASER altimeter took measurements of sea ice freeboard, while an electromagnetic bird was used to detect its draft, thus deriving the sea ice thickness distribution along survey lines in the Beaufort Sea. Due to sea ice deformation, a change in sea ice thickness distribution, or redistribution, was observed between the two days.....	24
Figure 18.	Variables used in the estimation of sea ice thickness from freeboard, h_f , which is designated with the <i>fb</i> symbol throughout this thesis. Source: Teleti and Luis (2013).	25
Figure 19.	Snow depths along a sea ice transect in the Arctic, where the x-axis indicates transect distance in meters. Source: Warren et al. (1999). Snow measurements were conducted along a 1000-meter snow line in October 1985 and March 1986, representing the fall and winter seasons for snow accumulation. The mean snow depth for the winter is 28.9 cm, and for fall is 8.7 cm.....	26
Figure 20.	Depiction of ICESat collecting data along the orbital track. Source: NASA (2005). NASA's ICESat orbited the earth, using LASER to measure the travel time between the Earth's surface and the satellite. Along the path, the LASER path is affected by clouds, aerosols and differing surface types.....	30
Figure 21.	ICESat Surface Elevations for the 2009 fall orbital period. Source: NSIDC (2014). ICEat measured sea surface elevations across the polar regions along its orbital track. The color scale depicts surface elevation height in meters; white space is void of satellite coverage. Gaps in satellite coverage are noted by the break in ground tracks.....	31
Figure 22.	Airborne Topographic Mapper Scan 24 March 2013. Source: Andrew Roberts (2015). Figure (a) is the surface elevation measurements taken by the ATM aboard the OIB flight on 24 March 2013. The dataset plotted is ILNSA1B. Figure (b) is the flight track. Figure (c) represents the red square overlying a portion of the track in (b), which indicates the leading direction of the subsection of the ATM scan.....	34
Figure 23.	OIB flight tracks across western Arctic 2009–2015. Source: NSIDC (2016). Flights were flown during the annual spring season, to provide altimetric measurements of sea ice freeboard following winter freezeup. Depicted are the tracks from 43 OIB flights. ICESat-2.....	35

Figure 24.	Schematic of ICESat-2 LASER footprint along track. Source: NASA (2016a). ATLAS will generate three pairs of LASER beams, improving sea ice coverage and elevation estimates.	36
Figure 25.	Sea Ice surface heat budget. Source: Perovich and Richter-Menge, (2009). Radiative and turbulent heat fluxes are primary contributors to sea ice growth and melt. Sea ice melt is omnidirectional, while growth is downward. Radiative fluxes are annotated in orange, turbulent fluxes in red.	39
Figure 26.	Image of brine pockets in first year ice. Source: Light et al. (2003). Brine inclusions and gas bubbles are visible, which change the density and specific heat of sea ice.	40
Figure 27.	Mechanical forcing of Arctic sea ice from (a) Source: Perovich and Richter-Menge (2009), (b) Source: Jack Cook, Woods Hole Oceanographic Institute. Four forcing mechanisms, as well as the Coriolis force, influence the motion of sea ice as seen in (a). Wind forcing and ocean currents transport sea ice across the Arctic Basin is seen in (b). Sea ice motion is dependent upon wind and current speed, ice roughness and drag.	41
Figure 28.	Anisotropic ice flow in the Beaufort Sea, April 29, 2011. Source: Global Fiducials Library (2015) Angles between leads that are formed across ice floes are often 30° to 40°.	44
Figure 29.	RASM domain. Source: Andrew Roberts, Naval Postgraduate School, (2015). The red line bounds the atmosphere-land domain with 50 km grid cells. The white line surrounds the ice-ocean domain with approximately 9 km grid cells and green represents major rivers and lakes delivering runoff to the ocean. The black line is the Central Arctic analysis domain, the focal region of this thesis. Blue shades detail bathymetry with the ocean domain, while orange and yellow hues indicate topography gradation.	50
Figure 30.	Single grid point method of sampling model freeboard along satellite paths. The temporal mean of the freeboard is calculated for each corresponding RASM grid point directly under the satellite track. The red box indicates the single grid point sampled under the satellite track.	55
Figure 31.	Expanded cross-track sampling. The satellite data collected at one RASM grid point is averaged and expanded to the surrounding 8 grid points. This approach is designed to make better use of the available data by expanding its spatial reach. The gray box details	

the multiple grid points sampled, expanding from the single (red) grid cell	56
Figure 32. RASM 2004 EAP and EVP mean seasonal thickness \bar{h}_i . The vectors represent sea ice drift. The shading represents the mean sea ice thickness for each grid cell. The magenta line is from the NOAA Climate Data Record of sea ice extent (Meier et al., 2013).....	61
Figure 33. For a more detailed description, see Figure 32. This data is for year 2007.....	61
Figure 34. a) 2007 $Bias(\bar{fb}_{ICESat-2})$ for freeboard sampled along ICESat-2 tracks for one complete 91-day repeat orbit period over the spring for April to June using the ICESat-2 emulator and RASM described in Chapter 3. b) Biases in (a) that are statistically significant at the 95% confidence interval (red). In this case, only model grid cells were sampled directly under each satellite track within ± 1 hour of the satellite pass as shown in Figure 30.....	65
Figure 35. For a more detailed description, see Figure 34. This data is for fall months October to December 2007 over one complete 91-day repeat orbital period.....	65
Figure 36. a) 2007 $Bias(\bar{fb}_{ICESat-2})$ for freeboard sampled along ICESat-2 tracks for one complete 91-day repeat orbit period over the spring for April to June using the ICESat-2 emulator and RASM described in Chapter III using multiple grid-point sampling. b) Biases in (a) that are statistically significant at the 95% confidence interval (red).....	66
Figure 37. For a more detailed description, see Figure 36. This data is for fall months October to December over one complete 91-day repeat orbital period. The broad, circular feature depicted in Figure b may represent an inconsistency within the model and how RASM is handling the ice edge during this season.....	67
Figure 38. a) Winter ICESat freeboard series 2003 to 2008: Ensemble mean of Power Spectral Density in dB. with the p exponent estimated from the line in red, and associated R^2 fit between 400 meters to 30 kilometers. b) The individual ICESat tracks used to calculate the ensemble average. Winter flights are annotated by the blue cells in Table 1 in Chapter II. The color bar represents freeboard in meters.	69
Figure 39. For a more detailed description, see Figure 38. This data is for summer 2004 and 2006, corresponding to the green cells in Table 1 in Chapter II.....	70

Figure 40.	For a more detailed description, see Figure 38. This data is for fall, 2003 to 2008, corresponding to the orange cells in Table 1 in Chapter II.	70
Figure 41.	a.) OIB spring series for 2009 to 2015: Ensemble mean of power spectral density in dB. with the p exponent estimated from the line in red, and associated R^2 fit between 400 meters to 100 kilometers. b) The individual OIB tracks used to calculate the ensemble average.....	73
Figure 42.	Individual OIB Flight conducted on 02 April 2009: Power Spectral Density in dB. with the p exponent estimated from the line in red, and associated R^2 fit between 400 meters to 100 kilometers. b) The individual OIB track used to calculate PSD.	73
Figure 43.	For a more detailed description, see Figure 42. This data is for an OIB Flight conducted on March 14, 2014.	74
Figure 44.	$\langle \overrightarrow{fb}_{obs} \rangle$ for ICESat, calculated for single grid-point sampling in a) spring and b) fall 2007. The model bias for these seasons, $Bias(\overrightarrow{fb}_{model})$ is provided in c) and d), respectively, for the RASM simulation using EAP sea ice mechanics, and e) and f) for the EVP sea ice mechanics variant.....	77
Figure 45.	ICESat Emulator 2007 Welch's T-test using Single Grid Point. Panels a-d correspond to Figure 44 c-f. $Bias(\overrightarrow{fb}_{model})$ that is statistically significant at the 95% confidence interval is represented in red.	78
Figure 46.	ICESat Emulator 2007 sample size using single grid point sampling. Color bars represent the number of samples for the satellite and models corresponding to results in Figures 44 and 45.....	79
Figure 47.	$\langle \overrightarrow{fb}_{obs} \rangle$ for ICESat, calculated for multiple grid-point sampling in a) spring and b) fall 2007. The model bias for these seasons, $Bias(\overrightarrow{fb}_{model})$ is provided in c) and d), respectively, for the RASM simulation using EAP sea ice mechanics, and e) and f) for the EVP sea ice mechanics variant.....	80
Figure 48.	ICESat Emulator 2007 Welch's T-test using Multiple Grid Points. Panels a-d correspond to Figure 47 c-f. $Bias(\overrightarrow{fb}_{model})$ that is statistically significant at the 95% confidence interval is represented in red.	81

Figure 49.	ICESat Emulator 2007 Sample Size using Single Grid Point sampling. Color bars represent the number of samples for the satellite and models corresponding to results in Figures 44 and 45.	82
Figure 50.	ICESat 2007 thickness distribution. Probability density function of freeboard, analogous to thickness distribution PDF displayed from Hutchings et al. (2008). Blue represents ICESat observations, Red represents multiple grid point sampling technique and magenta represents single grid point sampling.	83
Figure 51.	ICESat Emulator 2007 Taylor Diagram. The red and blue circles represent observations, and the squares are the model representations of both the single grid point and multiple grid point technique.....	85
Figure 52.	$\langle \overrightarrow{fb}_{obs} \rangle$ for ICESat, calculated for multiple grid-point sampling in a) winter and b) fall 2004. The model bias for these seasons, $Bias(\overrightarrow{fb}_{model})$ is provided in c) and d), respectively, for the RASM simulation using EAP sea ice mechanics, and e) and f) for the EVP sea ice mechanics variant.....	86
Figure 53.	$\langle \overrightarrow{fb}_{obs} \rangle$ for ICESat, calculated for multiple grid-point sampling in a) winter and b) Fall 2004. The model bias for these seasons, $Bias(\overrightarrow{fb}_{model}(\overline{h}_s = 0))$ is provided in c) and d), respectively, for the RASM simulation using EAP sea ice mechanics, and e) and f) for the EVP sea ice mechanics variant.	88
Figure 54.	$\langle \overrightarrow{fb}_{obs} \rangle$ for ICESat, calculated for multiple grid-point sampling in a) spring and b) fall 2007. The model bias for these seasons, $Bias(\overrightarrow{fb}_{model})$ is provided in c) and d), respectively, for the RASM simulation using EAP sea ice mechanics, and e) and f) for the EVP sea ice mechanics variant.....	89
Figure 55.	$\langle \overrightarrow{fb}_{obs} \rangle$ for ICESat, calculated for multiple grid-point sampling in a) spring and b) fall 2007. The model bias for these seasons, $Bias(\overrightarrow{fb}_{model}(\overline{h}_s = 0))$ is provided in c) and d), respectively, for the RASM simulation using EAP sea ice mechanics, and e) and f) for the EVP sea ice mechanics variant.	90
Figure 56.	ICESat 2004 freeboard variability. Probability density function of freeboard, analogous to thickness distribution PDF displayed from Hutchings et al. (2008). Blue represents ICESat observations, Red	

represents multiple grid point sampling technique and magenta represents single grid point sampling.	92
Figure 57. For a more detailed description, see Figure 56. This data is for 2007 central Arctic freeboard	93
Figure 58. ICESat Emulator 2004: RASM model performance. The EAP results are in light blue, the EVP results are in red and the observations are indicated by the dark blue circle. The solid circles are calculations using freeboard with snow loading, the white circles are calculations using freeboard without snow loading.	94
Figure 59. ICESat Emulator 2007: RASM model performance. The EAP results are in light blue, the EVP results are in red and the observations are indicated by the dark blue circle. The solid circles are calculations using freeboard with snow loading, the white circles are calculations using freeboard without snow loading.	95
Figure 60. a) 2007 $Bias(\bar{fb}_{ICESat-2})$ for freeboard sampled along ICESat-2 tracks for one complete 91-day repeat orbit period over the winter for January to March using the ICESat-2 emulator and RASM described in Chapter III. b) Differences in (a) that are statistically significant at the 95% confidence interval (red). In this case, only model grid cells were sampled directly under each satellite track with ± 1 hour of the satellite pass as shown in Figure 30.	103
Figure 61. a) For a more detailed description, see Figure 60. This data is for summer months July to September 2007 over one complete 91-day repeat orbital period.	104
Figure 62. 2007 $Bias(\bar{fb}_{ICESat-2})$ for freeboard sampled along ICESat-2 tracks for one complete 91-day repeat orbit period over the winter for January to March using the ICESat-2 emulator and RASM described in Chapter III using multiple grid-point sampling. b) Differences in (a) that are statistically significant at the 95% confidence interval (red).	104
Figure 63. For a more detailed description, see Figure 62. This data is for summer months July to September 2007 over one complete 91-day repeat orbital period.	105
Figure 64. a) 1996 $Bias(\bar{fb}_{ICESat-2})$ for freeboard sampled along ICESat-2 tracks for one complete 91-day repeat orbit period over the winter for January to March 1996 using the ICESat-2 emulator and RASM described in Chapter III. b) Differences in (a) that are statistically	

significant at the 95% confidence interval (red). In this case, only model grid cells were sampled directly under each satellite track with ± 1 hour of the satellite pass as shown in Figure 30.	105
Figure 65. a) For a more detailed description, see Figure 64. This data is for spring months April to June 1996 over one complete 91-day repeat orbital period.	106
Figure 66. a) For a more detailed description, see Figure 64. This data is for but for fall months July to September 1996 over one complete 91-day repeat orbital period.	106
Figure 67. For a more detailed description, see Figure 64. This data is for fall months October to December 1996 over one complete 91-day repeat orbital period.	107
Figure 68. a) 1996 $Bias(\bar{fb}_{ICESat-2})$ for freeboard sampled along ICESat-2 tracks for one complete 91-day repeat orbit period over the winter for January to March using the ICESat-2 emulator and RASM described in Chapter III using multiple grid-point sampling. b) Differences in (a) that are statistically significant at the 95% confidence interval (red)....	107
Figure 69. For a more detailed description, see Figure 68. This data is for spring months April to June 1996 over one complete 91-day repeat orbital period.	108
Figure 70. For a more detailed description, see Figure 68. This data is for summer months July to September 1996 over one complete 91-day repeat orbital period.	108
Figure 71. For a more detailed description, see Figure 68. This data is for fall months October to December 1996 over one complete 91-day repeat orbital period.	109

THIS PAGE INTENTIONALLY LEFT BLANK

LIST OF TABLES

Table 1.	ICESat campaign time periods and associated LASERs. Source: NSIDC (2016) and NASA (2016b). This table highlights ICESat operational dates, duration, LASER used to conduct sea surface elevation measurements and repeat orbit. The table is color coded to represent each season. Orange represents fall operations, blue is spring and green is for the summer operations. Gray represents data used in analysis presented later in this thesis.....	32
Table 2.	Thermodynamic notation for Equation 2	38
Table 3.	RASM configuration. This table provides the spatial and temporal resolution of RASM. Source: Roberts et al. (2015, table 1)	51
Table 4.	Variable notation used in OIB and ICESat Calculations	59
Table 5.	Summary of ICESat spatial freeboard noise characteristics, and R^2 values.	71
Table 6.	OIB Spectral Analysis Values	74
Table 7.	Variance and correlation weighted skill scores for fall 2004 and 2007....	99
Table 8.	Variance and correlation weighted skill scores for winter 2004 and spring 2007.....	99

THIS PAGE INTENTIONALLY LEFT BLANK

LIST OF ACRONYMS AND ABBREVIATIONS

ATLAS	Advanced Topographic LASER Altimeter System
ATM	Airborne Topographic Mapper
CICE	Sea Ice Model
CMIP	Climate Research Programme Coupled Model Intercomparison Project
CMIP5	Climate Research Programme Coupled Model Intercomparison Project Phase 5
CORE	Common Ocean Reference Experiment
CryoSAT	Cryosphere Satellite
EIA	Energy Information Administration
GCM	Global Climate Models
GLAS	Geoscience LASER Altimeter System
GSFC	Goddard Space Flight Center
ICESat	Ice, Cloud, and land Elevation Satellite
ICESat-2	Ice, Cloud, and land Elevation Satellite Two
NASA	National Aeronautics and Space Administration
NSIDC	National Snow and Ice Data Center
OIB	Operation IceBridge
POP	Los Alamos Laboratory Parallel Ocean Program
RASM	Regional Arctic System Model
VIC	Variable Infiltration Capacity Model
WGS 84	World Geodetic System 1984
WRF	Weather Research and Forecasting Model

THIS PAGE INTENTIONALLY LEFT BLANK

ACKNOWLEDGMENTS

First and foremost, I would like to thank my thesis advisor, Andrew Roberts. Andrew's drive and continual quest for knowledge are inspirational. Andrew has been an exceptional mentor, setting the highest of standards. This project proved to be both challenging and utterly rewarding. Andrew, thank you for your patience, guidance and wisdom. It was an absolute honor and privilege to work with you.

Next, I would like to thank several people who provided expertise and support over the last year. Wieslaw Maslowski, whenever we would discuss the Arctic or work on my thesis, would have a smile on his face. Wieslaw, your passion always shines through, providing ongoing motivation. Sinead Farrell and Jackie Richter-Menge, thank you for answering my incessant requests for data, providing insight into the Operation IceBridge, ICESat and ICESat-2 missions, and becoming confidants. To the National Snow and Ice Data Center and National Aeronautics and Space Administration, without access to your datasets, this research have been impossible. I am truly humbled and grateful to all those I have worked with during this process.

John Joseph, thank you for the opportunity to participate in ICEX. From learning about the Arctic environment to actually camping on an ice floe was a dream come true, from which I have learned a great deal. Thank you for the adventure of a lifetime. I would like to thank the Naval Postgraduate School faculty and staff for the incredible opportunity and education. To my classmates and fellow students, I have learned a great deal from you all and look forward to working with you in the future. And to my husband, I am genuinely grateful for your love, sacrifices, and support over last two years.

THIS PAGE INTENTIONALLY LEFT BLANK

I. INTRODUCTION

Climate change is rapidly altering the Arctic environment, as evidenced by the decline of Arctic sea ice (Jeffries et al. 2013). Sea ice extent, the region of the ocean with greater than 15% ice concentration, has greatly reduced across the Northern Hemisphere during the 21st century relative to climatological records (IPCC 2013). Continuous records of sea ice extent measured via satellites since 1979, confirm that sea ice extent has retreated toward the poles during the satellite era (NSIDC 2016). Using passive microwave satellite data, Figures 1 and 2 have been constructed by the National Snow and Ice Data Center (NSIDC) and depict a downward trend of sea ice extent for both September and March spanning more than 37 years (NSIDC 2016). These months were chosen because September follows the summer melt season and typically provides yearly minimum monthly sea ice extent. March is the observed month for maximum sea ice extent following the winter growth period. In recent years, September and March monthly extents have been well below the 30-year monthly average, which is evidence of the rapid, persistent decline of Arctic sea ice over the last several decades.

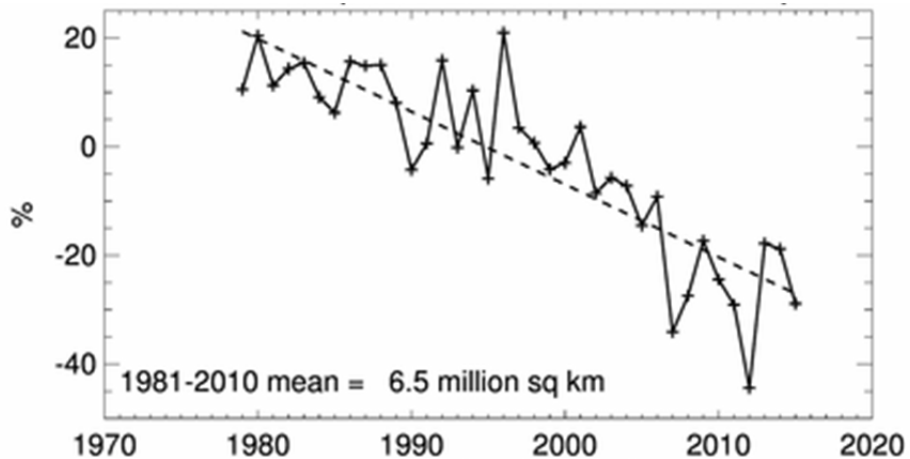


Figure 1. Northern Hemisphere extent anomalies, September 2015. Source: NSIDC (2016). The Northern Hemisphere sea ice extent for the month of September 2015 is declining at a rate of $-13.4 \pm 2.7\%$ per decade since the late 1970s. The mean sea ice extent is 6.5 million square kilometers.

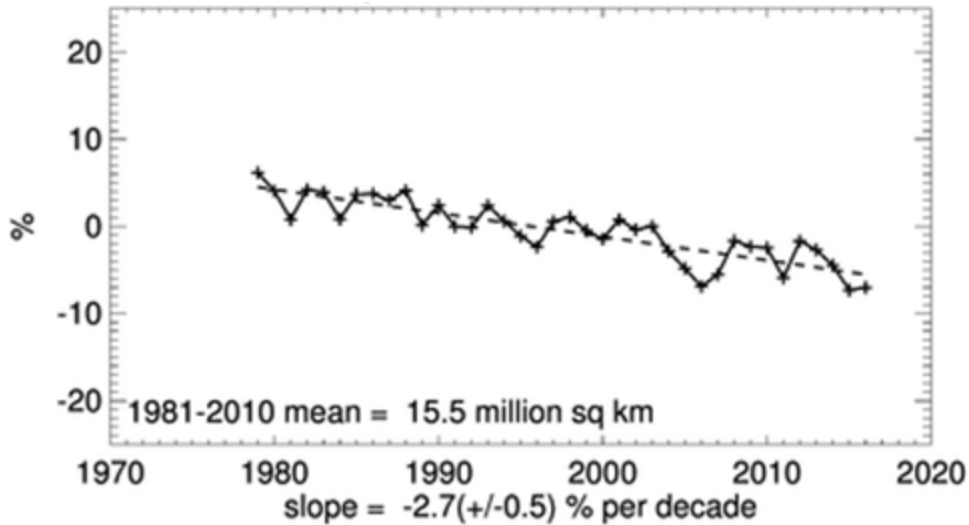


Figure 2. Northern Hemisphere extent anomalies, March 2016. Source: NSIDC (2016). The Northern Hemisphere sea ice extent for the month of March 2016 is declining at a rate of $-2.7 \pm 0.5\%$ per decade since the late 1970s. The March mean sea ice extent is 15.5 million square kilometers.

Aside from interactions with the climate system, the transpiring changes in Arctic sea ice will potentially have large future impacts on local ecosystems, ocean biochemistry, and physical processes. These are of great interest to scientists, governments, and the business and indigenous communities. With the decline of sea ice, there are opportunities for development of the Arctic as a transport route and as an oil, gas and fishing industry center. Nonetheless, associated with these opportunities are high latitude territorial claims as nations contend for natural resources within and beneath the Arctic Ocean. By drawing upon Department of Defense (DOD) capabilities and the expertise of the scientific research community, the U.S. can protect national interests and establish diplomatic strategies for the Arctic (Showstack 2013).

Knowledge of sea ice thickness provides insight into how the Arctic environment is evolving. Sea ice thickness trends are indicative of climatic changes within the Arctic Circle in response to global climate warming and its linkage to mid-latitude weather patterns (Francis and Vavrus 2012). Satellites and aircraft equipped with altimetric instruments have been developed to measure sea ice freeboard, which can be used to

provide sea ice thickness estimates across vast sections of the Arctic Ocean. Sea ice freeboard is the height of floating ice, with surficial snow, that protrudes above the ocean surface. Knowing the freeboard, as well as the density of sea ice and snow, allows the thickness of sea ice to be calculated using Archimedes' Principle. The introduction of altimetric measurements from satellites has greatly improved our understanding of sea ice thickness changes in the Arctic. However, due to measurement uncertainty as well as variations in snow cover and ice and snow density, thickness derived from freeboard has high uncertainty bounds (Kwok and Cunningham 2008; NASA 2012). Still, the collected freeboard data is very useful for developing and evaluating climate and sea ice forecast models. These classes of models are typically capable of predicting sea ice thickness, but the simulations have historically been difficult to evaluate with thickness derived from freeboard measurements due to the aforementioned uncertainty. In this thesis, we instead evaluate a model using just sea ice freeboard, which removes large potential sources of error associated with converting observed freeboard to thickness.

This thesis focuses on the use of altimetric measurements to evaluate sea ice in fully-coupled, high-resolution climate and seasonal forecast models. Sea ice thickness and snow cover are highly variable both spatially and temporally, and the main objective of this thesis is to account for this heterogeneity in developing skill metrics for sea ice models that utilize measurements of freeboard from space using LASERs. The thesis is organized as follows: Chapter I provides an overview of why sea ice is important in the global climate system and how the changing Arctic is pertinent to both U.S. national interests and the U.S. Navy. Chapter II introduces sea ice thickness, a brief history of sea ice numerical modeling and altimetric sea ice observations. Chapter III discusses the methodology, including the statistical analysis used to inter-compare modeled ice thickness with measured ice freeboard. In Chapter IV, the results from this research are examined followed by the conclusion in Chapter V, which presents a final set of skill scores applicable to both seasonal and climate model forecasts of sea ice thickness.

A. WHY IS ARCTIC SEA ICE IMPORTANT?

Sea ice is a floating medium between the atmosphere and ocean of vital importance to the Arctic marine ecosystem, Earth's energy budget as well as oceanic and atmospheric circulation (Perovich and Richter-Menge 2009). Arctic sea ice forms part of a dynamic coupled climate system, involving thermodynamic, biochemical and dynamic interactions between the atmosphere, terrestrial sources and the Arctic Ocean.

1. Arctic Sea Ice Characteristics

Sea ice formation, drift, deformation and melt change seasonally in the Arctic Ocean. Sea ice forms in fall after the surface air temperature drops below freezing and the top layer of the ocean cools to its freezing temperature. The ice continues to grow through the winter season and in the process rejects brine into the ocean, changing the density of the sea ice and the surrounding ocean water, which is important for mixing and deep ocean convection (Parkinson and Washington 1979). During this time, sea ice accumulates snow, which substantially increases the shortwave albedo of the surface (Webster et al. 2014). During the summer, the surface snow and sea ice melt, reducing Northern Hemisphere extent from an average of about 15 million km² in the winter to below about 7 million km² by late summer (NSIDC 2016). Inside the floating pack heterogeneous ice floes, or fragmented slabs of sea ice, typically vary in caliper diameter from about 100 to 5000 m, amongst which the sea ice morphology is assembled into level ice interspersed by lines of ridges and keels (Davis and Wadhams 1995; Feltham 2008; Rothrock and Thorndike 1984). With increased sunlight during the summer, slush and melt ponds develop across the floes, which greatly reduces the albedo of the surface. The thinnest sea ice melts the fastest, and sea ice that survives the summer melt season is defined as perennial, or multiyear ice.

Sea ice thickness is an indicator of the thermodynamic and dynamic history of the ice, all of which vary spatially across the Arctic Basin (Kwok et al. 2005; Nolin et al. 2002; Thorndike et al. 1975). Due to gradients in external wind and current forcing, and land boundaries, sea ice shears and compresses horizontally into thicker ice, and the mechanical strain rates and stresses within the pack may best be described with an

anisotropic sea ice rheology (Tsamados 2013). The anisotropic rheology of sea ice is a source for a network of oriented cracks, leads and ridges, formed along regions of weaker sea ice (Feltham 2008). Regions where sea ice floes converge, pressure ridges develop (Figure 3a). Conversely, regions of sea ice where floes diverge develop leads, narrow and long areas of open water (Figure 3b).

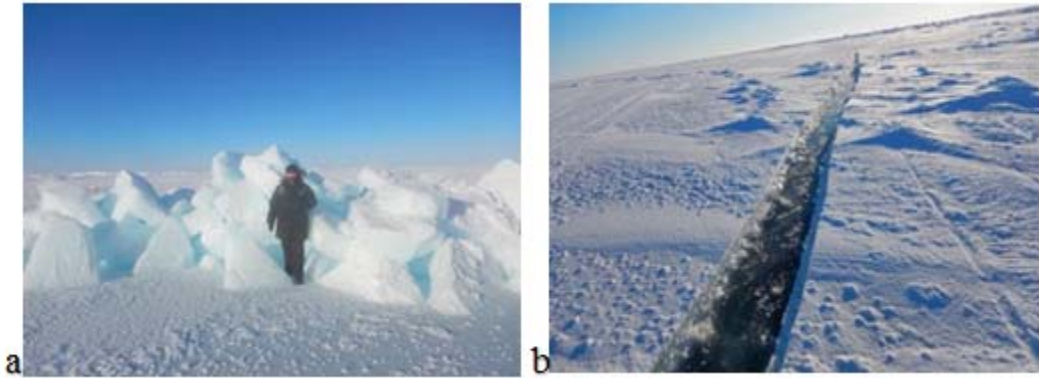


Figure 3. A ridge and lead in the Beaufort Sea, March 2016. Figure 3a is an image of a pressure ridge in the Beaufort Sea. Figure 3b is an image of a developing lead, horizontally tilted.

Surface roughness is an indicator of sea ice age, where first-year ice is smooth, in contrast to multi-year ice, which has typically been subjected to considerable deformation. Figures 4 and 5 show sea ice located north of Prudhoe Bay, Alaska, in the Beaufort Sea. Present in the images are areas of multi-year and first-year ice, numerous ridges, leads, and regions of convergence and divergence, giving insight into the spatial heterogeneity of sea ice on scales of less than 5 km.



Figure 4. Sea ice ridges in the Beaufort Sea, March 2016. This image of a sea ice floe was captured north of Prudhoe Bay, Alaska, and depicts the development of a sea ice ridge.



Figure 5. Leads in sea ice in the Beaufort Sea, March 2016. This image of a sea ice floe is north of Prudhoe Bay, Alaska, and depicts leads between the floes.

2. Sea Ice Energy Balance

Between the Northern and Southern Hemispheres, sea ice covers a region about 2.5 times the size of Canada at any given time (NSIDC 2016). Given this vast coverage, sea ice is important to the Earth's total albedo and energy budget. Snow and sea ice act as an insulator, limiting the absorption of shortwave radiation by the ocean in summer where it is covered by sea ice, and blanketing the ocean from turbulent heat transfer to a frigid atmosphere above in the winter. Sea ice albedo changes seasonally and inter-

annually as a result of the formation and melting processes of sea ice and snow distribution on ice, as seen in Figure 6. Sea ice with large albedo values, such as for snow covered multi-year ice (albedo of ~0.8), reflect more of the incoming solar radiation and enable sea ice to survive the summer months. Bare first-year ice, with an albedo of 0.52, reflects significantly less solar radiation than multi-year ice, which enhances melting progression. Melt ponds have a range of albedo values, from 0.15 to 0.29, depending upon the age, depth, and type of sea ice and snow coverage during the melt period. In stark contrast, sea water albedo is only about 0.06, meaning it absorbs more incoming solar radiation than sea ice resulting in warmer sea surface temperatures. One of the main concerns with sea ice retreat and record low sea ice extent is the increasing period of exposed ocean to radiational heating in summer. This leads to warming of the upper ocean waters; and with a higher specific heat content than ice, the ocean is able to store the added heat well into the winter months, in turn delaying the onset of sea ice formation and melting ice from below (Perovich et al. 2007).

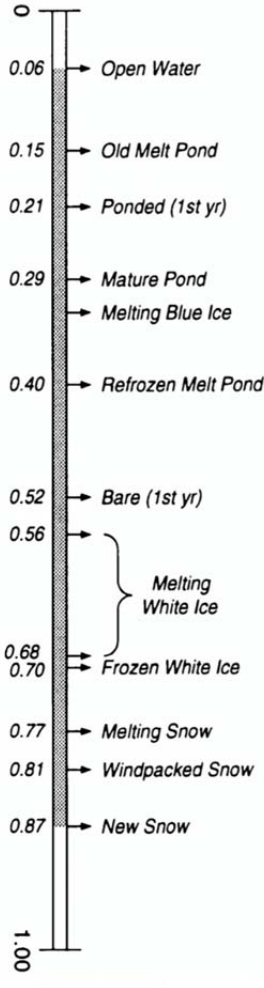


Figure 6. Albedo of sea ice. Source: Perovich (1996). The scale represents the albedo of sea ice in differing physical states. Measurements were conducted by Perovich during a spring to summer season transition to observe the albedos associated with the changes in the physical states of sea ice.

In addition to sea ice albedo varying both temporally and spatially, the albedo also depends upon the physical conditions of sea ice. Both first-year and multi-year ice experience growth, melt, and are subject to snow coverage. Perovich and Polashenski (2012) observed seven surface states of first-year ice: 1) cold snow; 2) melting snow; 3) pond formation; 4) pond drainage; 5) pond evolution; 6) open water; and 7) freezeup. Each of the states have a different albedo as seen in Figure 6, varying from 0.06 prior to freezeup to 0.85 in the winter. Multi-year ice has larger albedo during the melt season

(Figure 7), as compared to first-year ice, mainly because it does not reach the open water state (Perovich and Polashenski 2012). With the decline in multi-year sea ice area at a rate of -17.2% per decade (Comiso 2011) in the Arctic, there is a shift to more prevalent first year ice (Figure 8).

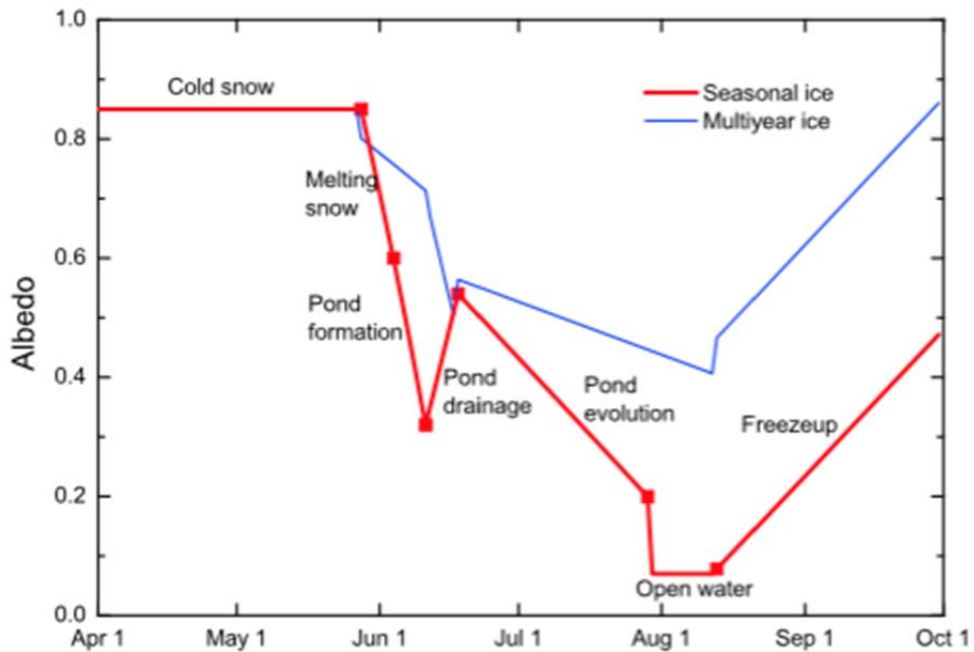


Figure 7. Annual evolution of sea ice albedo. Source: Perovich and Polashenski (2012). Time series sea ice albedo from the winter season to fall freeze up. The red line represents first year ice and the seven associated phases. The blue line represents multi-year ice.

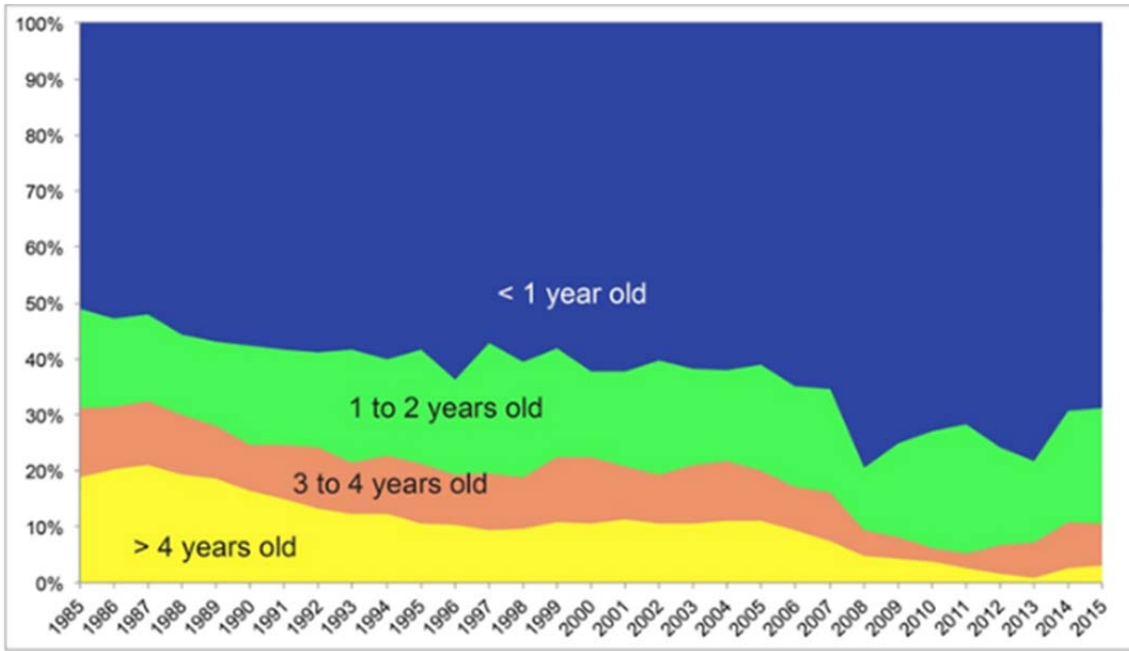


Figure 8. March sea ice categorized by age. Source: Perovich et al. (2015).

Between the years 1981–2015, there has been a decline in multi-year ice and a shift to more first year ice.

With the changes in sea ice extent, a shift from perennial to first-year ice, and the associated disparity of albedo values, there has been increased absorption of incoming solar radiation into the Arctic, sustaining the ice-albedo feedback loop (Perovich and Polashenski 2012).

Between 1979 and 2005, there has been a positive trend of incoming solar radiation into the Arctic Ocean as seen in Figure 9 across 89% of the Arctic Ocean (Perovich et al. 2007). With the observed rates of sea ice retreat, Perovich's associated values of solar heat flux into the ocean have increased by as much as 4% per year with a mean of 0.81% per year. This adds another source for sea ice ablation, well beyond the summer melt season. Warm waters may continue to melt sea ice from the bottom, if they are mixed upward into the surface mixed layer and to the bottom of sea ice (Perovich and Polashenski 2012). With the current pace of sea ice retreat, delay in winter formation and failure to accumulate to the historic levels, more ocean surface is absorbing solar radiation, which in turn is affecting the Arctic surface energy balance.

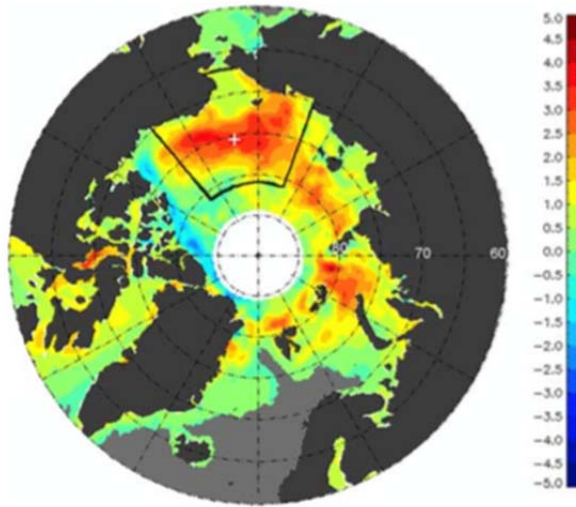


Figure 9. Linear Trend (%/year) of solar heat flux into the Arctic Ocean. Source: Perovich (2007). The color scale represents average percent per year increase of heat input into the Arctic Ocean, with the largest increase in the Chukchi Sea.

B. CONSEQUENCES OF A CHANGING ARCTIC ENVIRONMENT

The unprecedented speed and magnitude at which the changes in the Arctic are occurring have both local and global reaching impacts and consequences. Given the observed, dramatic sea ice loss, there may be correlation between sea ice decline and extreme weather in the mid-latitudes and ocean circulation patterns (Francis and Vavrus 2012). Atmospheric temperatures in the Arctic region are increasing more rapidly than in the rest of the world (Figure 10) supporting enhanced rates of sea ice melt and warmer sea surface temperatures.

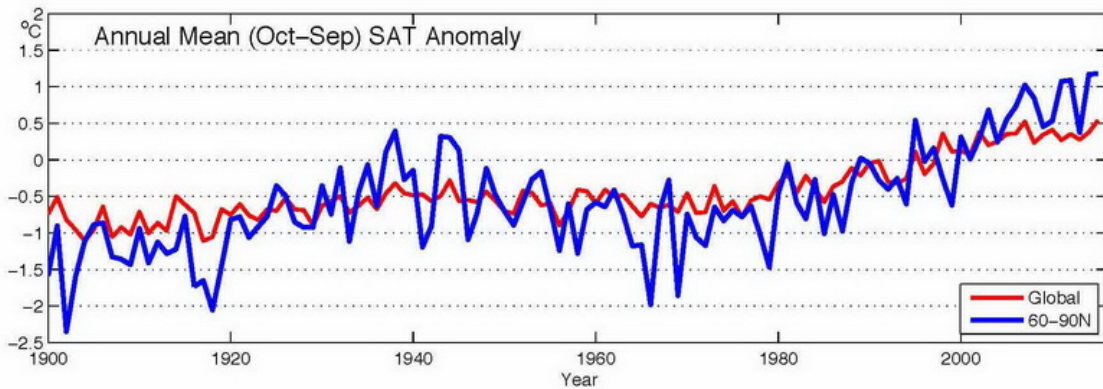


Figure 10. Arctic and global mean annual surface air temperature anomaly between the years 1900–2014. Source: NOAA (2016). The mean annual surface temperature, relative to the 1981–2010 mean, for the Arctic region has an increasing positive trend since the 1980s. The rate at which the Arctic surface temperatures are increasing is twice the rate of increase in global surface temperatures.

Due to Arctic Amplification, which is the enhanced warming of the atmosphere and ocean temperatures in the Arctic relative to the mid-latitudes and tropics, the Northern Hemisphere atmospheric latitudinal thickness gradients are decreasing (Francis and Vavrus 2012). The weakened atmospheric gradient between the polar region and mid-latitudes has been hypothesized to have widespread atmospheric ramifications, including atmospheric blocking and prolonged synoptic events, including persistent droughts and extreme cold spells (Francis and Vavrus 2012). This synoptic regime, which corresponds with the latitudinal elongation of the jet stream, has been studied in parallel with Arctic climate change. The change in jet stream, global weather patterns, and extreme weather phenomena across the Northern Hemisphere may be one consequence of the Arctic sea ice retreat. However, given the rapid rate at which the Arctic is warming, and short data records available, there is uncertainty in the degree to which climate change observed in the Arctic is impacting mid-latitude weather (Cohen et al. 2014).

The potential of longer ice-free seasons over expanding area of the Arctic Ocean increases the opportunity for seasonal international trade routes, fishing and commercial tourism industries (Smith and Stephenson 2013). Many climate models predict a shipping

route to be ice free during September along the Northern Sea Route (Figure 11) by the middle of the 21st century (Smith and Stephenson 2013). This would enable ships, without ice strengthened hulls to transit the Arctic (Smith and Stephenson 2013). Pending fruition of the ice-free environment, international trading through the Arctic would greatly reduce travel distances for ships moving between Pacific and Atlantic countries, in lieu of the Suez Canal (Figure 11).

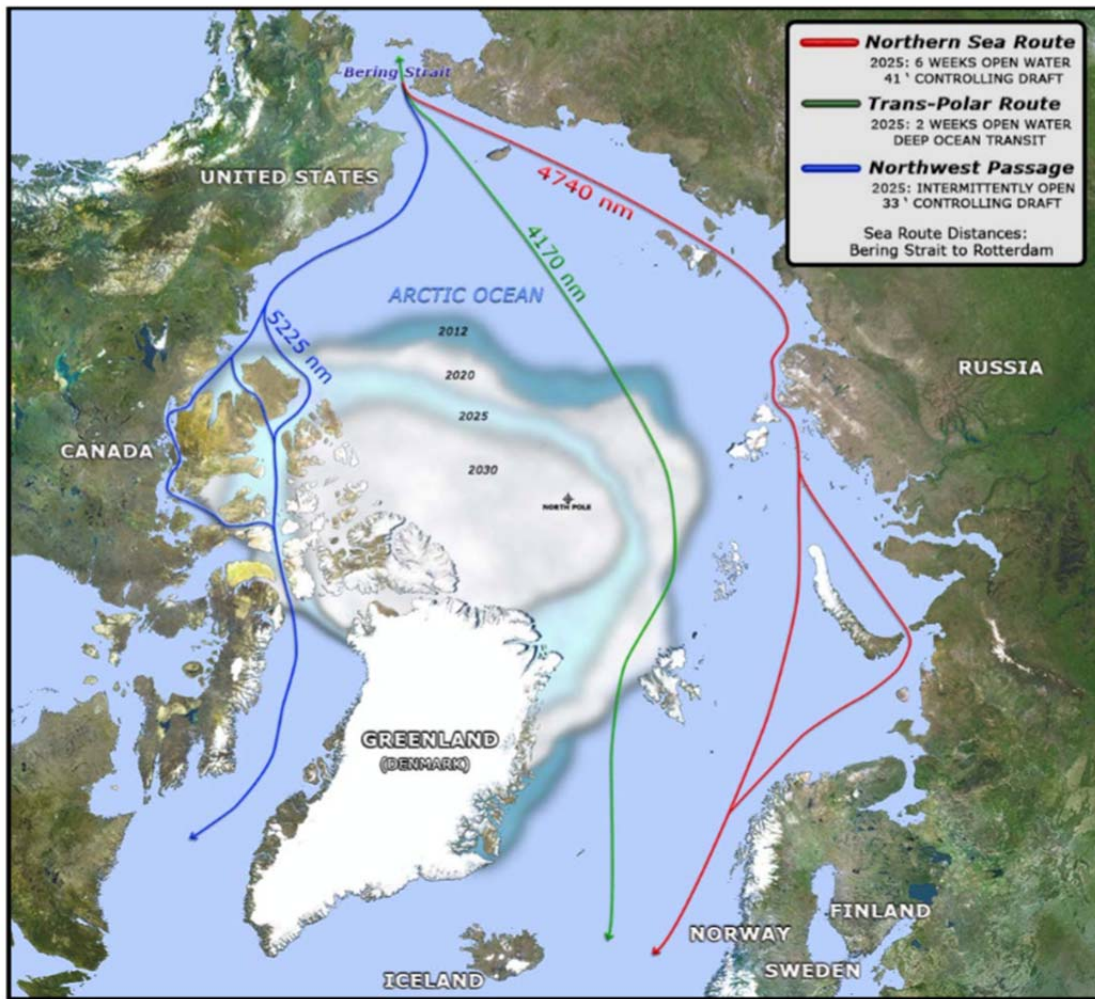


Figure 11. Trans-polar sea routes decreased sea ice extent. Source: Arctic Roadmap (2014). With the decline in sea ice, shipping routes through the Arctic Ocean may provide the opportunity for trans-polar maritime routes and increased maritime activities.

The climate forecast of open water area furthers human involvement and development across the Arctic. The Arctic region has prospective natural resources, including oil and gas, particularly along the continental shelf (Gautier et al. 2009). Such increased activities and development may further disrupt the delicate environment and clash with the indigenous culture and their way of life in the Arctic.

Sea ice loss also alters the local and distant ecosystems. From acting as a habitat for Arctic mammals, such as polar bears, walruses and ringed seals, to enabling subsurface phytoplankton blooms, and becoming a region of primary production for marine life, sea ice is an important resource to ensure the Arctic ecosystem remains in balance. Studies conducted by Arrigo et al. (2012) show the importance of sea ice and melt ponds to phytoplankton blooms, with under-ice biomass in much higher concentrations than in open water, during early spring. Such studies emphasize the importance of sea ice and melt ponds enabling solar radiation penetration into the upper oceanic layer, providing a favorable environment for phytoplankton growth, which is the base of the Arctic food web. With the sea ice reduction across continental shelves and slopes, Arctic wildlife is at risk of having to travel longer distances for food sources.

C. UNITED STATES' INTEREST IN THE CHANGING ARCTIC ENVIRONMENT

The Arctic is the polar region north of the line of latitude 66 degrees, 33' 44" N, consisting of both the terrestrial and oceanic areas, with approximately 4 million inhabitants (UNEP 2013). There are eight Arctic nations, including the United States (Figure 12). In addition to the Arctic states, there are six organizations representing Arctic indigenous tribes living within the Arctic Circle (Arctic Council 2016).



Figure 12. Map of the Arctic nations. Source: National Science Foundation (1998). The United States, Canada, Russia, Norway, Denmark, Finland, Sweden, and Iceland are the eight Arctic nations that encircle the Arctic Ocean. Russia has the longest coastline in the region and about two-thirds of Canada's marine coastline lies within the Arctic.

Five of these countries border the Arctic Ocean and have a right to claim territorial seas within the Arctic Circle. Their claims may extend within 12 nautical miles from a coast baseline, with an Exclusive Economic Zones (EEZ) extending up to 200 nautical miles, adjacent to the territorial sea (UNCLOS 1994). Per the United Nations Convention on the Law of the Sea (UNCLOS), a state that has a continental shelf with a submarine ridge, shall not exceed more than 350 nautical miles from the territorial sea baseline (UNCLOS 1994). Following this UNCLOS rule, Russia has claimed that the Lomonosov Ridge is an extension of the Siberian continental shelf (Figure 13; *New York Times* 2007). With the evolving Arctic environment, new opportunities arise for the use and exploration of the vast area, with risks of potential cultural and government conflicts.

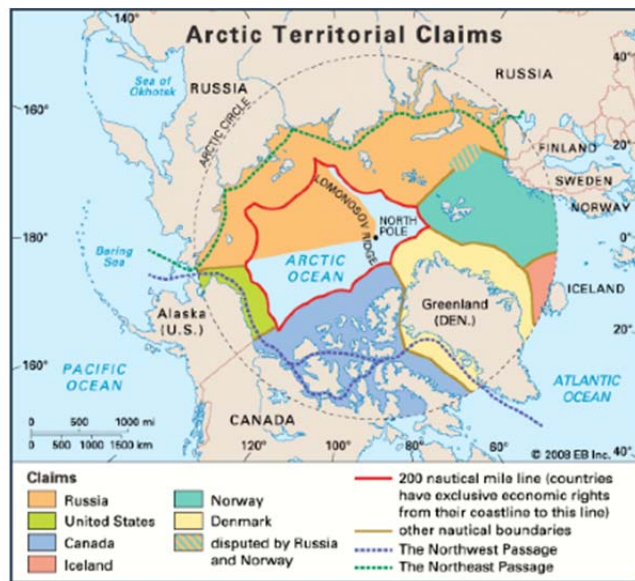


Figure 13. Arctic territorial claims. Source: Encyclopedia Britannica (2010). The Arctic territorial claims by the Arctic States. The red line represents the 200 nautical miles EEZ as authorized by UNCLOS. Russia's proposed claim extends toward the North Pole, into international waters. Russia considers the Lomonosov ridge as an extension of the Siberian continental shelf.

Fishing, oil, gas, mineral and tourism opportunities are all economic drivers for Arctic states to develop a plan and regulations within the Arctic. Estimates from the United States Energy Information Administration (USEIA) suggests the Arctic region may contain about 22% of the world's undiscovered oil and natural gas deposits. Additionally, national security interests, territorial claims and resource protection have motivated Arctic states to develop their own capabilities in the harsh environment (2009). The United States National Strategy for the Arctic Region focuses on three priorities: 1) advancing security interests; 2) regional stewardship; and 3) international cooperation. In April 2014, the United States assumed the role of chairmanship of the Arctic Council Ministerial, allowing for the opportunity for the United States to promote Arctic policy (U.S. Department of State 2016). Regulation enforcement, freedom of the seas, safety, and advancing security are paramount for the United States in the Arctic region. The United States has focused efforts on Alaska and tribal communities to develop infrastructure supporting U.S. economic and security interests. United States' efforts will

pursue proper stewardship, while respecting differing cultures and traditions, as well as the environment and natural resources, in an effort to continue to maintain peaceful negotiations of maritime boundaries.

The Arctic is a region where relatively few people live and sustain livelihoods. Both ongoing research and a fundamental understanding of the region are required to determine long-term impacts on, and interactions between, ecosystems, indigenous cultures and the physical environment. International cooperation and respect is the third focal point of the U.S. National Strategy to avoid conflict, protect the environment and support emerging industry. Challenges and opportunities will arise in an otherwise peaceful region of the Earth as the region becomes more conducive to human activities. The United States is focused on protecting its national interests, respecting the environment and working in cooperation with other Arctic States and indigenous people to explore the Arctic, build a sustainable infrastructure, protect sovereign claims and promote safety (National Strategy for the Arctic Region 2013).

D. U.S. NAVY RELEVANCE

For decades, the U.S. submarine forces have trained and operated within the Arctic Region (Arctic Roadmap 2014). However, and as noted earlier, the Arctic environment is changing at an unprecedented rate. Warmer regional temperatures, longer sea ice melt seasons, and significant multi-year ice melt rates, together are leading to an increase in accessibility to the region and potential security implications for the United States. The U.S. national security objectives are to ensure geopolitical stability in the Arctic, preserve freedom of the seas, and to protect national interests and resources (National Strategy for the Arctic Region 2013).

To support national objectives, the U.S. Navy, including surface and aviation assets, must be prepared and adequately equipped to operate within the Arctic environment. Armed with the initiative to increase the number of naval personnel operating in the Arctic by 2020, advances must be made to further understand the changing Arctic environment which is critical to personnel safety, effective use of assets, and operational support (Arctic Roadmap 2014).

Canada, Norway, Russia and Denmark have all increased military activity within the Arctic region as sea ice extent has diminished and countries pursue natural resource exploration (*New York Times* 2016). Russia is currently establishing Arctic Command Headquarters and opening bases across the Arctic, as shown in Figure 14 (*New York Times* 2015; *Wall Street Journal* 2016a; *Wall Street Journal* 2016b; *Wall Street Journal* 2015). In 2007, Russia planted a Russian flag at the North Pole seabed as a symbolic claim (*New York Times* 2007). In the fall of 2015, Russia's Arctic claim consisted of continental shelf region, extending beyond 200 nautical miles from the coastline, which is the internationally recognized EEZ (*New York Times*; 2016, United Nations 2016). This claim includes an additional area of 1.2 million square kilometers. While Arctic states may not have hostile intent, with the increase of military activities, the nations are making scientific advancements and progress in understanding the climate to protect their national interests. Additionally, Arctic nations are developing a logistical framework essential to maintaining year round operations in the Arctic.



Figure 14. Russian Military Bases within the Arctic Circle since 2014. Source: Center for Strategic and International Studies (2015) and New York Times (2015). Russia has established an Arctic command with the intent of re-opening former airfields and bases.

The U.S. aims to maintain peaceful relations with all Arctic states. Although the U.S. is not a signatory to United Nations Convention on the Law of the Sea (UNCLOS),

intentions are to use international means, including UNCLOS, to work toward resolutions of potential conflicts in lieu of military force. However, in line with the National Strategy, U.S. military forces need the ability to train and develop skills for operating in the Arctic environment, using subsurface, surface and aircraft assets (DOD Arctic Strategy 2013). The U.S. military must obtain a level of readiness to defend U.S. territorial waters, national interests and protect maritime trade routes. Strategic advances, Arctic training and operations, gave way to the military playing a scientific role in the Arctic following the Cold War (Arctic Roadmap 2014). The U.S. military and U.S. Coast Guard have been sources of environmental observations, science and research throughout the Arctic, with limited military training events. Aside from the biennial Ice Exercise (ICEX) and the Scientific Arctic Science Program (SCICEX), which are collaborative submarine and scientific research exercises conducted by the U.S. Navy, few U.S. military operations take place in the Arctic. As stated by Vice Admiral Joseph Tofala, Commander, Submarine Forces:

The (ICEX) objectives were demonstrating presence, gaining additional Arctic operational experience, furthering partnerships and expanding scientific research. (America's Navy 2016)

With the U.S. Navy roadmap guidance, the role of the Navy will gradually expand its role in the Arctic over the next two decades. This objective will enable the U.S. Navy to pursue continued Arctic presence, and maximize the effectiveness of the military operations assimilated with civilian science (Showstack 2013).

Further research and understanding of the Arctic environment is critical to the U.S. military operations and National security. Current fiscal constraints are a challenge for the United States (Showstack 2013). Having been restrained in its involvement in the Arctic, the United States will now need to develop better equipment, build new icebreakers, establish training plans and develop guidelines for Arctic operations. To further aid leadership and policy makers, scientists and predictive computer models of the Arctic environments have a vital role in understanding the regional changes, physical processes, potential dangers and resources available across the region (National Strategy for the Arctic Region 2013). A solid understanding of the physical environment will

enable further understanding of equipment limitations in the region. Ice thickness needs to be continually observed to support maritime vessels and operations, however satellite coverage is non-existent near the North Pole. The U.S. Navy assets and personnel can fill in the gaps in science and train in this environment in support of U.S. national interests.

II. PREVIOUS WORK ON SEA ICE

This chapter discusses Arctic sea ice thickness, the evolution of sea ice models and altimetric observations of ice freeboard. As discussed in Chapter I, the rapid decline of Arctic sea ice thickness can be indicative of both local and global climate changes. Climate models are continually being improved and observational records extended in efforts to understand the decline of sea ice thickness. The purpose of this section is to provide insight into the significance of sea ice thickness, sea ice models and observations. Sea ice thickness is discussed here to explain the challenges of accurately depicting Arctic sea ice volume from sea-ice models and from observations.

A. ARCTIC SEA ICE THICKNESS

Changes in Arctic and Antarctic sea ice extent can be discerned, however sea ice volume measurements over large distances and over longer times (i.e., interannual to decadal) are much more difficult to acquire. Understanding of sea ice volume changes is critical to understanding the rate at which sea ice is melting. Using ICESat records, a loss of 42% multi-year ice between 2004 and 2008 was estimated (Kwok et al. 2009). This rate of loss is much larger than the decrease in sea ice extent, which is about -13.4% per decade (NSIDC 2016). Changes in sea ice thicknesses can be attributed to advection, thermodynamics and mechanical processes (Thorndike 1975). The ice pack is continually moving, undergoing stress and strain. In regions of convergence, ridges develop, which increases sea ice thickness. In divergent regions, leads open, exposing warmer ocean waters below to cooling and new ice formation in winter, and lower surface albedos important for summer melt. Thermodynamically, the ice pack is influenced from both the ocean and atmosphere, which means sea ice thickness and volume vary with the change in season.

We discussed first-year and multi-year ice in Chapter I, and here the physics of their evolution is described. First-year ice thickens much faster than multi-year ice (Figure 15; Thorndike 1975). This is because first-year ice is typically thinner than multi-year ice, but may therefore not survive the summer melt season, unless it is subjected to

substantial ridging (Thorndike 1975). Arctic first-year ice is more susceptible to changes in atmospheric heat fluxes, corresponding to faster growth rates and onset of the freeze up cycle (Thorndike 1975). First-year ice starts to form as early as late August, where multi-year ice starts to accumulate basal ice and begins the growth cycle in November (Thorndike 1975; Perovich 2009). Similarly, during the melt season, first year ice melts sooner and faster than multi-year ice. The growth rates of both Arctic multi-year sea ice and first-year sea ice are illustrated in Figures 15 and 16. This is important to the changing Arctic environment because there is a shift from multi-year to first-year ice (Figure 8). Consequently, there may be longer periods and more expansive regions of open water in the near future within the central Arctic.

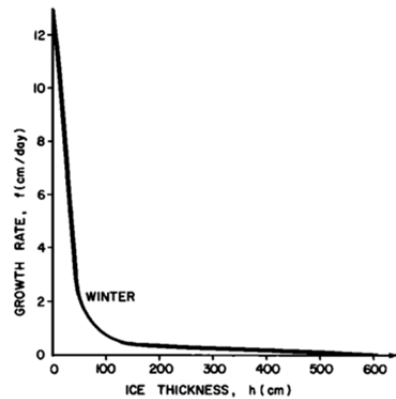


Figure 15. Central Arctic sea ice growth rates relative to ice thickness. Source: Thorndike et al. (1975). Sea ice growth rate, the thermodynamic thickening of sea ice, is dependent upon sea ice thickness. Thinner ice has a larger growth rate than perennial ice.

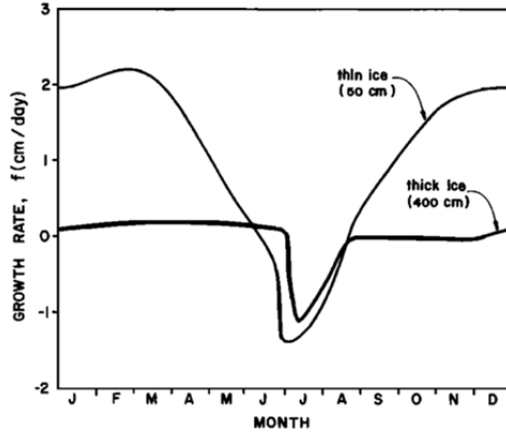


Figure 16. Monthly variation in sea ice growth rates for multi-year and first-year ice. Source: Thorndike et al. (1975). Thin sea ice responds to changes in the atmospheric heat fluxes faster than thicker ice for both the growth and melt phases. This is evident by the significantly larger growth and melt rates of thin ice, and earlier onset of each process, whereas the thicker ice responds to atmospheric fluxes at a much slower rate and at a later time period. The growth rate of thick sea ice does not increase until November, compared to thin ice, which begins the growth phase mid-August.

During the formation of sea-ice, salt and other impurities are rejected from the ice. This process decreases the density of the sea ice. Sea ice buoyancy may be approximated using Archimedes' principle. This states that a solid placed upon a denser fluid will displace a fluid mass equivalent to the mass of the solid under the force of gravity, and then remain at rest (Heath 1897). This explains how sea-ice is buoyed atop denser oceanic water, and may then remain in isostatic balance (Geiger et al. 2015). This isostatic assumption can be used to measure sea ice thickness by measuring its freeboard (Geiger et al. 2015). However, there are uncertainties introduced due to intra-seasonal changes in the density of sea ice and sea water, heterogeneous snow loading and snow density, and cavernous spaces between blocks of deformed ice in ridges, which are not always in local isostatic balance (Geiger et al. 2015).

Distribution and composition of sea ice thickness vary both temporally and spatially and can be described statistically with a thickness distribution over a given area, which we designate $g(h_i)$ (Thorndike et al. 1975; Figure 17). The Ice Cloud and Land

Elevation Satellite (ICESat), Operation IceBridge (OIB), and Cryosphere Satellite (CryoSat-2) data sets have been used to estimate basin wide Arctic sea ice thickness distributions. The Kwok and Cunningham (2012) analysis of the ICESat data focuses on estimation of ice thickness along ICESat ground tracks by converting surface elevation changes to sea ice freeboard, and then to ice thickness using Archimedes' Principle (Equation 1 in the next paragraph). Additional research has been conducted comparing and analyzing Cyrosat-2 measurements against ICESat, upward looking sonar measurements of ice draft, electromagnetic birds and IceBridge measurements of freeboard to further understand sea ice thickness (Hutchings et al. 2008; Kwok and Cunningham 2008). While such studies compare several data sets to one another to help reduce uncertainty in thickness estimates, the ice is assumed to be vertically homogeneous, which is not always true. However, in making this assumption, freeboard measurements can be converted into sea ice thickness as follows.

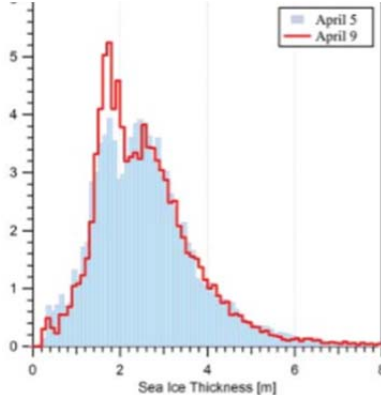


Figure 17. The sea ice thickness distribution $g(h_i)$. Source: Hutchings et al. (2008). On April 5 and 9, 2007, an airborne LASER altimeter took measurements of sea ice freeboard, while an electromagnetic bird was used to detect its draft, thus deriving the sea ice thickness distribution along survey lines in the Beaufort Sea. Due to sea ice deformation, a change in sea ice thickness distribution, or redistribution, was observed between the two days.

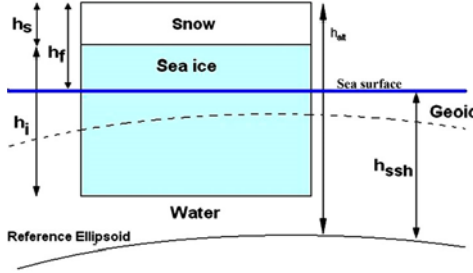


Figure 18. Variables used in the estimation of sea ice thickness from freeboard, h_f , which is designated with the fb symbol throughout this thesis.

Source: Teleti and Luis (2013).

Figure 18 depicts ice freeboard, h_f , from Teleti and Luis (2013), which we will designate fb in this thesis, derived from Archimedes' Principle:

$$fb = h_i \left(1 - \frac{\rho_i}{\rho_w} \right) + h_s \left(1 - \frac{\rho_s}{\rho_w} \right), \quad (1)$$

where h_i is sea ice thickness, ρ_w , ρ_i and ρ_s are the density of sea water, sea ice, and snow, respectively, f_b is freeboard of the ice and snow column floating in the water and h_s is freeboard snow thickness. From this equation, it is clear that accurate sea ice freeboard calculations are dependent upon accurate density and snow depth measurements, which fluctuate across Arctic Ocean and are locally heterogeneous.

B. SEA ICE THICKNESS UNCERTAINTY

The largest contributions to freeboard error comes from snow depth and ice density, which contribute up to 70% and 35% of the uncertainty in measurements, respectively (Zygmuntowska 2013). A small uncertainty in freeboard measurements can translate into large errors in sea ice thickness estimates. Though the role of snow is essential to maintaining sea ice thickness and multi-year ice floes by increasing the surface albedo of the pack, snow depth measurements across the Arctic are sporadic, at best. Even across short distances, snow depth distribution can vary significantly between seasons (Figure 19). In particular, snow depth measurements vary significantly between

the fall and winter seasons. In Warren's (1999) research, the average snow depth for the fall and winter seasons had averages of 8.7 centimeters and 28.9 centimeters, respectively, across a distance of 1000 meters. These differences in mean snow depths can have drastically different outcomes for sea ice thickness and sea ice mass quantities.

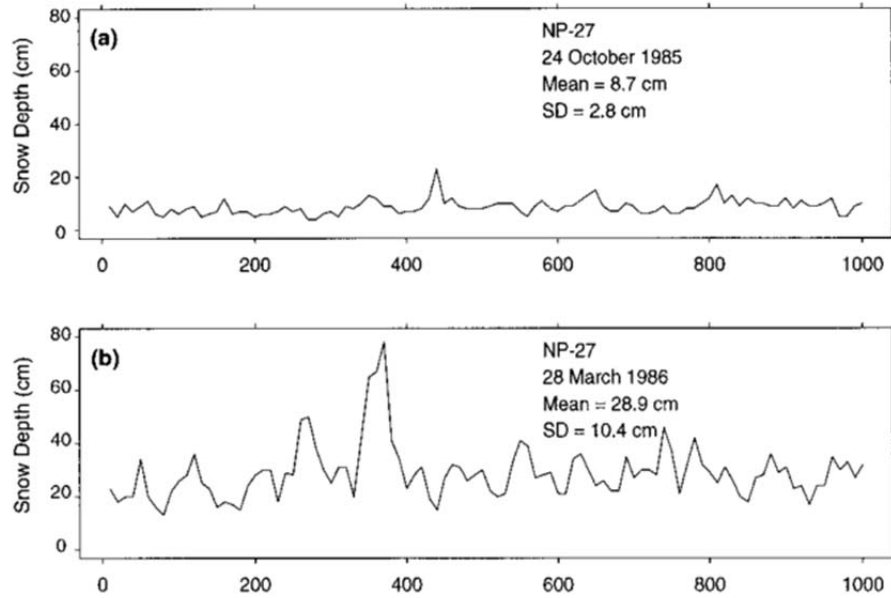


Figure 19. Snow depths along a sea ice transect in the Arctic, where the x-axis indicates transect distance in meters. Source: Warren et al. (1999). Snow measurements were conducted along a 1000-meter snow line in October 1985 and March 1986, representing the fall and winter seasons for snow accumulation. The mean snow depth for the winter is 28.9 cm, and for fall is 8.7 cm.

Actual snow depth distribution, variations in snow density and snow load quantities are not well known. A climatological record was developed by Warren et al. (1999; Figure 19) incorporating 37 years of snow depth data from drifting stations, providing insight into snow accumulation and melting months in addition to snow depth quantities. Warren's study indicated a weak negative trend in snow depths for all months with the largest downward trend for May. This study also indicated the largest snow depths are in the vicinity of hummocks, pressure ridges and sastrugi, which are regions where wind erosion has created ridge features upon the snow covered sea ice (Warren et al. 1999). Still, the depths of snow upon the aforementioned features vary spatially

(Warren et al. 1999). Since 1999, the Arctic has changed dramatically. Using Operation IceBridge (OIB) airborne radar measurements between 2009–2013, Webster et al. (2014) observed a decrease in snow depth of $37\pm29\%$ in the Western Arctic and $56\pm33\%$ in the Beaufort and Chukchi seas, relative to Warren et al. (1999) climatology.

In the summer, snow on the sea ice melts forming melt ponds or mushy layer. Snow density is also affected by winter wind packing (Kwok and Cunningham 2008). The albedo for melt ponds is less than sea ice with values ranging from 0.15-0.29 which allows for further absorption of incoming solar radiation and further melting through the summer season (Perovich 1996). During the winter, these pools refreeze and have a fresher salinity. At smaller scales with sea ice, brine inclusions and channels are ubiquitous (see also Figure 26 later in this chapter) Sea salt is rejected from ice crystal structure during ice formation, and as a column of sea ice develops, brine inclusions and channels are formed within it, consisting of the brine fluid, surrounded by solid-phase material. The brine, which is denser than the surrounding crystal solid, does not reach temperatures that would allow it to freeze, and therefore gravity drainage typically causes the gradual rejection of brine from the ice column into the ocean. This process is not instantaneous, and therefore sea ice has varying density resulting from the porosity associated with brine channels (Wadhams 2000).

C. A BRIEF SUMMARY OF OBSERVATIONS AND MODELING OF THE ARCTIC

Sea ice extent records, prior to satellite measurements, were obtained by observers aboard ships, aircrafts or *in-situ* measurements (Teleti and Luis 2013). Additionally, submarines have conducted ice thickness measurements using upward looking sonar (Teleti and Luis 2013). Creating these records has been limited by the inaccessibility of the Arctic environment, has been time consuming and has often lacked a standardized system for recording observations (Teleti and Luis 2013). *In-situ* observations often provide limited spatial and temporal resolution of sea ice across the Arctic Ocean, fueling uncertainty in sea ice thickness measurements and calculations. As technology advances, various scientific methods are being used to further understand the physical processes of the cryospheric environment, including attempts to recreate

historical records of sea ice, as well as use of altimetric observations and numerical models.

Arctic paleoclimatologists have recreated a time series of Arctic summer sea ice extent to determine if the reduced extent is anomalous or a cyclical process. Analyzing a time period of 1450 years up to the present decade, periods of relatively low and extensive ice coverage have been identified (Kinnard 2011). Potential forcing mechanisms of sea ice decay, including advection of warm air and the North Atlantic Oscillation bringing warmer waters to the Arctic, contribute to historical minimum sea ice extent values. However, the rapid 21st century decay of Arctic sea ice, exceeding the historical rate of decay (Figure 1 and Figure 2), suggests both anthropogenic and natural forces play a role in the recent decline of perennial Arctic sea ice volume (Kinnard 2011). Due to limited historical observations, with poor temporal and spatial resolution, measures to further understand the current state of the Arctic environment are essential.

D. ALTIMETRIC OBSERVATIONS

With the introduction of passive satellite microwave technology in the late 1970s, scientists were able to use regular measurements of microwave emissions from Earth's surface to better understand the seasonal variability of sea ice extent (Teleti and Luis 2013). The new satellite imagery provided spatially and temporally regular data of the world's oceans covered by sea ice. These passive microwave observations modernized cryospheric science by providing a continuous, well documented record of sea ice cover of the world's oceans. This record continues to be expanded today. Currently, using visible, infrared and microwave satellite imagery, sea ice extent data is available almost daily. While these records show an overall decline of Arctic sea ice extent, they do not provide insight into the changes occurring to sea ice thickness.

Altimetric measurements conducted from satellites and aircraft have sought to fix this problem, providing unprecedented intra-seasonal observations, aiding in the understanding of pack ice. Airborne and spaceborne altimeters measure changes in sea ice freeboard, *fb*, above the sea surface, where local differences in elevation correspond to changes in ice thickness and hence sea ice mass (Kwok et al. 2009). Even with the use

of aircraft and satellites, it is difficult to continually monitor sea ice thickness, due to limited spatial and temporal resolution. Though passive microwave imagery has been used since 1979 to monitor sea ice extent, sea ice thickness measurements from remote sensing instruments have only been used recently. It was not until 2003, with National Aeronautics and Space Administration's (NASA) launch of Ice, Cloud, and Land Elevation Satellite, (ICESat), that the first basin-scale estimates of sea ice thickness were conducted using satellite altimetry (Kwok and Cunningham 2007; Farrell et al. 2009).

1. ICESAT

ICESat was launched in January 2003, allowing NASA to collect surface elevation measurements of sea ice along its orbital tracks via the use of a LASER altimeter with an elevation accuracy of 14 cm (Abdalati et al., 2010; Kwok et al., 2007; Schutz et al., 2005; Zwally 2009). The Geoscience LASER Altimeter System (GLAS), mounted aboard ICESat, collected elevation data intermittently between February 2003 and October 2008 alternating between three LASERs, with both a red and green beam (Abdalati et al., 2010; Kwok et al., 2007). The red and green beams correspond to near infrared and visible wavelengths, respectively. Near infrared wavelengths are less sensitive to atmospheric conditions, such as clouds, as compared to green, visible wavelengths (Abdalati et al., 2010). To determine sea ice elevation, GLAS transmitted the LASER pulses (Figure 20), and counted the number of photons reflected back to the satellite to determine surface elevation (NASA, 2015). The data collected has been processed into estimates of freeboard and sea ice thickness. For the GLAS instrument, the horizontal sampling rate was 172 meters along track, with footprint resolution of approximately 65 meters (Abdalati et al., 2010; Kwok et al., 2007; Farrell et al., 2009) and 40 Hz sampling rate (Zwally 2002).

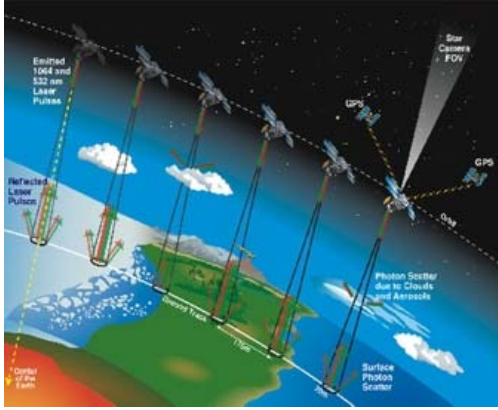


Figure 20. Depiction of ICESat collecting data along the orbital track. Source: NASA (2005). NASA's ICESat orbited the earth, using LASER to measure the travel time between the Earth's surface and the satellite. Along the path, the LASER path is affected by clouds, aerosols and differing surface types.

Limitations of ICESat included no coverage north of 86°N due to satellite inclination, which leaves the North Pole region void of data. Data collection periods during the ICESat mission were influenced by the presence of atmospheric clouds and aerosols, and also LASER malfunctions. Upon launch, the first two data collection periods, designated LASER 1A and LASER 1B, each had an 8-day repeat orbit for instrument calibration and validation (NSIDC, 2016). The first 10 days of LASER 2A conducted an 8-day orbit, and then cycled into a 91-day repeat orbit. The remaining operations used a 91-day repeat orbit, meaning that ground tracks were repeated approximately every three months. ICESat's 91-day repeat orbit comprised of 1354 along ground tracks, approximately 14.8 tracks per day (NSIDC, 2016). Operational LASER malfunctions led to varied temporal resolutions for each individual data collection campaign, instead of full year round coverage, as summarized in Table 1. Data collection durations varied in length, between 12 to 55 days, for all campaigns between 2003 and 2008 (NSIDC, 2016). While the ICESat mission was not able to monitor sea ice continually for these 5 years, the orbit configuration increased sea ice coverage by 15% of total winter sea ice (Farrell et al., 2009).

Figure 21 shows an image of a twelve-day period of actual data collected from GLAS. From this image one can see the coverage provided, as well as the breaks in individual orbit retrievals resulting from atmospheric or surface disturbances.

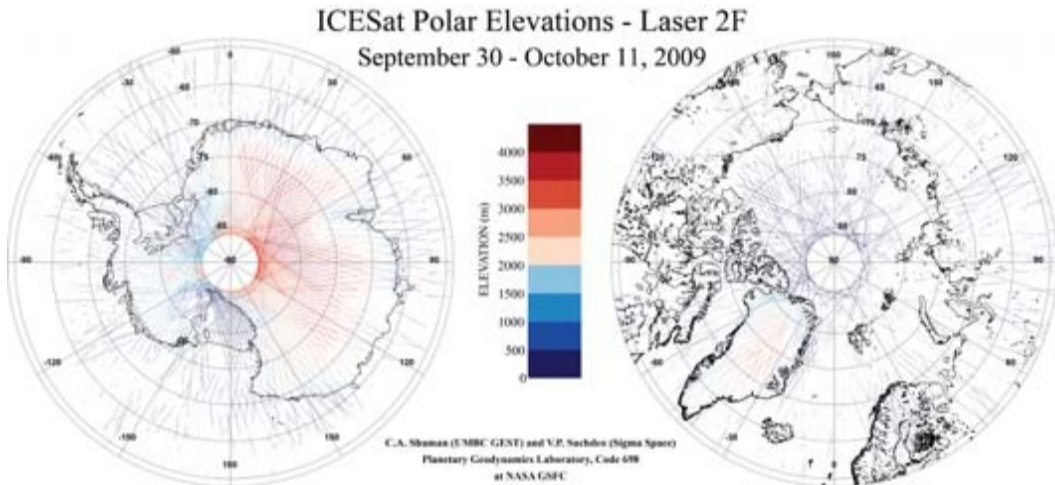


Figure 21. ICESat Surface Elevations for the 2009 fall orbital period. Source: NSIDC (2014). ICEat measured sea surface elevations across the polar regions along its orbital track. The color scale depicts surface elevation height in meters; white space is void of satellite coverage. Gaps in satellite coverage are noted by the break in ground tracks.

While the instrument was unable to make continuous, year round elevation measurements along each track, the ICESat mission helped improve the knowledge of spatial changes in Arctic sea ice thickness. Table 1 summarizes the 14 individual ice freeboard data campaigns relevant to this thesis. They include 6 spring seasons, 2 summer seasons and 6 fall seasons.

Table 1. ICESat campaign time periods and associated LASERs. Source: NSIDC (2016) and NASA (2016b). This table highlights ICESat operational dates, duration, LASER used to conduct sea surface elevation measurements and repeat orbit. The table is color coded to represent each season. Orange represents fall operations, blue is spring and green is for the summer operations. Gray represents data used in analysis presented later in this thesis.

Campaign Start	Campaign End	Operational Days	LASER Used	Repeat Orbit	Data used in Emulator
2003-02-20	2003-03-29	38	1	8 day	No
2003-09-25	2003-11-19	8	2A	8 day	No
2003-10-04	2003-11-19	45	2A	91 day	No
2004-02-17	2004-03-21	34	2B	91 day	Yes
2004-05-18	2004-06-21	35	2C	91 day	No
2004-10-03	2004-11-08	37	3A	91 day	Yes
2005-02-17	2005-03-24	36	3B	91 day	No
2005-05-20	2005-06-23	35	3C	91 day	No
2005-10-21	2005-11-24	35	3D	91 day	No
2006-02-22	2006-03-28	34	3E	91 day	No
2006-05-24	2006-06-26	33	3F	91 day	No

2006-10-25	2006-11-27	34	3G	91 day	No
2007-03-12	2007-04-14	34	3H	91 day	Yes
2007-10-02	2007-11-05	37	3I	91 day	Yes
2008-02-17	2008-03-21	34	3J	91 day	No
2008-10-04	2008-10-19	16	3K	91 day	No
2008-11-25	2008-12-17	23	2D	91 day	No
2009-03-09	2009-04-11	34	2E	91 day	No
2009-09-30	2009-10-11	12	2F	91 day	No

2. Operation IceBridge

Operation IceBridge (OIB) is a NASA led mission involving the use of aircraft with a mounted altimeter instrument measuring sea ice elevation along the flight path (Farrell et al., 2012). OIB supports ongoing NASA cryospheric data collection operations in polar regions in between ICESAT and the upcoming ICESat-2 mission, and has been conducted annually since 2009 (Kurtz et al., 2013). Arctic sea ice freeboard measurements are collected by OIB during the spring season, at the beginning of the melt season. OIB uses the Airborne Topographic Mapper (ATM), a Light Detection And Ranging (LIDAR) instrument, to measure sea ice freeboard. (Donghui et al., 2015; NSIDC, 2016; Farrell et al., 2012; NASA, 2012). The ATM revolving path (Figure 22) is 250 m and LASER footprint of about 1 m to 4 m, depending on the altitude of the plane, with surface diameter of 3–4 m (Farrell et al., 2012; Kwok et al., 2012).

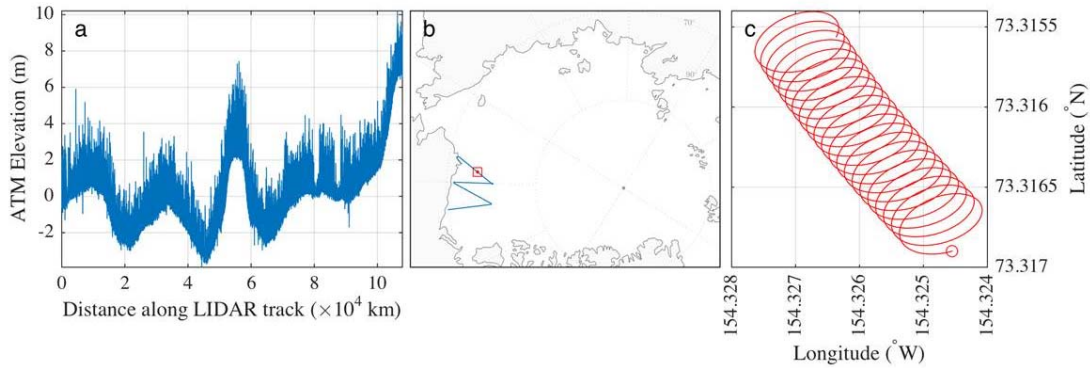


Figure 22. Airborne Topographic Mapper Scan 24 March 2013. Source: Andrew Roberts (2015). Figure (a) is the surface elevation measurements taken by the ATM aboard the OIB flight on 24 March 2013. The dataset plotted is ILNSA1B. Figure (b) is the flight track. Figure (c) represents the red square overlying a portion of the track in (b), which indicates the leading direction of the subsection of the ATM scan.

The OIB footprint diameter varies with the aircraft altitude, which ideally operates at approximately 500m above sea level, and the ATM measures topography to an accuracy of 10 cm-20cm (NASA, 2012). So called “Quicklook” data is made available via the U.S. National Snow and Ice Data Center (NSIDC) soon after each flight. In this thesis, we will analyze 43 individual OIB flights (Figure 18) between the years 2009 and 2015 from the Quicklook product.

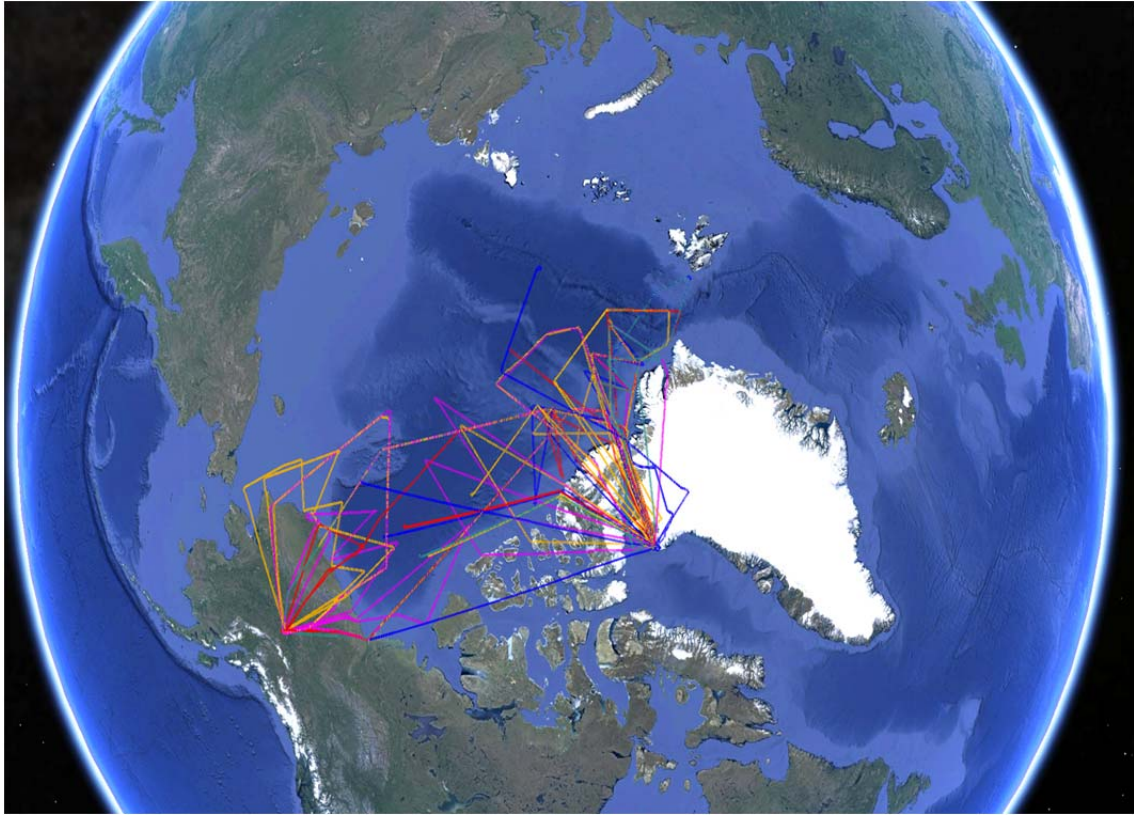


Figure 23. OIB flight tracks across western Arctic 2009–2015. Source: NSIDC (2016). Flights were flown during the annual spring season, to provide altimetric measurements of sea ice freeboard following winter freezeup. Depicted are the tracks from 43 OIB flights. ICESat-2

3. ICESat-2

Estimating sea ice thickness from freeboard measurements is a primary objective for the upcoming ICESat-2 mission. The impending mission launch date is December 2017, which will provide coverage up to 88°N. ICESat-2 will also have a 91-day repeat orbit with a pulse repetition frequency of 10kHz for photon counting (Abdalati et al., 2010). The 91-day repeat orbit will allow continuous, intra-seasonal observations of the sea ice. The on ground LASER footprint will be 10 meters in diameter, taking measurements every 70 centimeters along the ground track (Abdalati et al., 2010).

A significant difference in the ICESat-2 LASER configuration as compared to ICESat's GLAS is the use of Advanced Topographic LASER Altimeter System (ATLAS), which will consist of two LASERS, with one as a backup. Differing from

GLAS, the ATLAS LASER will be split into 3 pairs of LASER beams, six in total. Each pair will consist of one weak and one high energy beam. The three pairs will be spaced by about ~ 3 km when incident at the sea surface, with a 90-meter spacing between the paired high and low energy beams (Abdalati et al., 2010). The additional beams and new configuration will provide increased spatial coverage relative to GLAS on ICESat and improved accuracy of ± 3 cm for freeboard (Abdalati et al., 2010).

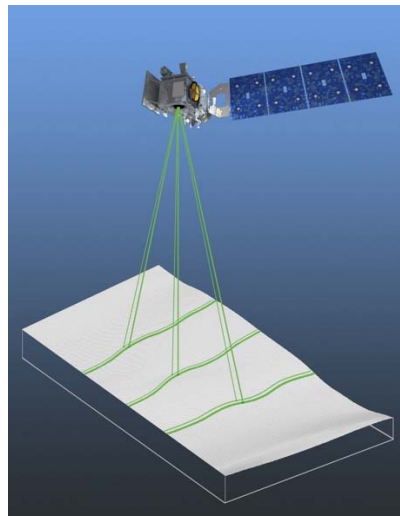


Figure 24. Schematic of ICESat-2 LASER footprint along track. Source: NASA (2016a). ATLAS will generate three pairs of LASER beams, improving sea ice coverage and elevation estimates.

E. SEA ICE MODELS

Current observations provide insufficient spatial and temporal coverage. Few details of sea ice volume, local thickness distribution of sea ice and snow, and melt-pond coverage are inferred from the observations, all of which are critical to properly understand climatic changes occurring across the Arctic Ocean. For this reason, numerical models have been developed to help gain an understanding of physical interactions that may lead to seasonal and climatic changes in Earth's polar regions. Numerical models of polar regions are continually refined and attempt to simulate the physical processes of the sea ice development by computationally integrating governing geophysical fluid models. The models attempt to simulate the processes of sea ice

development to determine the cause of sea ice decline as well as resolve interactions that are not readily observable.

Modeling of sea ice requires not only an understanding of the atmospheric and oceanic variables driving the formation, drift, deformation and melt of sea ice, but also the physics and characteristics of sea ice present. Many small-scale processes, related to sea ice thermodynamics, dynamics and interactions across the air-ice and ice-water interfaces are not well modeled in global climate models (GCM) due to their low resolution (IPCC, 2013). Sea ice models rely on parameterizations that are sometimes poorly supported by observations. Sea ice, ocean and atmospheric processes are closely coupled and are highly variable both temporally and spatially. To accurately represent these processes, many input parameters would be required (Hunke et al., 2015). It is important to note that with each added variable, there is a degree of error that may increase total error within the model. Individual physical processes, variables and parameters of sea ice need to be well understood and analyzed before coupling with other processes to enhance sea ice model capabilities. However, it is difficult to quantify potential errors from each individual processes.

Understanding the limitations of the modeled sea ice physics and maximizing effectiveness of observations will help focus and promulgate the requirements needed to accurately categorize and incorporate small scale sea ice processes within numerical models (Maslowski et al., 2012). The initial inputs, implemented boundary conditions, or even computational constraints all have large impacts on modeled sea ice morphology.

1. Advances in Sea Ice Modeling Since 1970

The observed transformations of Arctic sea ice are governed by dynamic and thermodynamic processes (Perovich and Richter-Menge 2009). Thermodynamic processes involve varying surface energy fluxes, resulting in sea ice growth and melt. Sea ice dynamics pertain to the movement of the sea ice floe. Sea ice motion is influenced by surface wind forcing, ocean stress, Coriolis force, sea surface tilt and internal ice stresses (Perovich and Richter-Menge 2009). Sea ice models have evolved to incorporate sea ice physics, including both thermodynamic and dynamic computations.

a. Thermodynamics

Maykut and Untersteiner (1971) describe a one-dimensional sea ice model that accounted for vertical changes in snow cover, ice salinity parameters, and energy fluxes due to incoming solar radiation. Focusing on the sea ice thermodynamics, this model assumed sea ice was a homogeneous slab, in which initial conditions were set for snow depths, albedo, salinity and energy fluxes. The upper surface energy budget is:

$$(1-\alpha)F_r - I_o + F_L - \varepsilon_L \sigma T_o^4 + F_s + F_l + F_c = \begin{cases} 0, T_0 < 273.15 K \\ -\left[q \frac{d}{dt} (h_i + h_s) \right] \end{cases} \quad (2)$$

Table 2. Thermodynamic notation for Equation 2

Term	Meaning
α	Surface albedo
F_r	Downward shortwave radiation
I_o	Downward Radiative energy passing through ice
F_L	Downward Longwave radiation
ε_L	surface emissivity
σ	Stefan-Boltzmann Constant
T_0	Surface Temperature
F_s	Sensible heat flux
F_l	Latent heat flux
F_c	Net heat conduction through the ice and snow column
q	Latent heat of fusion of the surface material
h_s	Snow thickness
h_i	Ice thickness

This equation includes radiative fluxes, turbulent fluxes and conduction through the ice-snow column, with notation given in Table 2. Sea ice growth and melt is dependent upon interactions with the atmosphere and ocean, as illustrated in Figure 26. Using a downward positive sign convention for fluxes, when the sum of the fluxes is negative, sea ice will grow; when the sum is positive, sea ice melts (Perovich and Richter-Menge 2009). The spatially varying ice thickness distribution, $g(h_i)$, is important to the heat budget for this model affecting heat loss quantities (Thorndike et al., 1975). The ice thickness distribution is vital to the heat exchange between the atmosphere-ocean-sea ice layers. Leads and thin ice absorb incoming solar radiation, leading to warmer ocean temperatures. Leads are also regions of oceanic heat loss to the atmosphere, accounting for nearly 50% of oceanic heat loss (Thorndike et al., 1975). The thickness distribution of sea ice is important to sea ice dynamics and will be discussed in the next section.

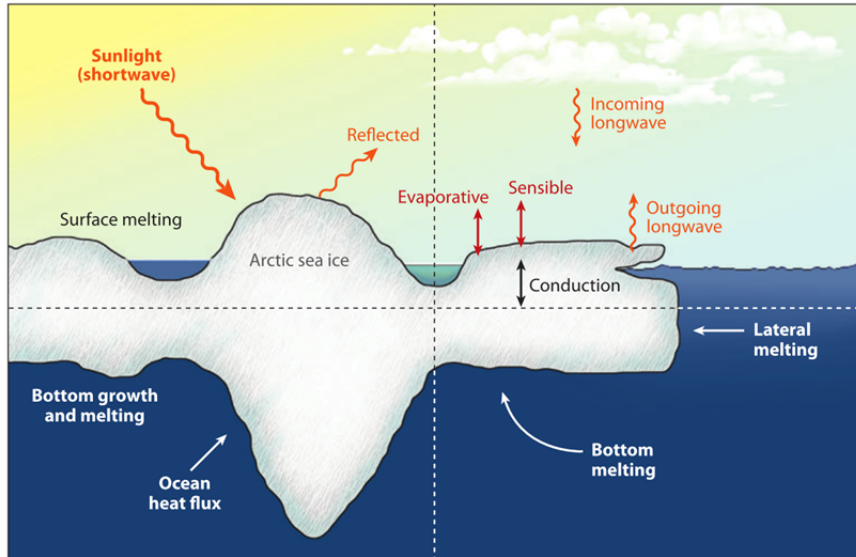


Figure 25. Sea Ice surface heat budget. Source: Perovich and Richter-Menge, (2009). Radiative and turbulent heat fluxes are primary contributors to sea ice growth and melt. Sea ice melt is omnidirectional, while growth is downward. Radiative fluxes are annotated in orange, turbulent fluxes in red.

There have been many enhancements to thermodynamic models since Maykut and Untersteiner (1971). An energy-conserving model was developed to account for the heat capacity of sea ice by Bitz and Lipscomb (1999). This research compared energy conserving and non-conserving models for both a zero-layer and three-layer model, introducing variation in salinity profiles, albedo and porosity differences (Bitz and Lipscomb 1999). The zero-layer model overestimated sea ice thickness by 50%, whereas the three-layer model over estimated by 5% for energy conserving model, and 15% for the non-conserving model (Bitz and Lipscomb 1999). Brine pockets (Figure 26) which are present throughout sea ice, influence the specific heat of the ice layer and affect the amount of energy required to melt the sea ice. Therefore, they should be modeled where possible.

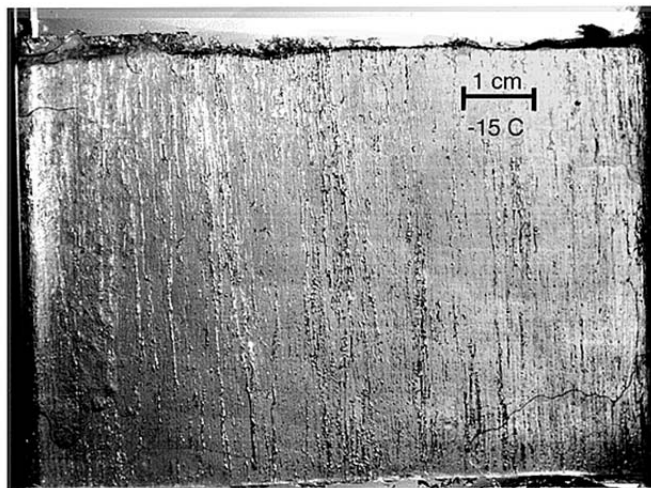


Figure 26. Image of brine pockets in first year ice. Source: Light et al. (2003).

Brine inclusions and gas bubbles are visible, which change the density and specific heat of sea ice.

Several physical processes influence the bulk salinity of sea ice, including melting, freezing, gravity drainage and melt pond flushing (Turner and Hunke 2015). By applying ‘mushy layer’ thermodynamics in a sea ice model, Turner and Hunke (2015) were able to simulate these effects. This is the most recent generation of sea ice thermodynamic model, and is used in this thesis to help resolve seasonal and spatial variations of sea ice salinity and its effects on sea ice thickness.

b. Dynamics

As already mentioned, sea ice dynamics is important for building thick, ridged ice in the Arctic. Most sea ice away from coastal regions is almost always in motion due to inertia and four forces: wind stress, ocean current stress, internal ice stress and ocean sea surface tilt (Hibler 1979), as illustrated in Figure 27. The dynamic processes of sea ice involve feedbacks between ice deformation, transport, the sea ice thickness distribution and applied mechanical stresses from the atmosphere and ocean (Thorndike et al., 1975).

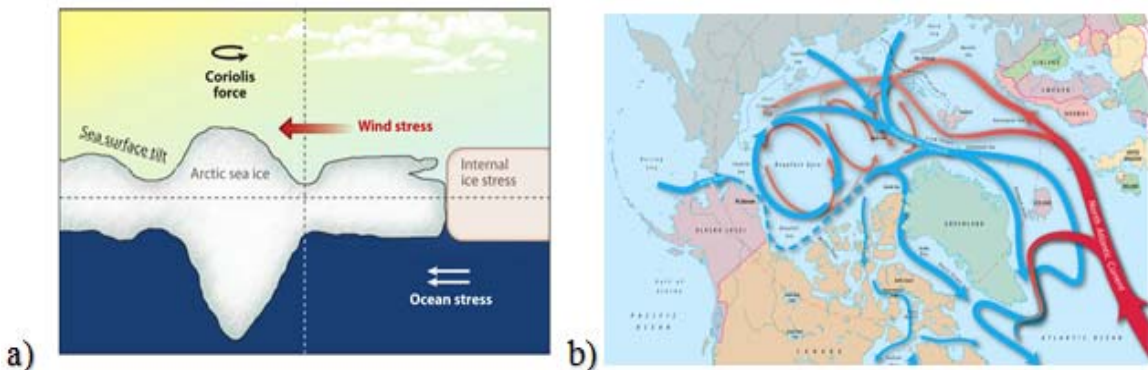


Figure 27. Mechanical forcing of Arctic sea ice from (a) Source: Perovich and Richter-Menge (2009), (b) Source: Jack Cook, Woods Hole Oceanographic Institute. Four forcing mechanisms, as well as the Coriolis force, influence the motion of sea ice as seen in (a). Wind forcing and ocean currents transport sea ice across the Arctic Basin is seen in (b). Sea ice motion is dependent upon wind and current speed, ice roughness and drag.

Hibler (1979) created one of the first Arctic sea ice dynamic and thermodynamic models, best known for its sophisticated treatment of internal ice. The model introduced an isotropic viscous-plastic constitutive law for sea ice to represent the horizontal internal ice force vector, F , based upon sea ice thickness distribution $g(h_i)$. However, for the Hibler (1979) model, $g(h_i)$ was simplified into just two thickness categories divided at 0.5m. The model integrated the sea ice momentum balance, relating ice mass per unit area, m , the Coriolis parameter, f , ice-water and air-ice stresses, τ_w and τ_a respectively, and sea surface tilt, ∇H , with the sea ice horizontal velocity, u , as follows:

$$m \frac{Du}{Dt} = -m f k \times u + \tau_a + \tau_w - mg \nabla H + F \quad (3)$$

In many sophisticated sea ice models, this is solved in conjunction with sea ice thermodynamics as previously described, which are then used to solve for continuity of the thickness distribution:

$$\frac{\partial g(h_i)}{\partial t} = \nabla \cdot (g(h_i)u) + \psi(h_i) + F(h_i) \quad (4)$$

where $\psi(h_i)$ is the rate of mechanical redistribution and $F(h_i)$ is thermodynamic growth or decay rate.

With the momentum balance equation and constitutive law for F , this equation can be used to predict the movement of ice over time t . The sea ice thickness distribution is important to the energy budget between sea ice and ocean boundary layers (Thorndike et al., 1975). Ice strength is also dependent on the thickness distribution and varies seasonally. Using this approach, daily, seasonal and climatic changes in ice thickness can be modeled across the Arctic basin, and that is the approach used in the model assessed in this thesis.

Parkinson and Washington (1979) developed a sea ice model around the same time at Hibler (1979) that modeled thermodynamic and dynamic processes of sea ice except for a sophisticated rheology, which was Hibler's main 1979 contribution. Rather than focusing on sea ice dynamics, Parkinson and Washington's 200 km resolution model demonstrated the importance of coupling sea ice simulations with the atmosphere and ocean, albeit in a simplified way. Coupled sea ice modeling allows for more accurate incorporation of wind stress, sea surface temperatures and advection of model ice by reproducing atmospheric and oceanic events that can drive changes in sea ice (Parkinson and Washington 1979).

Over the last forty years, Hibler's 1979 sea ice model has been the foundation for many other subsequent sea ice models, and the demonstration of coupling by Parkinson and Washington (1979) initiated the use of sophisticated sea ice models in climate

simulations. Further research incorporated an elastic element to the sea ice constitutive equation to enhance computational efficiency (Hunke and Dukowicz 1997). This Elastic-Viscous-Plastic (EVP) assumption applied to sea ice dynamics accounts for Viscous-Plastic sea ice deformation modeled by Hibler (1979), but with a small added elastic component that offers an efficient solution of the sea ice momentum equation on massively parallel supercomputers, including those used by the Navy to forecast sea ice state.

Some recent sea ice models use an anisotropic rheology assumption for sea ice behavior across the Arctic basin as a potential improvement upon the isotropic assumption. The foundation for this anisotropic assumption is to add “realism” to the model, and depict anisotropy seen in satellite imagery and the geometry of ice floes (Tsamados 2013). Ice floes can change shape through interactions with other floes and from thermodynamic processes. Observations show the intersection angle between leads is about 30–40 degrees (Figure 28), which is indicative of anisotropy (Tsamados 2013). Additionally, use of the anisotropic sea ice mechanics can result in reduced ice drift speed in the Beaufort Gyre and Transpolar Drift (Figure 27b), while increasing simulated thickness due to deformation, ridging and sliding during the winter and spring seasons, which compares relatively well with observations (Tsamados 2013).

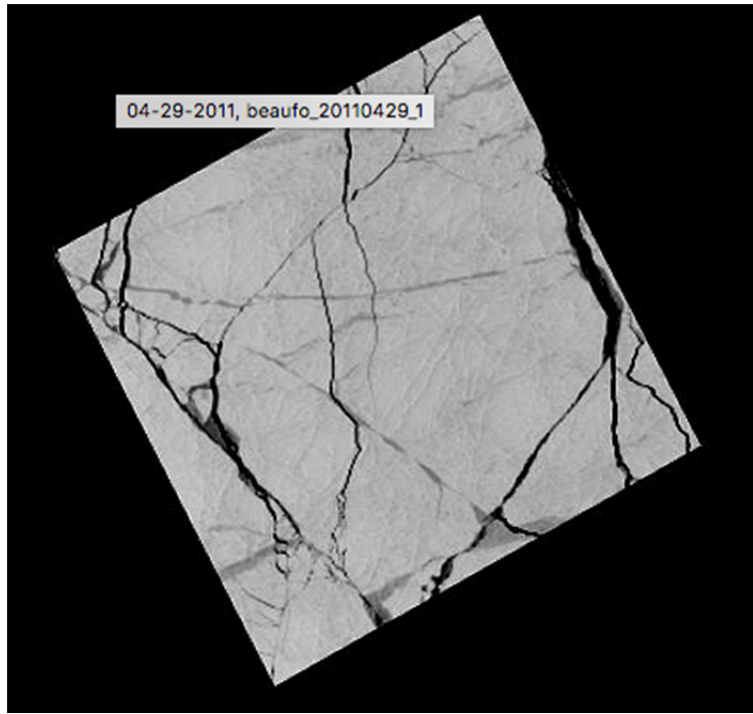


Figure 28. Anisotropic ice flow in the Beaufort Sea, April 29, 2011. Source: Global Fiducials Library (2015) Angles between leads that are formed across ice floes are often 30° to 40° .

In addition to the recent advances in ice thermodynamics and dynamics discussed here, recent research has focused on simulating specific, smaller scale sea ice processes, and their impact upon the large scale (Arctic Basin). These processes include optical scattering affecting ice and snow albedo, snow redistribution on ice, and changes in melt ponds (IPCC, 2013).

2. LIMITATIONS OF COUPLED MODELS

These advancements in sea ice models has enabled researchers to further understand key elements of sea ice physics, but each model and theory has its own limitations and biases (IPCC, 2013). Within numerical models, sea ice interactions with the atmosphere and ocean are often poorly represented (IPCC, 2013). This is supported by the observed rate of sea ice decline in the Arctic more often exceeding the rates projected by climate models than not. To better understand how models handle the

complex environment of the Arctic, ensemble averages are often required to quantify internal variability.

The World Climate Research Programme Coupled Model Intercomparison Project (WCRP/CMIP) was established in 1995 for improving general circulation models (CMIP 2009). The Coupled Model Inter-comparison Project Phase 5 (CMIP5) compared modeled Arctic sea ice extent trends for the years 1850–2100 and compared the results to satellite records from 1979–2005. By incorporating anthropogenic emissions into the models' radiative forcing, the multi-model ensemble tracked, with some degree of accuracy, the historical observations of Arctic sea ice extent (Stroeve 2012). Without the anthropogenic forcing, the world's top performing climate models failed to reproduce the same downward trend in Arctic sea ice extent.

These models are now collectively capable of reproducing sea ice extent to an accuracy of $\pm 10\%$, and project a steep rate of decline in Arctic sea ice (IPCC, 2013). The models suggest Arctic ice cover becoming seasonal, around 2045, where nearly the entire ice cover will be just first year ice (IPCC, 2013). The CMIP5 analysis also indicates that more than 50% of the decline in sea ice extent occurring between 1979 and 2011 is due to anthropogenic forcing (Stroeve 2012). Stroeve acknowledged the strength of the models is dependent upon sea ice processes, observations, how the models handle natural climate variability. More importantly, there these results analyzed sea ice *extent*, whereas a perhaps more meaningful metric is sea ice thickness.

Given these caveats, it is essential to understand how well models perform in simulating thickness. Models have limitations and historical satellite imagery has provided a 2-dimensional perspective of the sea ice (Maslowski 2012). To fully understand the 3-dimensional view of sea ice in models, research is required to quantify how well ice volume is simulated. In this thesis, we used a sophisticated, coupled regional climate model to investigate this question.

3. Los Alamos Sea Ice Model (CICE) and Its Use in This Study

The Regional Arctic System Model (RASM) used in this study, and described in the next chapter, uses the Los Alamos Sea ice model version 5 (CICE5) in a fully coupled

regional climate model framework. CICE5 incorporates some of the latest available sea ice model thermodynamics and dynamics discussed earlier, and can also be used to simulate chemistry and biological processes in sea ice. This model is typically run on parallel supercomputers. Its physics options include: the previously discussed mushy-layer sea ice thermodynamics of Turner and Hunke (2015), the Elastic-Viscous-Plastic (EVP; Hunke and Dukowicz 1997) or the Elastic Anisotropic Plastic (EAP) rheology of Tsamados et al. (2013), surface radiation scattering by snow (Briegleb and Light (2007), explicit melt ponds (Hunke et al. 2013), and a thickness distribution with five default thickness categories to approximate $g(h_i)$, with thickness bounds at 0.65, 1.39, 2.47 and 4.56 m (Hunke et al., 2015). Yet there remain fundamental difficulties in quantitatively evaluating forecast skill of this model, particularly in the sea ice thickness distribution (Hunke et al. 2015), and this thesis focuses particularly on this topic.

F. INTENT TO STUDY

With the upcoming launch of ICESat-2, there is motivation to make better use of spaceborne LASER altimeters to try to improve on the knowledge gap in our understanding of model ice thickness predictions. This thesis describes one small step to address this problem, by developing a capability to regularly use altimetric freeboard measurements from LASERs to quantitatively evaluate the skill of modeled sea ice thickness. The methods used in this thesis can be applied to the design of an “ICESat-2 emulator” described in the following chapters and could be built to run in CICE for operational Navy forecasts. It would enable skill scores to be extracted from model simulations to quantify the ability of CICE to represent sea ice thickness in both the Arctic and Antarctic using measurements from both ICESat, and, when it is launched, ICESat-2. For the current study, we just focus our attention to the Arctic, which has particular Naval significance, as detailed in Chapter I. We will also make use of IceBridge observations as part of this work. However, there are several other datasets of sea ice freeboard or draft that are not being used in this thesis. Only brief mention was made of CryoSat-2, which is currently providing routine measurements of ice freeboard globally (Tilling et al. 2015), but does not use LASERs, and so is beyond the scope of this thesis. In addition, there is a high quality dataset of submarine draft profiles of sea ice

(e.g. Lindsay 2010), declassified for parts of the central Arctic. These measurements, too, are not included in the ensuing analysis. However, the methods of analysis discussed herein could be applied to both CryoSat-2 and submarine profiles in future, in the latter case solving for draft and instead of freeboard. Now, with this defined scope of the thesis, a method for evaluating models now follows.

THIS PAGE INTENTIONALLY LEFT BLANK

III. MODEL DESCRIPTION AND METHODS

A. OBJECTIVE

In the previous chapter, we reviewed three core equations solved by pan-Arctic and global sea ice models, and discussed the skill of coupled models in simulating Arctic sea ice. This chapter discusses the methods used to evaluate sea ice thickness in models using the LASER altimeter measurements discussed in Chapter II. The methods described here are specific to high-resolution sea ice models with horizontal grid spacing of 10km or less, but could in future be generalized to lower-resolution global climate models. Using a high-resolution model is the easiest starting point for this work, because it resolves scales closest to those observed by satellites. We begin with a description of the Regional Arctic System Model (RASM) output as used in later chapters. We then discuss how freeboard measured along satellite ground tracks can be statistically compared with model freeboard derived from the modeled $g(h_i)$. This method thus serves as a proxy for evaluating modeled sea ice thickness.

B. THE REGIONAL ARCTIC SYSTEM MODEL

The Regional Arctic System Model is a fully coupled, high-resolution model developed at the Naval Postgraduate School in collaboration with the University of Colorado, University of Washington, Los Alamos National Laboratory, Iowa State University and the University of Arizona. The RASM ice-ocean component has a horizontal resolution of $1/12^\circ$ (~9 km). This is significantly more resolute than typical CMIP5 GCM sea ice grids discussed in Chapter II, which have resolutions on the order of 100 km. (Roberts et al., 2015; IPCC, 2013). With an overall temporal resolution of 20 minutes for the sea ice model (Table 3) RASM's sea ice output can be compared with hourly observations (Roberts et al., 2015). The full RASM ice-ocean domain extends beyond the Arctic Ocean, but we will focus only on the Central Arctic (black, Figure 29).

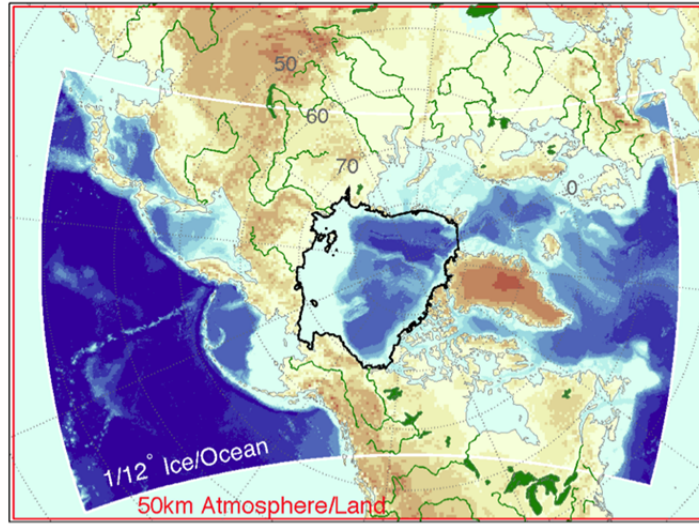


Figure 29. RASM domain. Source: Andrew Roberts, Naval Postgraduate School, (2015). The red line bounds the atmosphere-land domain with 50 km grid cells. The white line surrounds the ice-ocean domain with approximately 9 km grid cells and green represents major rivers and lakes delivering runoff to the ocean. The black line is the Central Arctic analysis domain, the focal region of this thesis. Blue shades detail bathymetry with the ocean domain, while orange and yellow hues indicate topography gradation.

RASM includes the Weather Research and Forecasting model (WRF; Cassano et al. 2016), the Variable Infiltration Capacity model (VIC; Hamman et al. 2016), the Parallel Ocean Program (POP; see Maslowski et al. 2012) and Los Alamos Sea Ice Model (CICE; see Roberts et al. 2015, with updates to CICE Version 5 detailed in Hunke et al. 2015). The WRF model is a high resolution, meso-scale numerical weather prediction model developed by the National Center for Atmospheric Research, (NCAR). The University of Washington developed VIC, which is a macro-scale, hydrologic model that provides runoff to the ocean (Liang et al., 1994). POP, developed at Los Alamos National Laboratory (Smith et al. 1992; Dukowicz and Smith 1994), is an energy-conserving ocean model that solves the three-dimensional primitive equations for fluid motion on the sphere under hydrostatic and Boussinesq approximations. CICE was discussed previously in Chapter II, but here we describe the configuration of CICE as used in RASM for this thesis, especially the sea ice model, because it is relevant to results

analyzed in Chapter IV, and the way in which freeboard measurements may be converted into “model equivalent” quantities.

Table 3. RASM configuration. This table provides the spatial and temporal resolution of RASM. Source: Roberts et al. (2015, table 1)

Component	Code	Configuration
Atmosphere	WRF3	50 km, 40 levels, 2.5 min time step
Land	VIC	50 km, 3 soil layers, 20 min time step
Ocean	POP2	1/12°, 45 levels (7 in the top 42 m), 10 time steps per 20 min flux exchange
Sea ice	CICE4	1/12°, 5 thickness categories divided at 0.65, 1.39, 2.47, 4.56, 9.3 m 4 thermodynamic ice layers per category and 1 snow layer 20 min thermodynamics and 2 min dynamics time step
Coupler	CPL7x	Flux exchange every 20 min for all components

The mean model freeboard for each grid cell is calculated using the following equations:

$$\overline{fb}_{model} = fb(\overline{h}_i, \overline{h}_s) = \overline{h}_i \left(1 - \frac{\rho_i}{\rho_w} \right) + \overline{h}_s \left(1 - \frac{\rho_i}{\rho_w} \right) \quad (5)$$

where

$$\overline{h}_i = \int_0^{\infty} h_i g(h_i) dh_i \approx \sum_{n=1}^5 h_{ni} A_n$$

and

$$\overline{h}_s = \int_0^{\infty} h_s g(h_s) dh_s \approx \sum_{n=1}^5 h_{ns} A_n$$

given the sea ice thickness distribution $g(h_i)$ and snow thickness distribution $g(h_s)$. CICE used in this configuration only uses one mean snow thickness, h_{ns} unique to and on top of each of the five sea ice thickness categories h_{ni} given $n = 1, 2, \dots, 5$. Recall from

Chapter II that these are divided at 0.65, 1.39, 2.47 and 4.56 m. Each ice category occupies an area A_n in a single model grid cell. The modeled sea ice concentration in each grid cell is thus given by:

$$A = \sum_{n=1}^5 A_n$$

Using the five thickness categories, $g(h_i)$ can be discretized using methods discussed by Lipscomb (2001). The best way to evaluate freeboard in a model is to construct a mean observed freeboard \overline{fb}_{obs} to compare with mean model freeboard \overline{fb}_{model} . To do this, the disparity between model and observational spatial resolution must be sufficiently similar. RASM, using the spatial resolution at about 9 km, equivalent to 1/12° on a rotated sphere grid with equator passing through the pole, is a good tool for this test due to the high spatial resolution.

The ice and snow thickness distributions, $g(h_i)$ and $g(h_s)$, are predicted quantities in RASM. In addition, ice and snow density, ρ_i and ρ_s , are held constant in RASM, and therefore \overline{fb}_{model} is easily calculated for each 20 minute time step of CICE in RASM. Due to the fact that $g(h_i)$ and $g(h_s)$ vary infinitesimally in the model over an hour, we have analyzed hourly instantaneous fields of \overline{fb}_{model} in this thesis in order to reduce the quantity of data required if one were to analyze every single 20 minute time step of CICE in RASM. Also, in order to determine the impact of surface snow in the modeled freeboard, we conduct a twin analyses in subsequent chapters of \overline{fb}_{model} and $\overline{fb}_{model}(h_s = 0)$, the latter case indicating that snow is not included in the freeboard calculation. Analyzing results of \overline{fb}_{model} and $\overline{fb}_{model}(h_s = 0)$ in tandem is a convenient way to quantify the contribution of modeled snowfall and surface snow physics on simulation skill. In a fully coupled model such as RASM, this is important, because sea ice freeboard is not just an indication of sea ice model skill, but also in the skill of the atmospheric model to deposit snow on sea ice, and of the coupled model system in representing the hydrologic cycle.

C. ICESAT-2 EMULATOR

A key purpose of this research is to understand how best to construct compatible values of \overline{fb}_{obs} and \overline{fb}_{model} for each model grid cell so as to use them in metrics of model performance in a statistically meaningful way. Satellite and aircraft observations of freeboard have a small footprint when compared to a ~9 kilometer grid cell (see Chapter II). Here we look to determine how to optimize the use of observational data and compare them to the model output and potentially increase the use of narrow tracks of LASER measurements across sea ice to be applicable to a broader swath of RASM model grid cells in the vicinity of a satellite ground track.

To gain an initial appreciation of the problem, an ICESat-2 sampling algorithm was constructed using MATLAB. For the purpose of this thesis, we will call this the “ICESat-2 emulator.” The purpose of this emulator is to quantify the spatiotemporal sampling bias that is introduced by only constructing temporal averages whenever ICESat-2 passes over a 9-km grid cell of RASM. This is compared to the case where temporal averages for each model grid cell are calculated at every time step of the model. This latter method is the normal method by which climate model output is organized to summarize sea ice state. We use the planned 91-day repeat orbit for ICESat-2, since the satellite is not yet launched.

The ICESat-2 emulator works like this: In one output stream, we sample model output to the nearest hour of an overpass of ICESat-2. The model is only sampled directly under the satellite track. All model grid cells not directly in the vicinity of the satellite overpass in that hour remain unsampled. In this case, a model grid cell’s temporal average is only constructed from the times the satellite passes directly overhead. In a second output stream from the emulator, each model grid cell is sampled at each hourly time step to contribute to that model grid cell’s mean value over a given time period. During the course of a 91-day repeat orbit, or another temporal period of our choosing, when all model grid cells that could possibly receive an overflight of ICESat-2 have done so, we tally up the samples to construct the mean freeboard from both sampling methods and compare the biased mean (satellite sampled) and unbiased mean (each grid cell

sampled at each timestep). This analysis is only conducted within the central Arctic domain annotated in Figure 29, but could be applied elsewhere.

We will symbolize the unbiased temporal freeboard mean as $\langle \overline{fb}_{model} \rangle$. It represents the true temporal mean of the freeboard at each model grid point without spatial bias. The angled brackets indicate an arithmetic temporal mean. The biased temporal mean, constructed by only sampling each model grid point directly under and at the point in time of an ICESAT-2 overpass, is symbolized as $\langle \overline{fb}_{model}^{\rightarrow} \rangle$, where the arrow indicates sampling along the satellite track only. We now discuss exactly how we sample model grid points in the vicinity of an ICESat-2 overpass.

First, this satellite-biased mean is constructed by sampling the model for each of the nearest 9km RASM grid points along the projected ICESat-2 91-day repeat orbit paths across the Arctic, equivalent to 1387 ground tracks per cycle. The bias this introduces is given by:

$$Bias(\overline{fb}_{ICESat-2}) = \langle \overline{fb}_{model} \rangle - \langle \overline{fb}_{model}^{\rightarrow} \rangle$$

The physical meaning of this field is that it indicates the “biased view” of sea ice if we were to only analyze the pack from measurements by the satellite.

Bias was calculated for two different years of RASM output taken from a developmental simulation of the model: 1996 and 2007. The year 2007 was selected because it represents one of the lowest minimum ice extent years in the satellite record (see Figures 1 and 2 in Chapter I). The year 1996 was selected to determine if similar bias was found, in a typical year prior to the rapid retreat of perennial Arctic ice this century. Each year was subdivided into four seasons to study seasonal variation, each period approximately spanning the 91-day repeat orbit of ICESat-2. In order to quantify the contribution of surface snow to the bias, tandem experiments were conducted with and without surface snow, as previously discussed, so that a second bias was calculated for the “no-snow” case:

$$Bias(\overline{fb}_{ICESat-2}(h_s = 0)) = \langle \overline{fb}_{model}(h_s = 0) \rangle - \langle \overline{fb}_{model}^{\rightarrow}(h_s = 0) \rangle$$

Sensitivity of the bias to the precise method of sampling under the satellite track was then investigated. In the bias estimate discussed previously, samples are only taken directly under the projected ICESat-2 flight path. In a second set of tests, this path was expanded out to sample 8 model grid cells directly adjacent to the grid cells sampled at the time of an ICESat-2 overpass. The difference between the two approaches is illustrated in Figures 30 and 31. The first approach we will call “single grid point sampling.” The second method will be referred to as either “expanded grid point sampling” or the “multiple grid point” method. The main purpose of this second set of experiments is to determine if the statistical significance of the bias could be improved (reduced) with a slightly large satellite “swath.” This has implications that will become apparent later in this thesis.

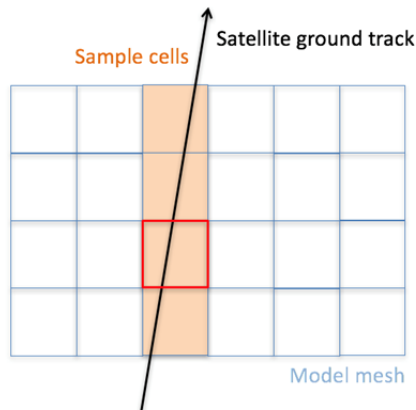


Figure 30. Single grid point method of sampling model freeboard along satellite paths. The temporal mean of the freeboard is calculated for each corresponding RASM grid point directly under the satellite track. The red box indicates the single grid point sampled under the satellite track.

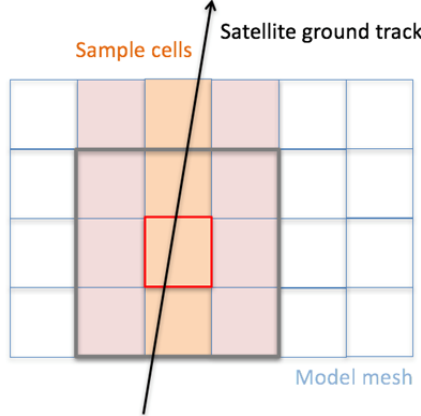


Figure 31. Expanded cross-track sampling. The satellite data collected at one RASM grid point is averaged and expanded to the surrounding 8 grid points. This approach is designed to make better use of the available data by expanding its spatial reach. The gray box details the multiple grid points sampled, expanding from the single (red) grid cell

The statistical significance of the freeboard bias can be estimated using Welch's t-test, necessary because the sample size differs between $\langle \bar{fb}_{model} \rangle$ and $\langle \bar{fb}_{model} \rangle$. From Wilks (2006), the unbiased estimation for standard deviation is:

$$\sigma = \sqrt{\frac{1}{N'-1} \sum_{i=1}^N (X_i - \bar{X})^2},$$

where the effective sample size, N' , is given by

$$N' \equiv N \frac{1 - r_1}{1 + r_1}$$

given the lag-1 autocorrelation r_1 . From this, the effective degrees of freedom, for samples with unequal variances is given by:

$$df = N'_a + N'_b - 2$$

as discussed in von Storch and Zwiers (1999). This may then be used to determine statistical significance at the 95% confidence interval for bias using a two-sided t-test:

$$t = \frac{\bar{X}_a - \bar{X}_b}{\sqrt{\frac{\sigma_a^2}{N'_a} + \frac{\sigma_b^2}{N'_b}}}$$

Where subscript a indicates samples taken for the temporal mean $\langle \bar{fb}_{model} \rangle$, and subscript b indicates samples taken for the temporal mean $\langle \bar{fb}_{\rightarrow} \rangle$ at each 9 km grid point. That is, $\bar{X}_a = \langle \bar{fb}_{model} \rangle$, and $\bar{X}_b = \langle \bar{fb}_{\rightarrow} \rangle$, substituted in the equations to avoid needless complexity. We use the densities of snow, ice and sea water as set in CICE within RASM: $\rho_s = 300$ kg m⁻³, $\rho_i = 917$ kg m⁻³ and $\rho_w = 1026$ kg m⁻³.

An important point to note here is that if we expand the number of grid points sampled surrounding the ICESat-2 track, as in Figure 31, then N'_b increases relative to the case where only a single grid point is sampled under the satellite track (Figure 30). As a result, the effective degrees of freedom increases, refining the t-test. So the ICESat-2 emulator described here represents an idealized test, where we simply sample the model data in two different ways: One way along the satellite track, the other way by sampling all model grid cells with equal weight in time. We are in effect treating the model as “real world” sea ice to understand the significance, or not, of selective spatiotemporal sampling of the pack with LASERs from space. By expanding out the grid points sampled in a second set of tests (increasing N'_b), we learn of the local spatial dependence in the temporal bias. However, as yet, we have not physically justified why it might be acceptable to sample beyond the immediate range of a LASER measurement of freeboard, and we now look to a set of experiments that could justify “multiple grid point sampling.”

D. CHARACTERIZING SPATIAL RELATIONSHIPS IN FREEBOARD

In order to understand how freeboard measurements by LASER are spatially related over scales of 10–100km we will make use of the ICESat and OIB dataset described in Chapter II. The scales 10–100km represent 1 to 10 model grid points, and by

analyzing this scale range, we can determine if there is a close statistical relationship that could justify multiple grid point sampling introduced in the previous section.

Both the ICESat mission and Operation IceBridge (OIB) flight data were analyzed using spectral analysis to determine how measured freeboard varies spatially. The ICESat data set analyzed is “Arctic Sea Ice Freeboard and Thickness, Version 1,” written by Yi and Zwally (2009), and includes measurements from the 14 ICESat LASER campaigns described in Chapter II. Each mission data set was analyzed individually, by season and as individual tracks to determine how the results varied spatially and temporally. Additionally, freeboard measurements from 43 OIB flights were analyzed using the National Snow and Ice Data Center datasets introduced in Chapter II (Kurtz et al., 2015).

Freeboard tracks from ICESat and OIB were spatially detrended, and data gaps were filled by linear interpolation where missing samples did not exceed three times the standard deviation of the approximate sampling distance of 200m and 40m, respectively. Where data gaps exceeded this distance, the distance gap was removed from the tracks as if the track continued in space unimpeded. This procedure is only acceptable due to the relatively continuous nature of the freeboard tracks with few data gaps, and would otherwise be prohibitive due to erroneous spatial signals it introduces. It was found to have minimal impact on the final statistical confidence of the results.

From Priestly (1981), the spectra were calculated using the Fourier transform of the autocovariance weighted by the Parzen Window, C_{yy} , with a maximum lag, τ_{max} , determined by the spatial sampling distance along the tracks, giving the power spectral density function $f(\omega)$. The resulting power spectral density distribution enabled analysis of freeboard along the tracks as a function of wavelength, $\lambda = 1/\omega$, which indicates the spatial scale of interest. A chi-square goodness of fit was then applied to the spectra at the 95% confidence interval to gauge statistical significance of the emergent signal, as described in Emery and Thomson (2014). Dependence of spectra on the particular window chosen was tested by also doing spectral analysis using a Hamming window, but

this did not affect the final conclusions of the investigation, and so results have been omitted from this thesis.

Results presented in Chapter IV reveal strongly linear spectra across large wavenumber ranges. For the purpose of this research, a least-squares linear fit was used to test the strength of the linearity between 400m and 30 kilometers for ICESat and OIB. This scale was chosen because it matched the spatial extent of the multiple grid point sampling of RASM discussed for the ICESat-2 emulator earlier. The linear relationship revealed in the spectra were further interpreted with the aid of Rothrock and Thorndike (1980) and Wadhams and Davis (1994), who used linear relationships in spectra of sea ice draft to characterize spatial noise in their submarine datasets for the Arctic. The gradient of a statistically significant line in spectra on log-log axes, p , reveals a power law relationship between power spectral density, P , and wavenumber:

$$P \propto \frac{1}{\omega^p}$$

Pink noise indicates a weak spatial signal; for this project pink noise occurs when $p=1$. Pink noise is part of the colored noise spectrum which means the power spectrum is correlated with frequency (Sprott 2003), which translates in this case to the mean freeboard being correlated with distance. When $p=0$, this is indicative of white, uncorrelated noise and $p=2$ is Brownian noise. The purpose of conducting this test is to determine if a weak ($p<1$) spatial noise characteristic exists over the scales of interest when comparing LASER derived freeboard with the model. If a weak spatial relation exists, then the method of expanding out the sampled grid cells (Figure 30) can be justified, otherwise we must be content with only sampling grid cell directly under the satellite track.

Table 4. Variable notation used in OIB and ICESat Calculations

Symbol	Description
ω	Wavenumber
λ	wavelength
τ	Spatial lag
p	Gradient of straight line of spectra on log-log axes

E. APPLYING THESE METHODS TO UNDERSTAND SKILL IN MODELS

Using the methods outlined earlier, the final step in this thesis was to derive a way to make an “apples-to-apples” comparison with real LASER freeboard measurements already collected by ICESat. This then serves as an example to follow for when ICESat-2 is launched next year. To do this, we will determine bias in a similar way as discussed at the start of this chapter, only this time, it is not a sampling bias, but a model bias. We assess model bias using the following equation in a similar manner to assessing spatial bias for the ICESat-2 emulator mentioned earlier:

$$Bias(\overline{fb}_{model}) = \langle \overline{fb}_{model} \rangle - \langle \overline{fb}_{obs} \rangle$$

where $\langle \overline{fb}_{model} \rangle$ is the model freeboard sampled along ICESat ground tracks, identical to that described earlier for the ICESat-2 emulator, and $\langle \overline{fb}_{obs} \rangle$ is the mean observed freeboard from Yi and Zwally (2009), averaged for all samples that fall within a single model grid cell for the duration of the model-measurement comparison. The model data is sampled to within ± 1 hour of satellite passing overhead. Therefore, for one pass of the satellite, a mean model grid cell freeboard will be sampled once from the model, but as many as 150 samples of freeboard exist for the satellite track within each model grid cell.

The intention of this thesis is to demonstrate the method, and for this, two years of ICESat data, 2007 and 2004, were used to compare observed freeboard estimates against two different RASM simulations of sea ice thickness. The first simulation used the Anisotropic (EAP) sea ice rheology, the second the isotropic rheology (EVP), for which the spatial thickness and ice drift summaries are shown in Figure 32 and 33. This is then used to gain a measure of the performance of the model’s $g(h_i)$ and $g(h_s)$ simulation using Taylor diagrams (Taylor 2001) and thereafter to estimate skill scores, introduced in the final chapter of this thesis. We next introduce results obtained in applying these methods.

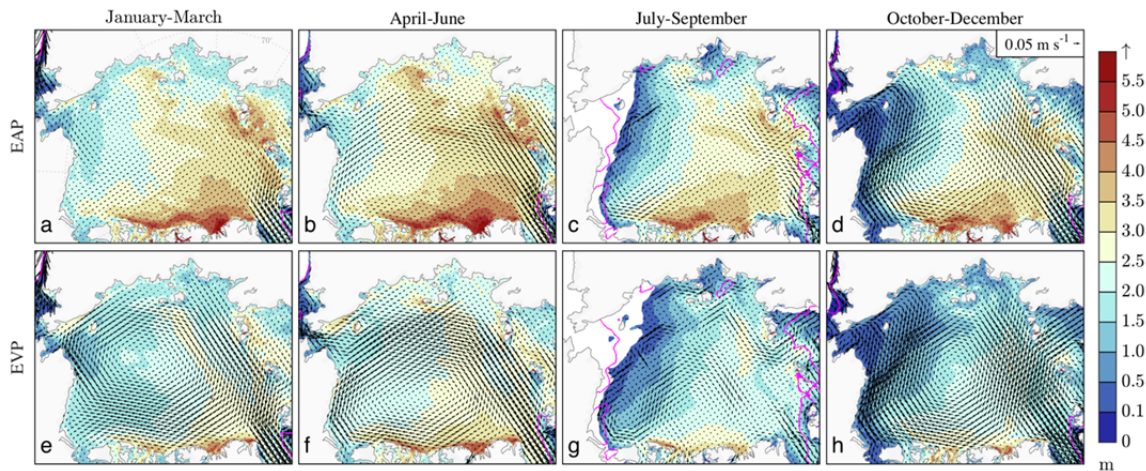


Figure 32. RASM 2004 EAP and EVP mean seasonal thickness \bar{h}_i . The vectors represent sea ice drift. The shading represents the mean sea ice thickness for each grid cell. The magenta line is from the NOAA Climate Data Record of sea ice extent (Meier et al., 2013)

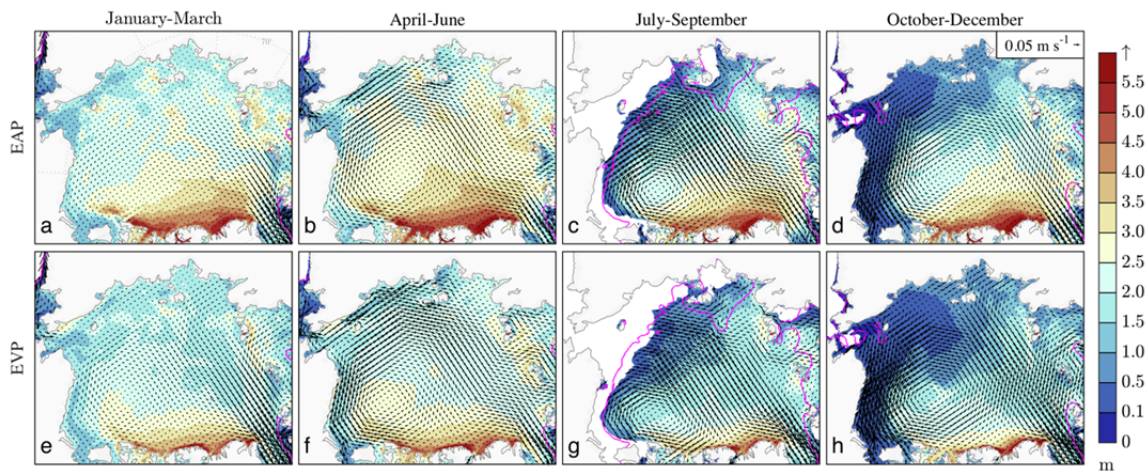


Figure 33. For a more detailed description, see Figure 32. This data is for year 2007.

THIS PAGE INTENTIONALLY LEFT BLANK

IV. BIAS IN OBSERVATIONS AND IN MODELS USING ALTIMETRICALLY DERIVED SEA ICE FREEBOARD

A. OVERVIEW

Using the methods introduced in the previous chapter, results are now presented in the order in which the methods were discussed. First, model results from the ICESat-2 emulator are examined to determine the freeboard bias when sampling only along satellite tracks to construct temporal means. Then, spectral analysis was applied to both ICESat and OIB freeboard estimates, to determine the spatial noise characteristics of the mean freeboard signals. Finally, using the results from the spectral analysis, model bias is calculated using ICESat freeboard samples. The results demonstrate how satellite freeboard measurements may be used to evaluate RASM, and, more broadly, numerical models of sea ice.

B. ICESAT-2 TEST EMULATOR

The ICESat-2 emulator was used to calculate freeboard temporal averages along its orbital tracks using developmental RASM model runs from 1996 and 2007, analogous to the model simulations discussed in Chapter III. The only role the model simulations have at this point is to provide a stable representation of the pack that enables us to estimate the ICESat-2 *Bias*($\overline{fb}_{ICESat-2}$) at each model grid point within the central Arctic domain (black outline, Figure 29). This is representative, also, of the ICESat sampling bias relevant later in this chapter.

The *Bias*($\overline{fb}_{ICESat-2}$) results are segmented into 4 seasons, using the projected 91-day repeat orbit cycle and presented in Figures 34 to 37. Figures 34a and 35a illustrate the difference between the track-sampled and regular freeboard means for both 2007 spring and fall seasons. Each season corresponds to one complete 91-day repeat orbit period. Here, the spring season is defined as April to June and the fall season is October to December. The largest mean freeboard biases, greater than 0.09 m, are in the Arctic Ocean regions furthest from the North Pole. This corresponds to the areas of minimal or no sampling conducted by the satellite where orbital paths diverge with increasing

distance from the pole. Additionally, during the fall, this is a region of large sea ice drift velocities (Figure 32 and Figure 33), associated with the Beaufort Gyre, which may be influencing for the positive bias. It is also a region of greatest thermodynamic growth and melt, and is thus sensitive to sampling frequency.

Using the calculated differences of the freeboard means, Welch's two-sided t-test was applied to determine the statistical significance of the model bias at each grid point, as described in Chapter III. The results are provided in Figures 34(b) and 35(b) alongside the bias values. Red shading in these Figures indicates a difference significant at the 95% confidence interval. The most important results illustrated in Figures 34 and 35 is that although the sampling bias, $Bias(\overline{fb}_{ICESat-2})$, is greatest furthest from the pole, the result is statistically insignificant over a single repeat orbit period of 91 days, because that part of the pack is seldom sampled. By contrast, the largest statistical significance is closest to the pole, where the bias between evenly sample freeboard, and satellite-sample freeboard is smallest. These results are representative of the 1996 case also tested, not shown here, but included in Appendix 1 due to the strong similarity in the bias and statistical significance pattern. This similarity between 1996 and 2007 indicates the problem is not climatologically driven, but instead a sampling problem mostly independent of the state of the pack. Similarly, results from the 2007 winter and summer seasons show less bias and are provided in Appendix 1. These seasons are outside the periods of significant freezeup or melting cycles, accounting for the reduced bias.

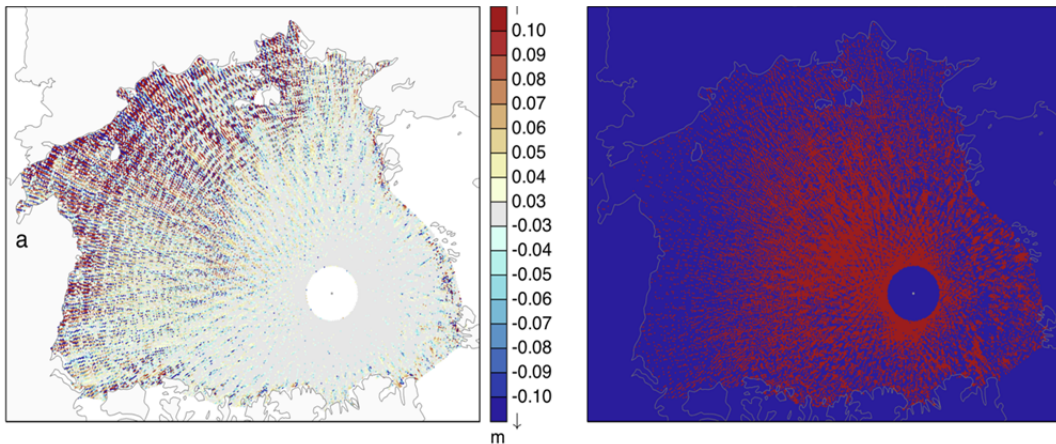


Figure 34. a) 2007 $Bias(\bar{fb}_{ICESat-2})$ for freeboard sampled along ICESat-2 tracks for one complete 91-day repeat orbit period over the spring for April to June using the ICESat-2 emulator and RASM described in Chapter 3. b) Biases in (a) that are statistically significant at the 95% confidence interval (red). In this case, only model grid cells were sampled directly under each satellite track within ± 1 hour of the satellite pass as shown in Figure 30.

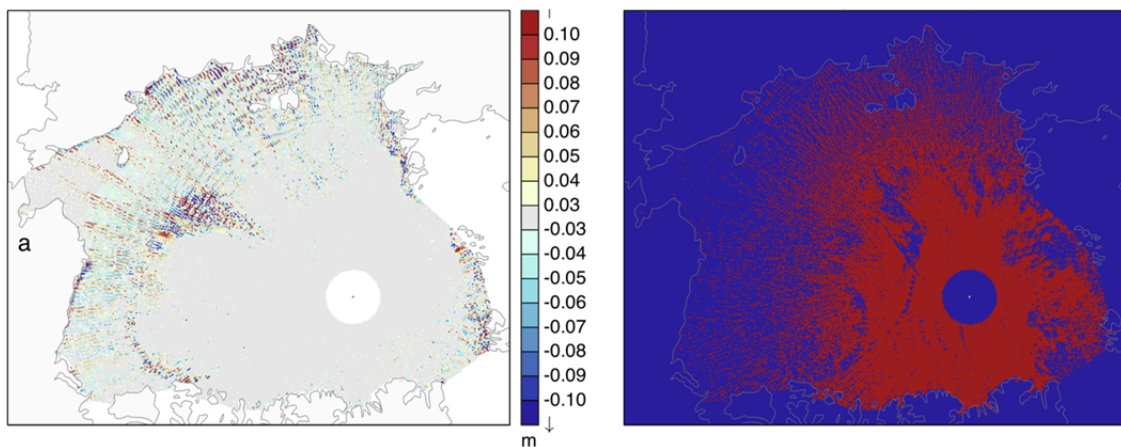


Figure 35. For a more detailed description, see Figure 34. This data is for fall months October to December 2007 over one complete 91-day repeat orbital period.

In order to understand the impact of expanding the number of grid cells sampled under each satellite track, multiple grid cell sampling, as demonstrated in Figure 31, was

applied to the ICESat-2 emulator for the same model data presented in earlier. In practical terms, the sampling was adjusted to sample freeboard for a grid cell underneath an ICESat-2 track, as well as the surrounding 8 RASM grid points. This expands the “reach” of the track-sampled data from an approximate 9 km grid cell to approximately 27x27 km grid box. Results for this test are provided in Figures 36 and 37, which are analogous to Figure 34 and 35, respectively.

The cell expansion method reduces the biases between the satellite and model freeboards across much of the Arctic region. By expanding the sampled area to include a total of 9 grid cells (middle grid cell plus 8 surrounding grid cells), the statistical significance of the bias is greatly expanded, and includes most of the Arctic basin. At same time, the sampling bias is greatly reduced. These results are consistent with both winter (January-March) and summer (July-September) cases, which are not shown for brevity.

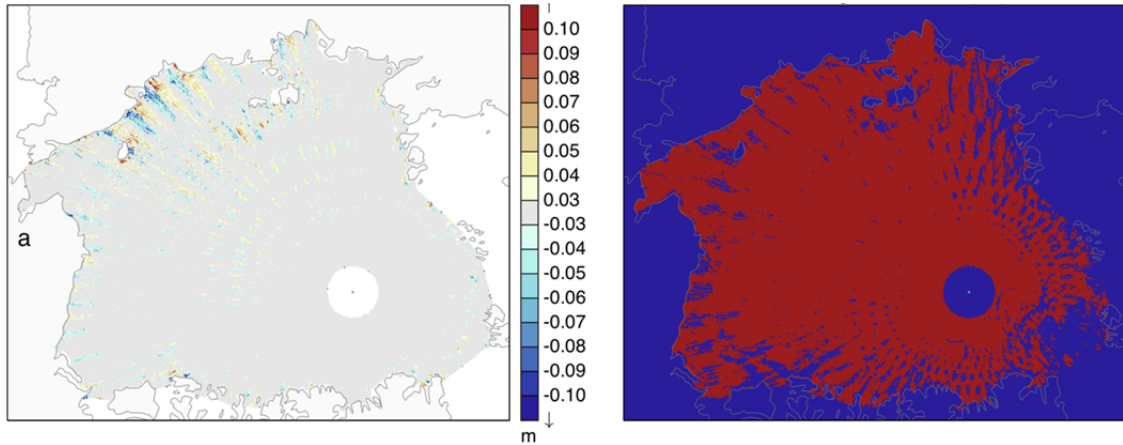


Figure 36. a) 2007 $Bias(\overline{fb}_{ICESat-2})$ for freeboard sampled along ICESat-2 tracks for one complete 91-day repeat orbit period over the spring for April to June using the ICESat-2 emulator and RASM described in Chapter III using multiple grid-point sampling. b) Biases in (a) that are statistically significant at the 95% confidence interval (red).

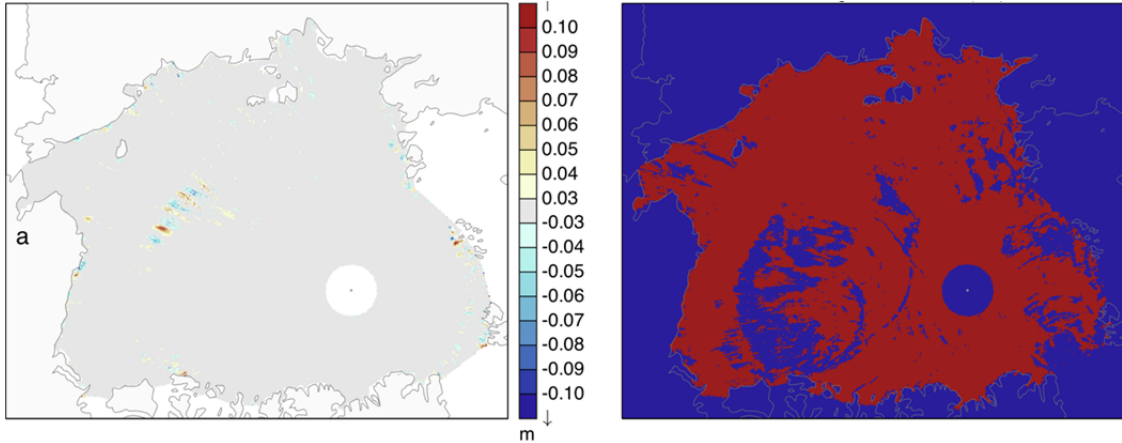


Figure 37. For a more detailed description, see Figure 36. This data is for fall months October to December over one complete 91-day repeat orbital period. The broad, circular feature depicted in Figure b may represent an inconsistency within the model and how RASM is handling the ice edge during this season.

Developing this ICESat-2 emulator using RASM output as “real” sea ice thickness data provided valuable insight into how to maximize the use of the altimetric data within the model. First, from using the 91-day repeat orbit, we were able to acquire a biased seasonal signal, allowing us to quantify satellite bias implicit in model-observation comparisons. By expanding the grid point sampling from 1 to 9 grid cells, the spatial coverage and the statistical significance of the bias is increased drastically for the Arctic Basin, and the overall bias is reduced. This is important due to the limited spatial resolution of the ATLAS measurements that will be taken when ICESat-2 is launched next year. But it is equally relevant to comparing models with ICESat data that has already been collected, because that satellite used a similar 91-day repeat orbit for much of its mission.

The ICESat-2 emulator was also used to analyze differing snow regimes in a second series of tests. To do this, the freeboard bias was calculated by removing snow from the calculation, as shown in Chapter III for $Bias(\bar{fb}_{ICESat-2}(h_s = 0))$, again for all months in 1996 and 2007. This calculation is only possible because we are using model data for which we explicitly know the snow cover distribution, as detailed in Equation 5 in Chapter III. However, there was little sensitivity to the change in terms of the spatial

pattern in bias magnitude and statistical significance as compared to the results presented earlier. Therefore, we may conclude that, if possible, expanding the sampling of model output beyond a strict ground track of a LASER altimeter will lead to a more accurate estimate of model bias.

The ICESat-2 cases presented here assumes an ideal environment, providing perfect coverage along each track throughout both the tested years. In this case, we tested our results sampling for each 9km grid cell on the ground track, and also expanded the sampled area to $\sim 27 \times 27$ kilometers. The next step in this project is to use the spectral analysis described in Chapter III to determine whether or not expanding the satellite track is physically justifiable.

1. ICESAT AND OIB SPECTRAL ANALYSIS

Spectral analysis was used to characterize spatial noise relationships of the ICESat and OIB freeboard data introduced in Chapter II. The power spectral density was characterized with the p -exponent described in Chapter III, using the R^2 statistic (von Storch and Zwiers 1999) as an indication of the goodness of fit of the noise characterization. The p -exponent and correlation coefficient, R^2 , were calculated for the 14 ICESat campaigns discussed in Chapter II using ensemble freeboard means with varying temporal scales. This approach allowed determination of differing p -exponents and goodness of fit between observational campaigns, presented as an ensemble mean of individual ground tracks. Statistical significance of the spectra were estimated at the 99% confidence interval, an power spectral density is presented on a relative scale of decibels (dB), converted to $10 \log_{10} P$ for power P (that is, referenced to 1 m^{-2} of freeboard power).

a. ICESat

For ICESat, the analysis of freeboard was conducted using three temporal scales: a) ensemble series for winter, summer and fall campaigns (Figure 38, Figure 39, and Figure 40); b) individual campaigns (Table 5); and c) single, cross-basin tracks were processed (Table 5). The ensemble series comprised of all fourteen data sets, which

includes approximately 35 days of data for each campaign. Six campaigns are included in both the winter and fall series and the summer series includes two campaigns. The cumulative winter series, Figure 38, resulted in a p exponent of 0.49 with an excellent goodness of fit ($R^2=0.98$). This result indicates that for the spatial scales between 400m and 30km, the freeboard has a signal ‘half way’ between white and pink noise. In other words, it varies only weakly with distance in this range of spatial scales. Similar p -exponent results were detected for all the summer and fall series (Figure 39 and Figure 40). These results suggest that the RASM model sampling can be expanded roughly to a 3x3 grid cells (27x27 km) on a monthly time frame to improve the robustness of model evaluation using ICESat. The results presented so far are for an ensemble average of all ICESat orbits, and the solidity of the result was frayed when looking at individual tracks: R^2 values decreased significantly for the single, cross-basin tracks (Table 5) mainly due to smaller sample sizes.

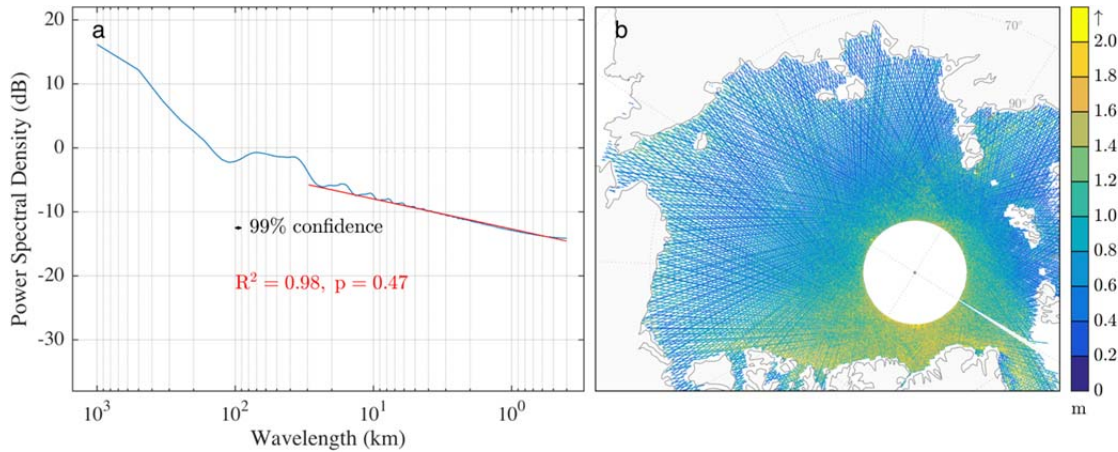


Figure 38. a) Winter ICESat freeboard series 2003 to 2008: Ensemble mean of Power Spectral Density in dB. with the p exponent estimated from the line in red, and associated R^2 fit between 400 meters to 30 kilometers. b) The individual ICESat tracks used to calculate the ensemble average. Winter flights are annotated by the blue cells in Table 1 in Chapter II. The color bar represents freeboard in meters.

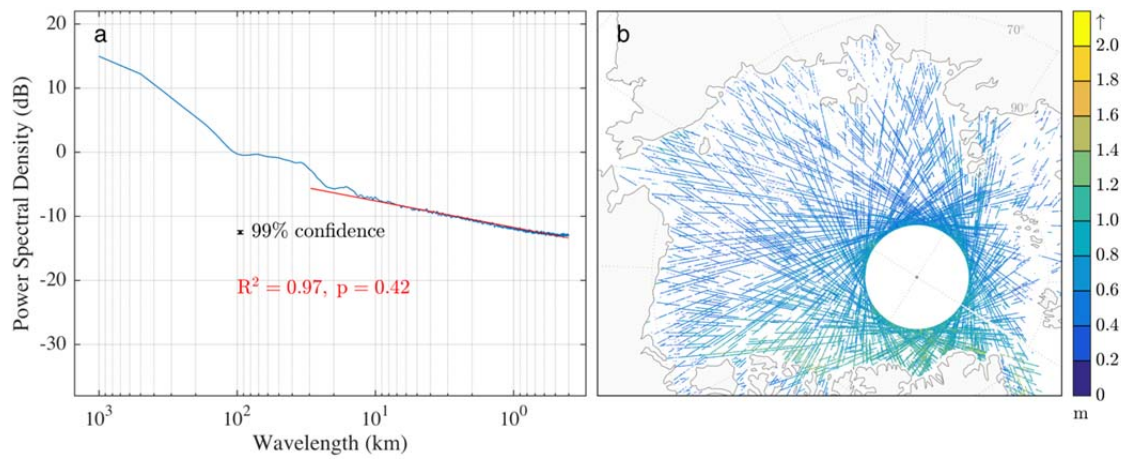


Figure 39. For a more detailed description, see Figure 38. This data is for summer 2004 and 2006, corresponding to the green cells in Table 1 in Chapter II.

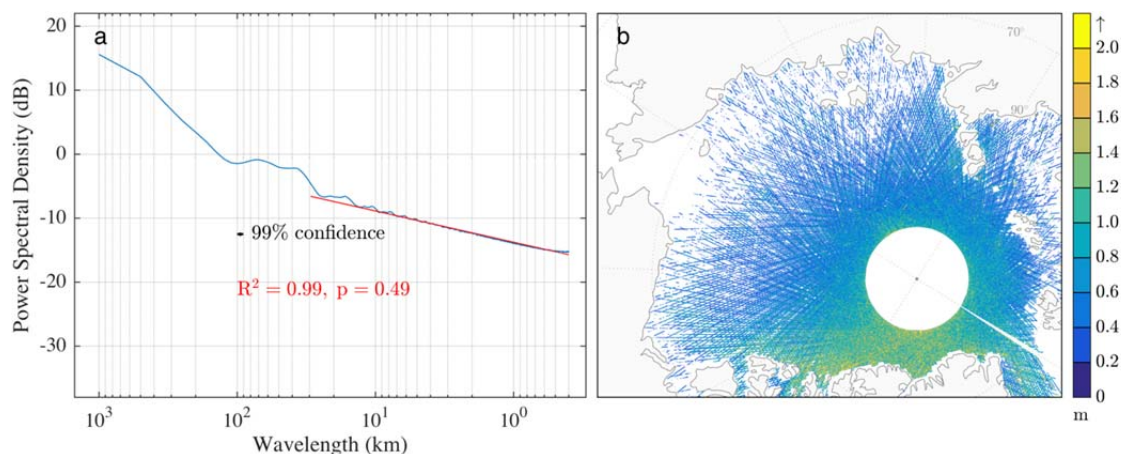


Figure 40. For a more detailed description, see Figure 38. This data is for fall, 2003 to 2008, corresponding to the orange cells in Table 1 in Chapter II.

Table 5. Summary of ICESat spatial freeboard noise characteristics, and R^2 values.

Campaign	Season and Year	p exponent	R^2
Winter	Cumulative	0.47	0.98
Summer	Cumulative	0.42	0.97
Fall	Cumulative	0.49	0.99
2B	Winter 2004	0.54	0.99
3H	Winter 2007	0.44	0.98
3A	Fall 2004	0.40	0.98
3I	Fall 2007	0.51	0.96
Single Track 3H0217002	Spring 2007	0.43	0.58
Single Track 3B0197002	Winter 2005	0.29	0.35
Single Track 3A0270002	Fall 2004	0.35	0.40
Single Track 3D0392002	Fall 2005	0.44	0.50

Beyond the spatial scale range from 400m to 30km, there is a transition zone seen in the ICESat signal in the range between 30 and 100 kilometers. This may represent a region in the spectra where the GLAS measurements shift from effectively being an aerial average of freeboard, through the solid angle of the incident LASER beam on sea ice and snow, to representing more of a grid point sample on the scales of 100km or greater. As already stated, the spatial scales associated with the transition region are not in wavelengths of interest for this study, and so we dispose of the further analysis of this transition zone. However, it is an important limitation of the data that may not be widely understood or appreciated by the research community.

b. OIB

Forty-three flights between 2009 and 2015 were analyzed using the same method as for the ICESat data to characterize spatial noise. Figure 41 shows the analysis for the ensemble mean spectra for all OIB Arctic flights in the indicated year range. Here, focusing on the data between 400 meters and 100 kilometers, the p exponent is 0.74, again indicative of noise between white and pink characterizations. The confidence in this estimate is high with an R^2 value of 0.99. Below the ATM resolution of 250 meters, the p -exponent values increase beyond the pink and even the brown noise regime. While this result is not relevant to the scales of interest here, we hypothesize whether it may indicate a limitation of the Quicklook freeboard product for small scales. Rothrock and Thorndike (1980) detected an analogous drop-off in their spectral power of draft with decreasing spatial scales, which they attributed to the expanse of their sonar swath looking up at sea ice. By contrast here, the drop-off may be attributable to processing of the spiral ATM data indicated in Figure 22 in Chapter II.

Each individual flight was analyzed in the same manner as in Figure 42 and Figure 43. While the p exponents were larger than for ICESat, the noise is still weakly varying with space over the scale of interest, further justifying a slight expansion of model grid points used to evaluate RASM. Table 6 provides values for one single, cross basin flight for each year. The p exponent values are all indicative of the spectrum between white and pink noise, which further supports expanding the model sampling spatial scale to 27x27 km grid cells.

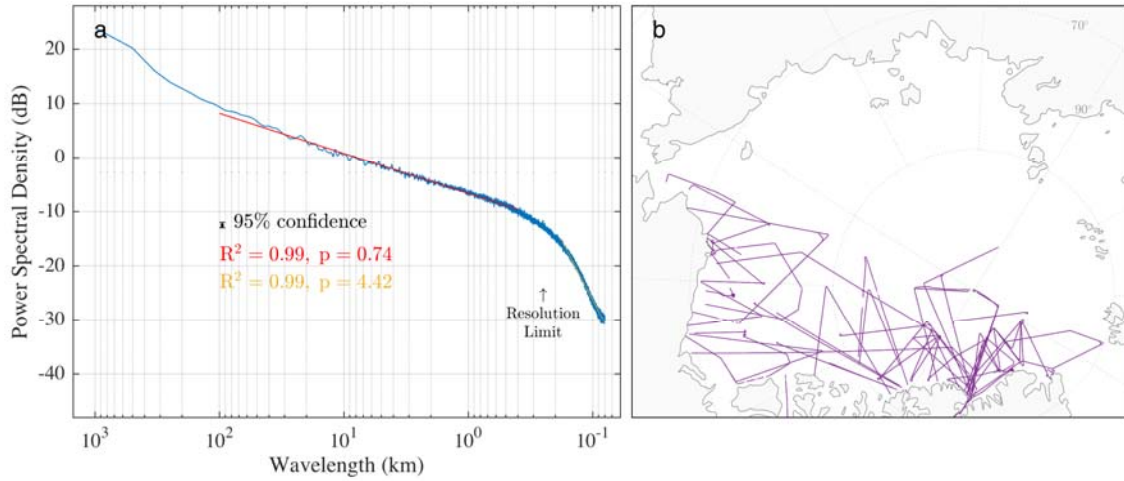


Figure 41. a.) OIB spring series for 2009 to 2015: Ensemble mean of power spectral density in dB. with the p exponent estimated from the line in red, and associated R^2 fit between 400 meters to 100 kilometers. b) The individual OIB tracks used to calculate the ensemble average.

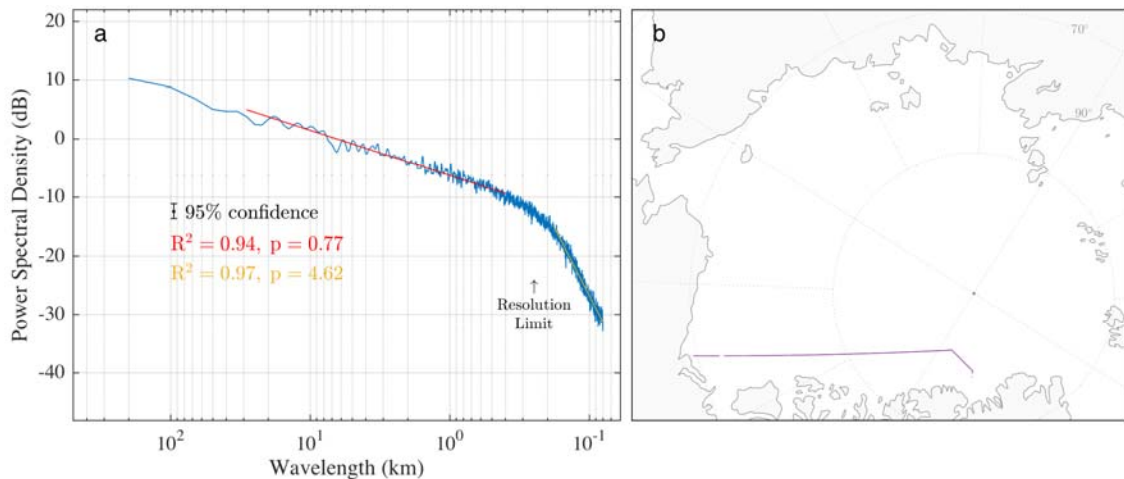


Figure 42. Individual OIB Flight conducted on 02 April 2009: Power Spectral Density in dB. with the p exponent estimated from the line in red, and associated R^2 fit between 400 meters to 100 kilometers. b) The individual OIB track used to calculate PSD.

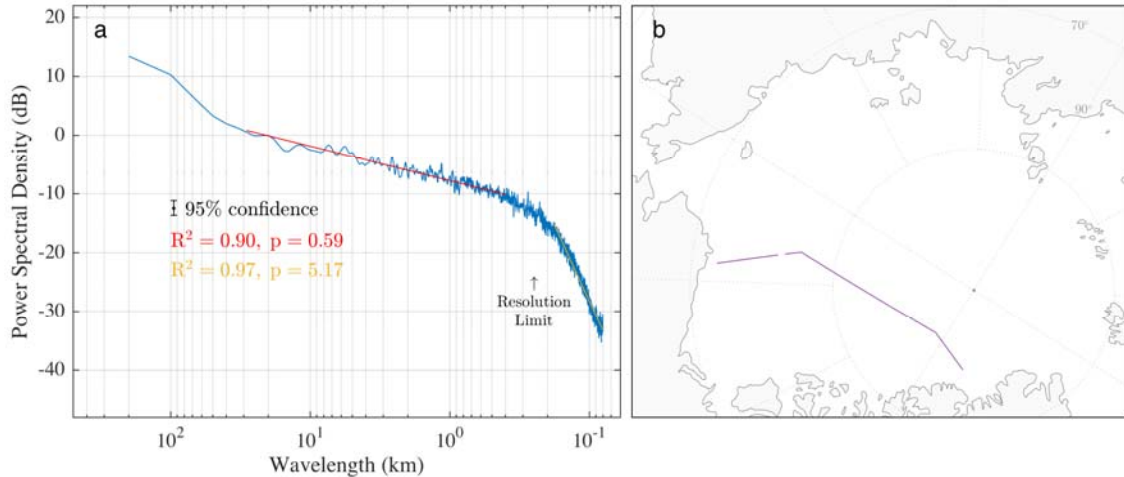


Figure 43. For a more detailed description, see Figure 42. This data is for an OIB Flight conducted on March 14, 2014.

Table 6. OIB Spectral Analysis Values

Flight	p	R^2
Ensemble average	0.74	0.99
IDC20090402	0.77	0.94
IDC20100419	0.67	0.90
IDC20110326	0.63	0.92
IDC20120324	0.54	0.80
IDC 20130321	0.72	0.90
OIB_20140314	0.59	0.90
OIB_20150324	0.83	0.87

2. Discussion

Both ICESat and OIB spectral analysis results support the objective to expand altimetric measurements to three RASM grid cells for monthly and seasonal estimates of bias. Only weak spatial correlation is evident from the gradient of both the OIB and ICESat flight path power spectrums. Sub-pink noise is consistent between spatial resolutions of 400 meters to 30 kilometers. For the ICESat campaigns, the p exponent results were similar, varying between 0.29 and 0.61 for all tracks. The R^2 for each campaign ensemble and cumulative seasonal ensemble is consistently between 0.96 and

0.99. We note that the transition zone between 30km and 100km detected in ICESat does not exist in OIB data, and is probably attributable instrument bias in ICESat data. However, for the scales of interest, the results support using the multiple grid cell sampling method described in Chapter III. We now apply this to the design of a sampling method to estimate the skill of RASM simulations for two selected years in the ICESat record.

C. INITIAL ICESAT EMULATOR RESULTS

The ICESat-2 bias estimates provided at the start of this chapter quantify the spatial bias in sampling a model as if a satellite were flying across model grid cells. Here, we use collected ICESat data to evaluate the actual model bias along satellite tracks as compared to measurements of freeboard. In other words, we opened this chapter seeking to determine how to best evaluate $Bias(\overline{fb}_{ICESat-2}) = \langle \overline{fb}_{model} \rangle - \langle \overline{fb}_{\vec{model}} \rangle$, and we close this chapter by using the experience gained in that exercise to evaluate $Bias(\overline{fb}_{\vec{model}}) = \langle \overline{fb}_{\vec{model}} \rangle - \langle \overline{fb}_{\vec{obs}} \rangle$. This is done for the ICESat campaign years of 2004 and 2007, selected because the first year (2004) represents a period at the onset of the rapid decline of perennial sea ice this century, and the second year (2007) represents one of the lowest summer sea ice extents in the Passive Microwave record, as discussed Chapter II. We analyze the two different model simulations discussed in Chapter III (Figure 32 and Figure 33) that utilize EAP and EVP sea ice rheology. In this section, we will be using sea ice freeboard measurements which includes snow loading. However, ICESat assumes measures just one value for all freeboard measurements. A complication, not experienced with the ICESat-2 ideal test case results, is the ICESat campaign's mechanical failures and erratic environmental impacts along the satellite tracks. These resulted in breaks in satellite coverage and causing data paucity along some tracks, but are easily handled by the chosen statistical tools.

a. Single versus Multiple Grid Points ICESat Emulator 2007: Freeboard calculations plus snow

Here we investigate again the impact of sampling only a single line of model grid cells underneath a LASER track, as compared to including adjacent grid cells in the analysis. In this case we use real measurements for freeboard taken by GLAS aboard ICESat. In Figure 44, results from the ICESat emulator results are displayed for 2007 spring and fall periods of March 12-April 14, and October 2-November 5, respectively. For clarity, we refer to the March 12-April 14 campaign as “spring” in the following Figures and analysis. This specific campaign includes both “spring” and “fall” dates as we have defined in section B, unlike the other ICESat campaigns analyzed. This is consistent with previous literature on the ICESat dataset.

For the model freeboard calculations including snow loading, Figure 44 (a) and (b), depicts the calculated freeboard $\langle \overrightarrow{fb}_{obs} \rangle$ for ICESat. The spring 2007 campaign had significantly more ground track coverage as compared to the fall season. This is important to recognize, as we step through the process and prove the satellite emulator works with varied spatial coverage from the satellite observations. Of note, an anomaly was identified within the ICESat $\langle \overrightarrow{fb}_{obs} \rangle$ Figures, which depict large freeboard values around the Greenwich meridian. This is an issue with the ICESat freeboard data issued by NASA, rather than the methods used here.

The largest freeboard values for both seasons are to the north of the Canadian Archipelago and Greenland coastlines, which aligns with the spatial thickness pattern seen in RASM (Figure 32). However, there are discrepancies evident in freeboard between the observations and the model. For both the EAP and EVP RASM simulations, the largest freeboard biases occur near the center of the Arctic Ocean and in the Nansen Basin during the spring season. The EAP model depicts larger, wide-spread biases in these regions. In fall, the modeled sea ice freeboard bias is more subtle, with the EVP model run depicting less discrepancy. This is possibly due to how each model characterizes the WRF snow values and biases associated with the snow input.

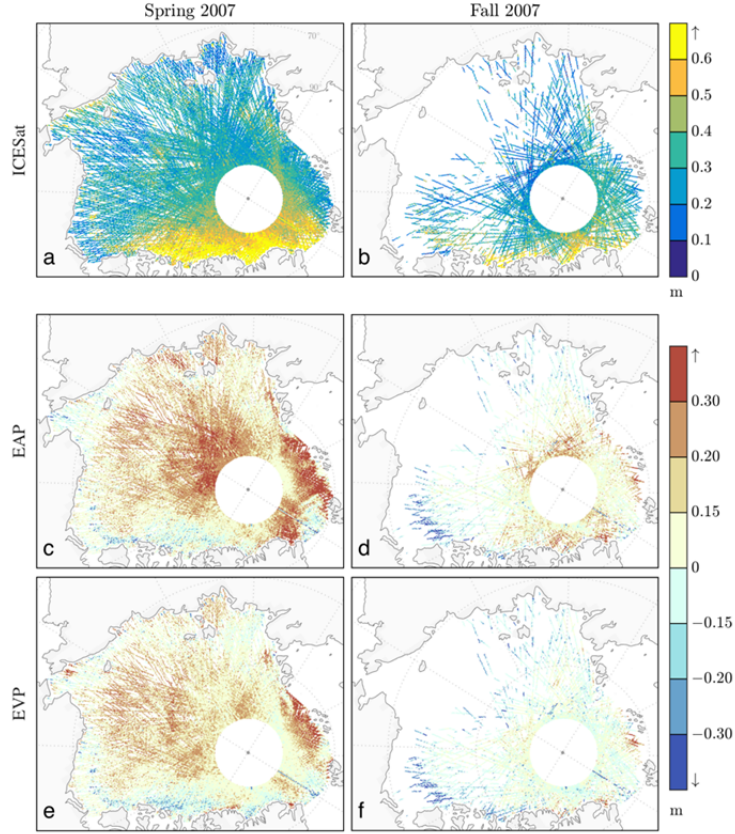


Figure 44. $\langle \overrightarrow{fb}_{obs} \rangle$ for ICESat, calculated for single grid-point sampling in a) spring and b) fall 2007. The model bias for these seasons, $Bias(\overrightarrow{fb}_{model})$ is provided in c) and d), respectively, for the RASM simulation using EAP sea ice mechanics, and e) and f) for the EVP sea ice mechanics variant.

Applying a t-test to these results, Figure 45, indicates that only a slender margin of $Bias(\overrightarrow{fb}_{model})$ is significant at the 95% confidence interval around the “pole hole.” This corresponds to the region with the largest sample sizes for each 9km model grid cell, as indicated in, Figure 46.

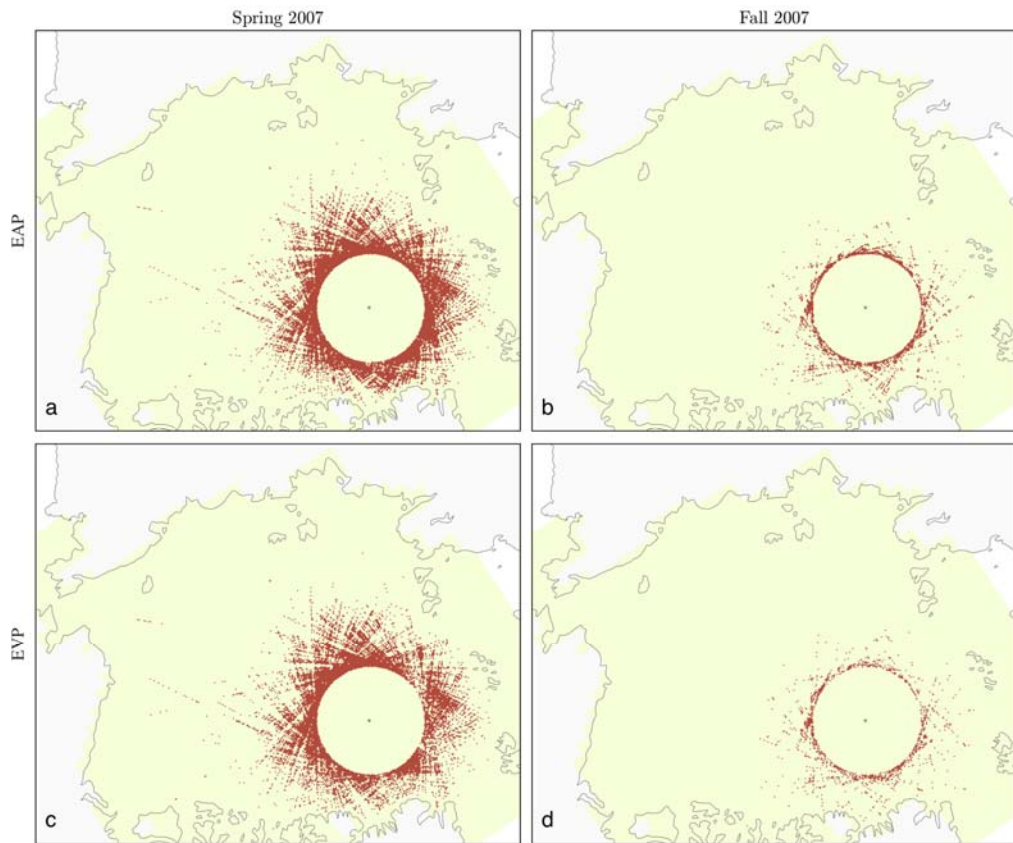


Figure 45. ICESat Emulator 2007 Welch's T-test using Single Grid Point. Panels a-d correspond to Figure 44 c-f. $Bias(\overrightarrow{fb}_{model})$ that is statistically significant at the 95% confidence interval is represented in red.

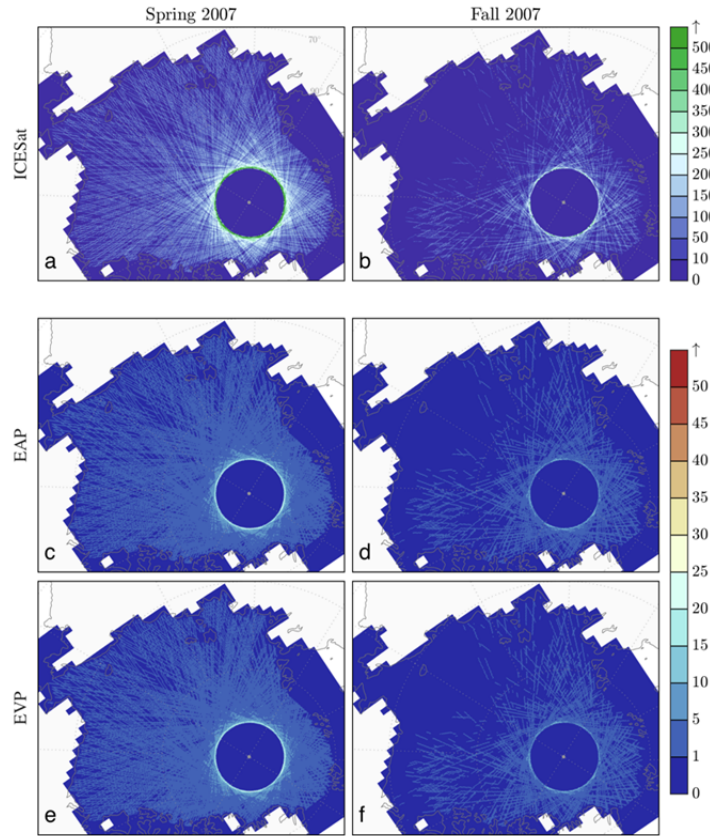


Figure 46. ICESat Emulator 2007 sample size using single grid point sampling.

Color bars represent the number of samples for the satellite and models corresponding to results in Figures 44 and 45.

As expected, a similar distribution of freeboard differences is evident in the multiple grid cell results presented in Figure 47. By expanding to the neighboring grid points, spatial coverage of the model bias estimate is enhanced for both seasons. The disparities between modeled and observed freeboard are more evident, as they are covering more grid cells. The most significant difference between the ICESat single and multiple grid point sampling are the t-test results (Figure 48). The statistical significance for the spring season provides nearly basin wide statistical significance for the model bias. The fall season statistical significance also provides increased coverage away from the Arctic hole, but is more limited by a scarcity of available tracks. The model bias is statistically significant to 95% for a much larger portion of the Arctic due to the increased

sample size (Figure 49). The results are similar to those seen earlier in this chapter for the ICESat-2 emulator.

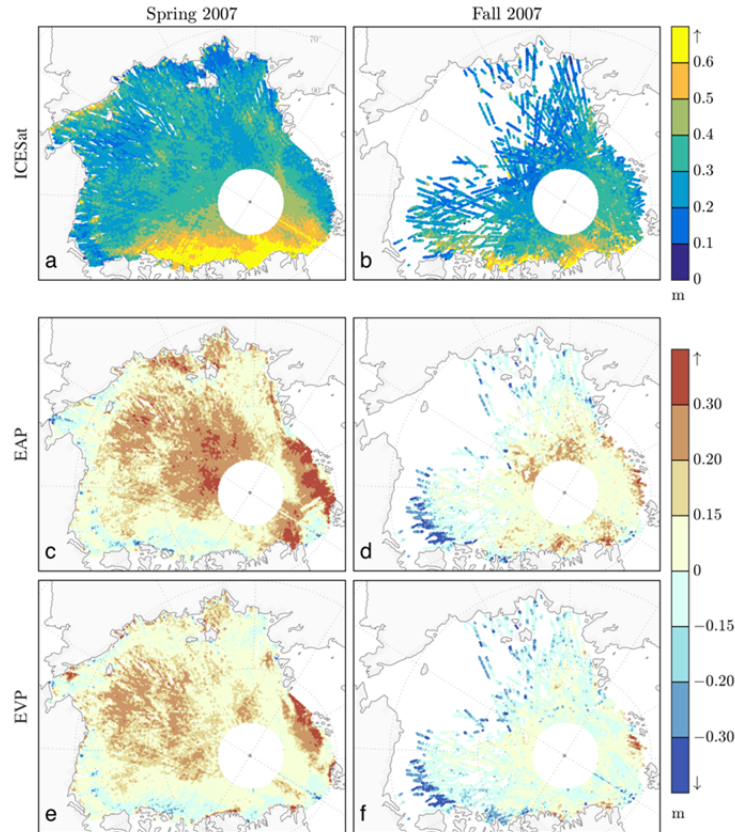


Figure 47. $\langle \overrightarrow{fb}_{obs} \rangle$ for ICESat, calculated for multiple grid-point sampling in a) spring and b) fall 2007. The model bias for these seasons, $Bias(\overrightarrow{fb}_{model})$ is provided in c) and d), respectively, for the RASM simulation using EAP sea ice mechanics, and e) and f) for the EVP sea ice mechanics variant.

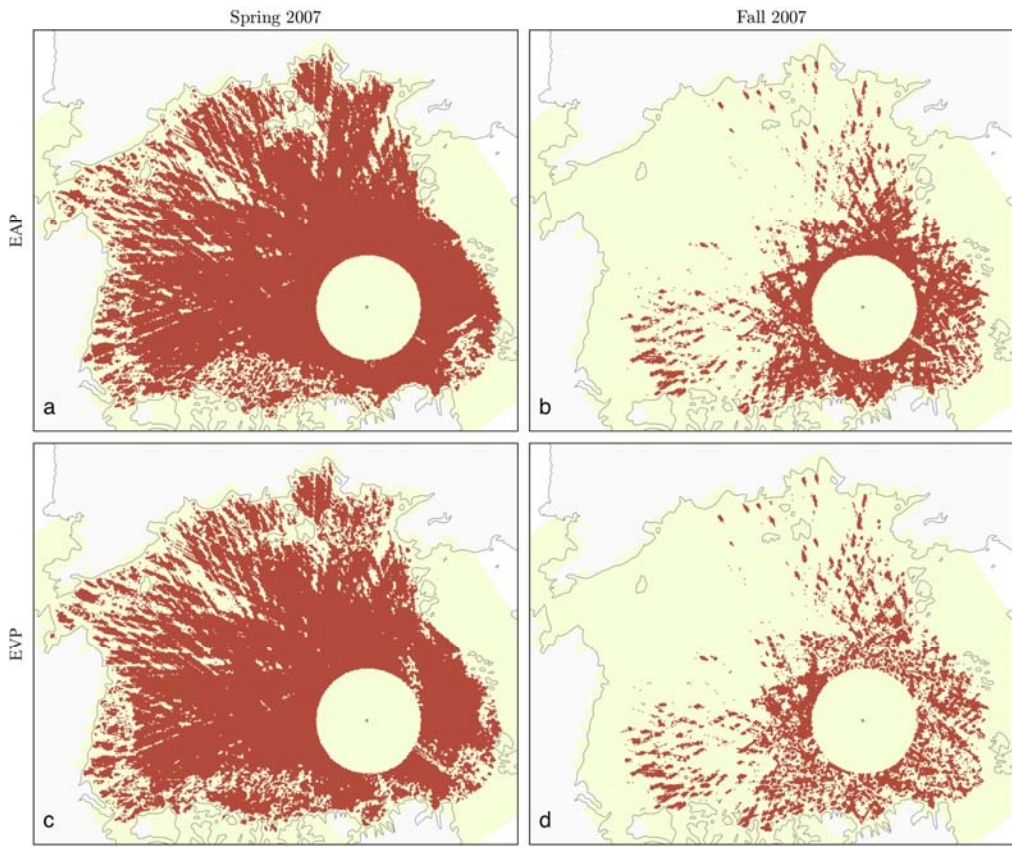


Figure 48. ICESat Emulator 2007 Welch's T-test using Multiple Grid Points.

Panels a-d correspond to Figure 47 c-f. $Bias(\bar{fb}_{model})$ that is statistically significant at the 95% confidence interval is represented in red.

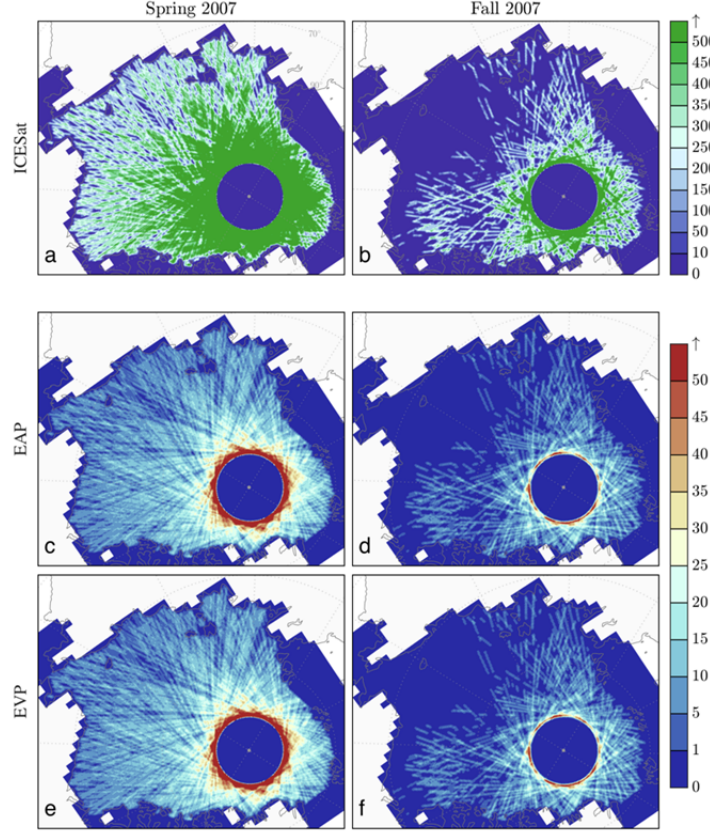


Figure 49. ICESat Emulator 2007 Sample Size using Single Grid Point sampling. Color bars represent the number of samples for the satellite and models corresponding to results in Figures 44 and 45.

These results from the ICESat emulator comparing single and multiple grid point sample were similar to the ICESat-2 emulator results discussed at the beginning of this chapter. The expanded grid cell technique provides enhanced spatial coverage of the Arctic Ocean, supported by statistical significance with a 95% confidence interval.

The RASM sea ice thickness distribution for both EVP and EAP sea ice models (Figure 50), depicts similar results for both the single point and multiple grid point sampling, supporting the multiple grid expansion method. For both 2007 model results, the model thickness distribution is skewed to the right of the ICESat data, which may be due to the record minimum sea ice observed during this time period not being correctly captured by the model, except the EVP case in fall 2007. More importantly for our results, both the single grid and multiple grid techniques are well aligned with one

another. The ice thickness distribution does not vary substantially between the two methods, supporting the expansion technique.

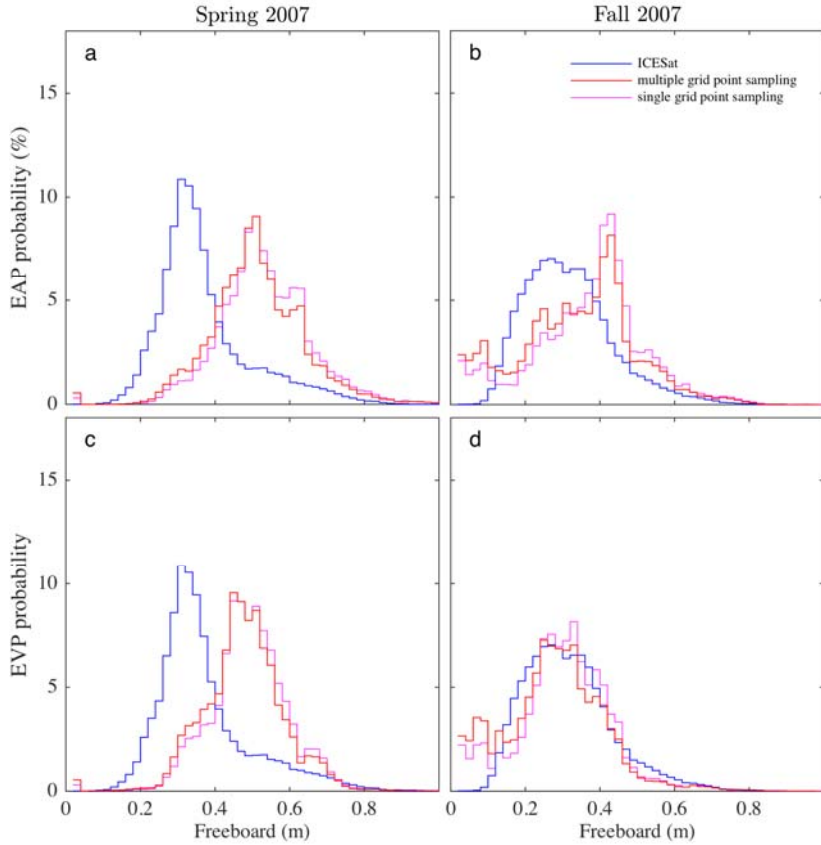


Figure 50. ICESat 2007 thickness distribution. Probability density function of freeboard, analogous to thickness distribution PDF displayed from Hutchings et al. (2008). Blue represents ICESat observations, Red represents multiple grid point sampling technique and magenta represents single grid point sampling.

A Taylor diagram summarizes the ICESat emulator analysis for the pattern means presented in Figures 51(a) and 51(b), which explains statistical relationships between the basin-wide model and measured freeboard patterns across the Arctic Basin. The Taylor Diagram provides a concise statistical summary of how well the multiple and single grid point techniques are similar in terms of correlation, variance and root-mean-square differences (RMSD) (Taylor 2001). To plot the statistical differences between the models

and observations, the model variables are normalized relative to the standard deviation of the observations (Taylor 2001).

For the spring 2007 season, the multiple-grid-point sampling correlation is 0.6. The multiple-grid-point sampling almost perfectly replicates observed freeboard variance across the Arctic basin, with a Standard Deviation of ~1, normalized against the pattern standard deviation. The single grid point sampling technique has a slightly smaller variance than the observations. For the fall season, both of the model runs decrease correlation and increase variance, opposite to the equivalent observational shift. The significant difference between the seasons may be due to a smaller sample size for the fall of 2007, but, when viewed in context of earlier results, it is more likely an indication of the inability of the model to replicate extreme seasonal sea ice decline that occurred in 2007.

Applying the multiple grid point sampling technique to both individual ICESat LASER campaigns and to a series of campaigns, we are able to obtain statistical significance for approximately one third of a 91-day repeat orbit, which corresponds to an individual seasonal campaign of approximately 35 days (Table 1). This allows the analysis technique to be used to evaluate all climate models, in addition to monthly sea ice forecasts, making this methodology a universal tool applicable to both short and long term navy forecasts.

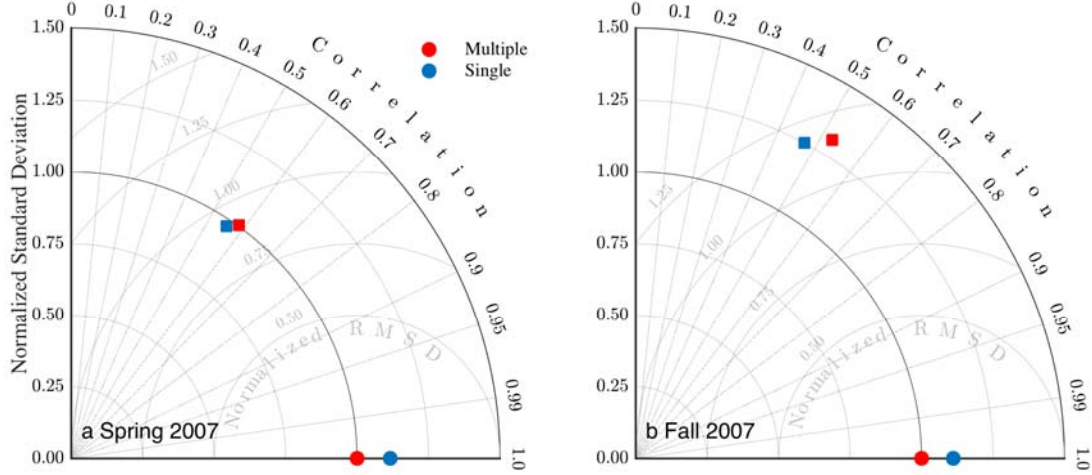


Figure 51. ICESat Emulator 2007 Taylor Diagram. The red and blue circles represent observations, and the squares are the model representations of both the single grid point and multiple grid point technique.

D. FINAL ICESAT/ICESAT-2 EMULATOR DESIGN—EXAMPLES FROM 2004 AND 2007

Having settled on the 9-grid-point sampling method, we now view the full complement of results for 2004 and 2007 for the aforementioned EVP and EAP model runs (Figure 32 and Figure 33). Here, two freeboard biases were assessed, the model freeboard with snow loading, $Bias(\overline{fb}_{model})$, and the model freeboard without snow loading, $Bias(\overline{fb}_{model}(\overline{h}_s = 0))$, thus generating a second set of freeboard bias estimates:

$$Bias(\overline{fb}_{model}(\overline{h}_s = 0)) = \langle \overline{fb}_{model}(\overline{h}_s = 0) \rangle - \langle \overline{fb}_{obs} \rangle$$

Importantly, at no time were the observed freeboards from ICESat adjusted for the presence of snow, because this requires assumptions about snow density and thickness for which we have only limited knowledge in the observed dataset. In contrast, we have a complete understanding of the snow thickness and density in the sea ice model. Thus, by adjusting the model, rather than the satellite data for the presence of snow, we circumvent a long-standing issue in that satellites have no knowledge of the density of snow and ice along the ground track. This is an important aspect of our emulator.

2004 ICESat freeboard estimates are depicted in Figure 52(a) and Figure 52(b) for the winter and fall seasons, respectively. Recalling Figure 32 which provides a seasonal analysis of sea ice thicknesses for both sea ice models, spatially, the sea ice thickness distribution corresponds fairly well to the ICESat observations. Sea ice thickness values are largest north of the Canadian Archipelago for much of the year and ice thickness values decrease toward the Chuchki Sea and Siberian coast. However, we have calculated the biases in freeboard means to evaluate the model using both freeboard regimes, with and without snow loading.

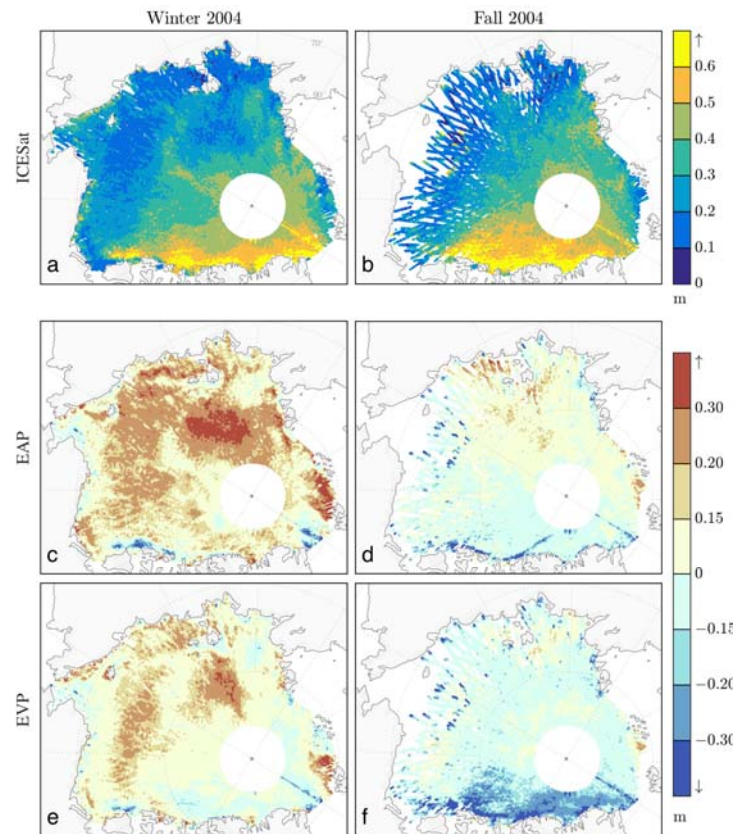


Figure 52. $\langle \overrightarrow{fb}_{obs} \rangle$ for ICESat, calculated for multiple grid-point sampling in a) winter and b) fall 2004. The model bias for these seasons, $Bias(\overrightarrow{fb}_{model})$ is provided in c) and d), respectively, for the RASM simulation using EAP sea ice mechanics, and e) and f) for the EVP sea ice mechanics variant.

For the 2004 EAP winter test, the model has a large bias, overestimating sea ice freeboard across a vast portion of the Arctic with values ranging between 0.15 and 0.3 meters. During the fall, EAP overestimates freeboard near the Arctic hole and Eastern Arctic Ocean, but underestimates across the western Arctic. The EVP sea ice model depicts similar distribution to the EAP for both seasons, with a more widespread region where the bias is -0.30 along the Canadian Archipelago and Greenland coasts. From Figure 52 (c-f), it is evident that both RASM model runs, incorporating the snow loading, have biased sea ice thickness estimates for both the winter and fall seasons. With snow loading included in the freeboard measurements, neither sea ice model accurately represents the sea ice distribution observed by ICESat during the winter and fall months of 2004. Snow loading adds a degree of uncertainty to the calculations within each sea ice model.

2004 ICESat emulator results without snow loading estimates are represented in Figure 53. The $Bias(\overline{fb}_{model}(\overline{h}_s = 0))$, varies between both sea ice models and seasons (Figures 53 (c-f)). Both EAP and EVP models underestimates thickness along the Canadian Archipelago and Fram Strait for both seasons. The EAP model also has a high bias in Barents Sea and Laptev Sea during the winter. Otherwise the EAP matches the ICESat observations fairly well, with freeboard estimates within ± 0.15 meters, which is nearly the same value as the ICESat GLAS uncertainty.

The EVP model has larger $Bias(\overline{fb}_{model}[\overline{h}_s = 0])$ with values exceeding -0.30 across the Eastern Arctic Ocean. The winter season has a smaller difference in the Western Arctic, with values between ± 0.15 meters. For 2004, the EAP model with $Bias(\overline{fb}_{model}(\overline{h}_s = 0))$ has freeboard values closer in proximity to ICESat observations than the EVP sea ice model.

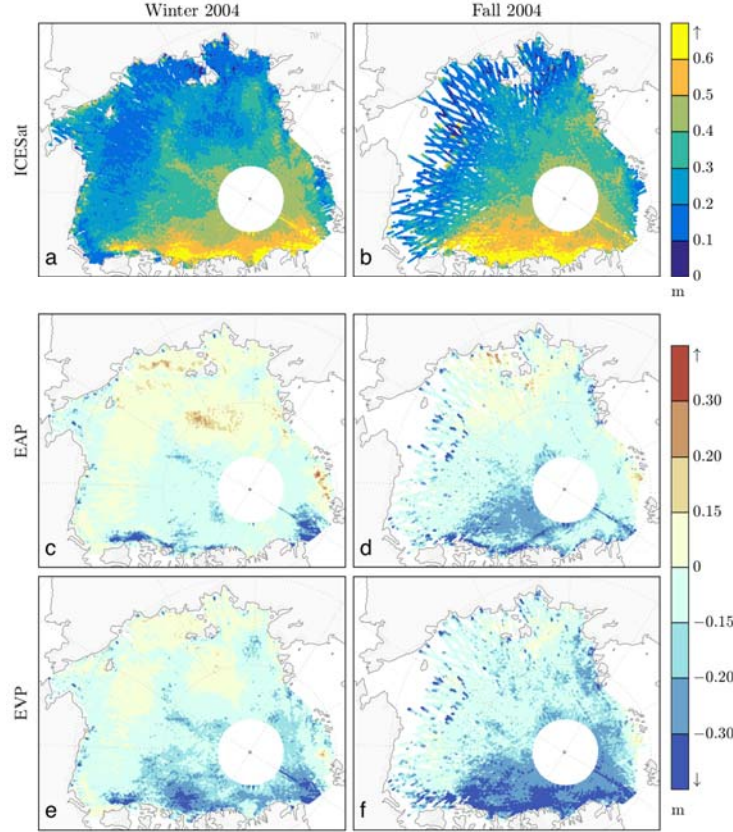


Figure 53. $\langle \overrightarrow{fb}_{obs} \rangle$ for ICESat, calculated for multiple grid-point sampling in a) winter and b) Fall 2004. The model bias for these seasons, $Bias(\overrightarrow{fb}_{model}(\overline{h}_s = 0))$ is provided in c) and d), respectively, for the RASM simulation using EAP sea ice mechanics, and e) and f) for the EVP sea ice mechanics variant.

Further to the ICESat-model comparison presented for 2007 in the previous section, we briefly discuss their relevance in terms of skill, and also present the case for snow was removed from the model freeboard calculations. The freeboard differences between the satellite and models are seen in Figure 54 and Figure 55. Figure 54(a) and 54(b) display the ICESat observations across 9 grid cells, and is repeated from Figure 47 for clarity.

Similar to the 2004 results, there is a large bias in the models using the freeboard with snow regime. EAP bias exceeds +0.30 within the Central Arctic and Barents Sea region during the spring season. For the EAP fall season test, the EAP maintains larger

freeboard values within the Eastern Arctic, but underestimates freeboard in the Western Arctic. The EVP sea ice model shows similar trends in the model bias. As seen with the 2004 emulator run, applying snow loading to freeboard calculations increases uncertainty within the models.

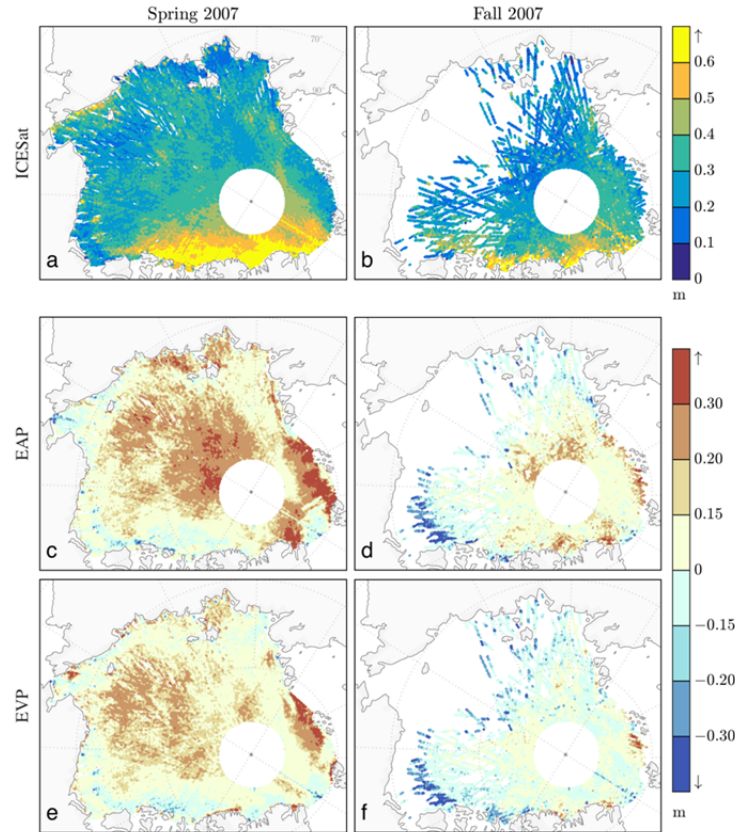


Figure 54. $\langle \overrightarrow{fb}_{obs} \rangle$ for ICESat, calculated for multiple grid-point sampling in a) spring and b) fall 2007. The model bias for these seasons, $Bias(\overrightarrow{fb}_{model})$ is provided in c) and d), respectively, for the RASM simulation using EAP sea ice mechanics, and e) and f) for the EVP sea ice mechanics variant.

EAP and EVP models had similar $Bias(\overrightarrow{fb}_{model}(\overline{h}_s = 0))$ in freeboard measurements when compared against ICESat observations, Figure 55. The largest freeboard biases, -0.3 meters, are along the Canadian Archipelago, Alaska, Siberia and

the Fram Strait during the spring. Both sea ice models have a -0.30 error in the vicinity of the Fram Strait and along the Canadian Archipelago during the fall. Spatially, the spring season had larger regions of sea ice freeboard biases, with the model underestimating freeboard across most of the basin, as compared to the fall.

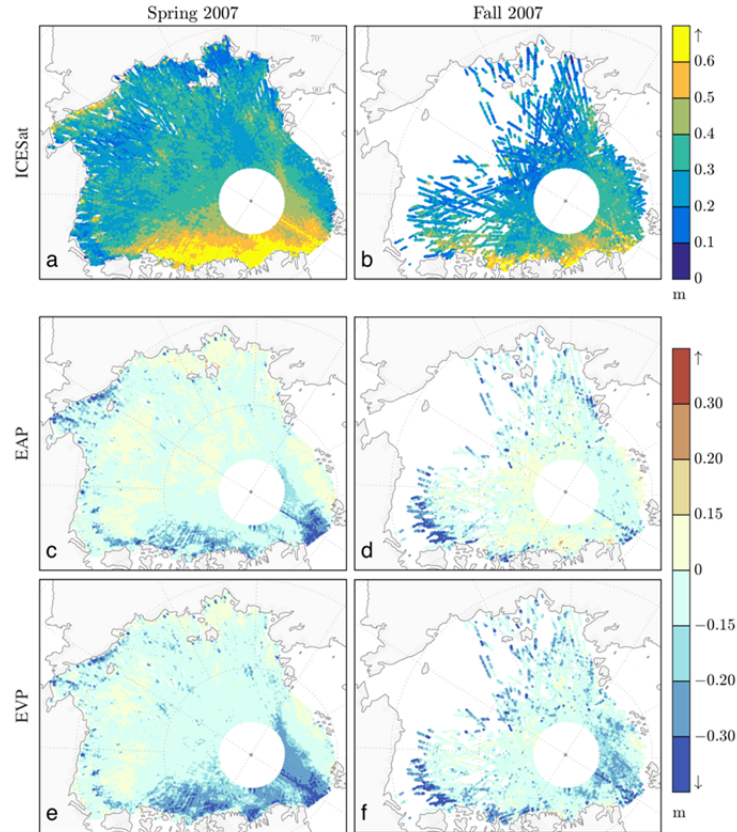


Figure 55. $\langle \overrightarrow{fb}_{obs} \rangle$ for ICESat, calculated for multiple grid-point sampling in a) spring and b) fall 2007. The model bias for these seasons, $Bias(\overrightarrow{fb}_{model}(\bar{h}_s = 0))$ is provided in c) and d), respectively, for the RASM simulation using EAP sea ice mechanics, and e) and f) for the EVP sea ice mechanics variant.

In summary, the EAP and EVP models have very similar thickness distribution, from a spatial perspective. The largest differences between the models and observations occur along the Fram Strait and Canadian Coast. Around the Arctic hole, EAP provides

more accurate measurements. Referencing back to Figures 32 and 33, the largest change in velocity occurs within the Fram Strait for both models, which may partially account for the disparity in freeboard measurements. Additionally, during the 2007 spring and 2004 winter seasons, the transport of sea ice increases along the Canadian coast for the EVP simulation, which may also be a source of uncertainty within the model causing the difference in freeboard measurements. For the freeboard without snow loading, both models have a bias of calculating too low for freeboard measurements in regions of largest differences.

The basin-wide freeboard distributions are represented in Figure 56 for 2004 and Figure 57 for 2007. For the 2004 winter season, both the EVP and EAP models have bimodal distribution of sea ice thickness. $Bias(\overline{fb}_{model}(\overline{h}_s = 0))$, has the most comparable freeboard distribution trends to the ICESat observations. $Bias(\overline{fb}_{model})$ maintains a positive bias for both model configuration (EAP and EVP) and both seasons. Neither model perfectly duplicates the observation tendencies, but significant differences are evident between the two freeboard regimes.

From Figure 56, it is evident that both the RASM tests, incorporating snow loading, overestimates sea ice thickness during the winter and the fall 2004 EAP simulation. However, the EVP model with snow provides the most similar results to the ICESat observations for the fall 2004 season.

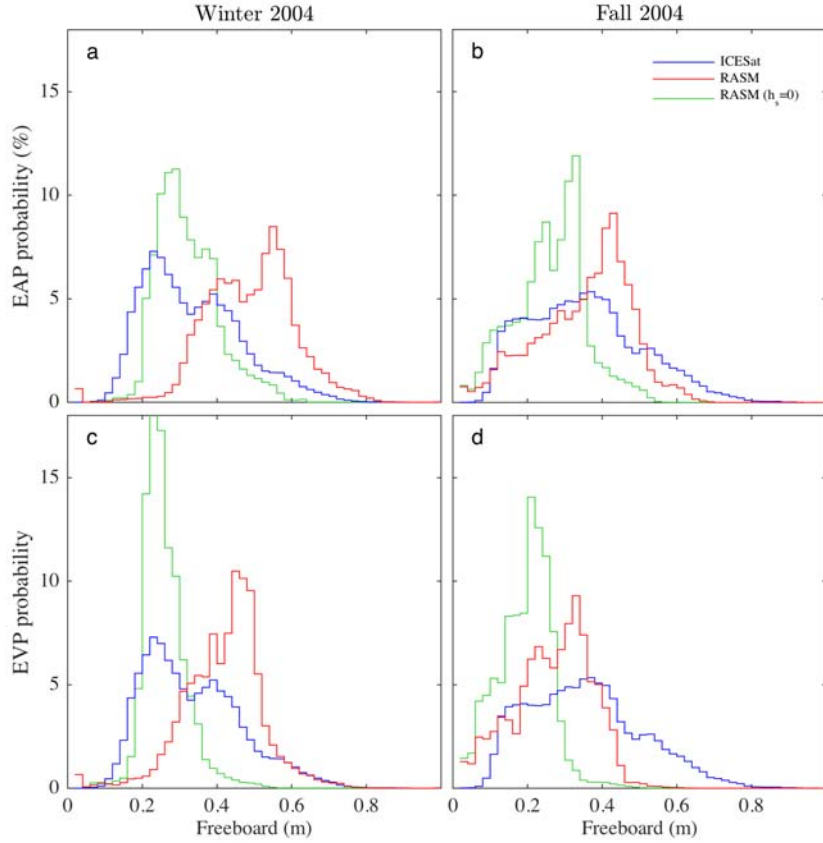


Figure 56. ICESat 2004 freeboard variability. Probability density function of freeboard, analogous to thickness distribution PDF displayed from Hutchings et al. (2008). Blue represents ICESat observations, Red represents multiple grid point sampling technique and magenta represents single grid point sampling.

In 2007, a similar bimodal distribution and outcome was found, Figure 57. The biases between $Bias(\overline{fb}_{model}(\overline{h}_s = 0))$ and $Bias(\overline{fb}_{model})$ are apparent, with the $Bias(\overline{fb}_{model})$ skewed to the right of the ICESat distribution. In both the winter 2004 and spring 2007 seasons, the ICESat freeboard distribution most closely resembles the sea ice model output without snow loading, with the exception being the fall EVP simulation.

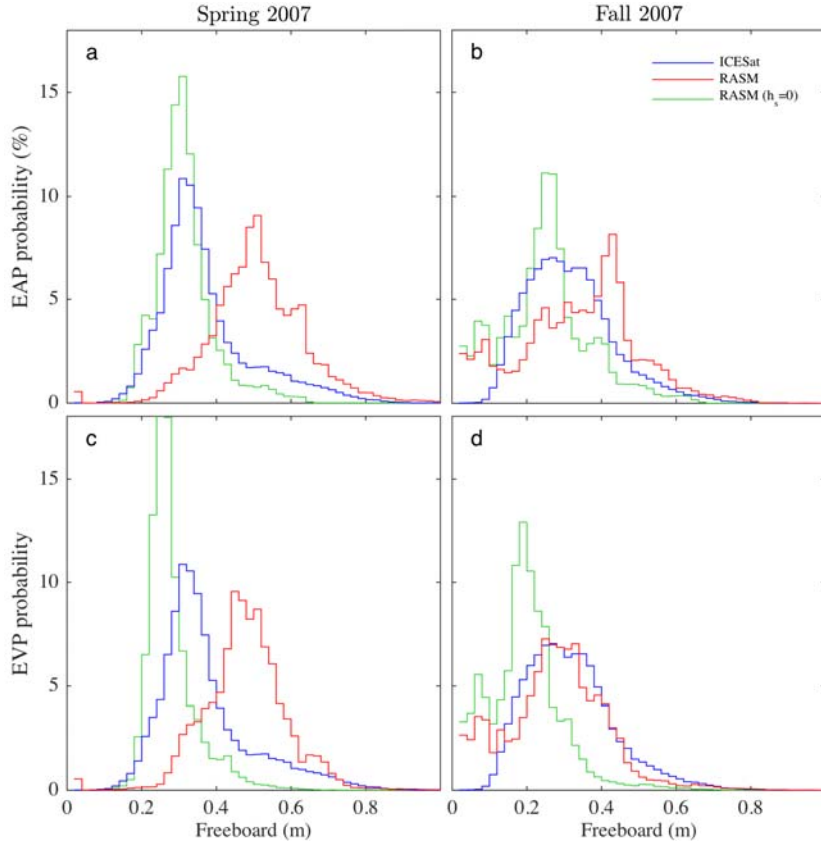


Figure 57. For a more detailed description, see Figure 56. This data is for 2007 central Arctic freeboard

Taylor diagrams were constructed to evaluate the model runs' spatial bias pattern (Figure 58). In winter 2004, the snow loading and non-snow loading for both EVP and EAP runs have nearly the same correlations and root mean square differences from ICESat measurements. With the addition of snow loading, the standard deviation increases, resulting in larger freeboard variances and closer agreement between the model calculations and ICESat observations. The fall 2004 Taylor Diagram (Figure 58(b)) also depicts increasing standard deviation with the snow loading model runs. For the EVP runs, the correlation and RMSD slightly decreases whereas the EAP runs are more or less constant.

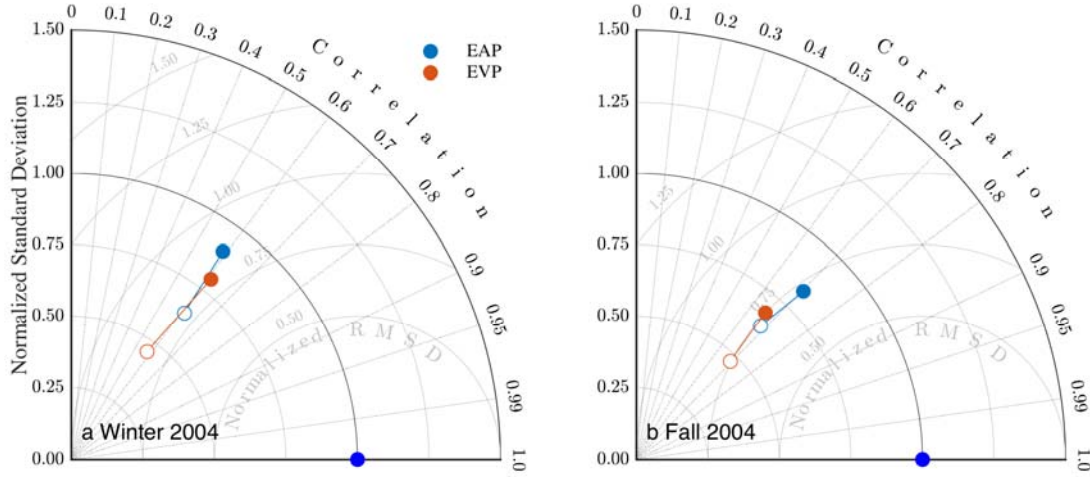


Figure 58. ICESat Emulator 2004: RASM model performance. The EAP results are in light blue, the EVP results are in red and the observations are indicated by the dark blue circle. The solid circles are calculations using freeboard with snow loading, the white circles are calculations using freeboard without snow loading.

The spring 2007 EAP and EVP model configurations depict decreasing correlation, while increasing RMSD and standard deviation (Figure 59). The fall 2007 runs increase normalized standard deviation significantly with the addition of snow, while correlation decreases. All four Taylor diagrams signify that it is important to accurately depict snow loading in order to correctly represent sea ice thickness in climate models, and more importantly, that the snow loading is improving the model estimate of freeboard variance. With these results in hand, we now conclude this thesis by deriving skill scores the nicely summarize these final results.

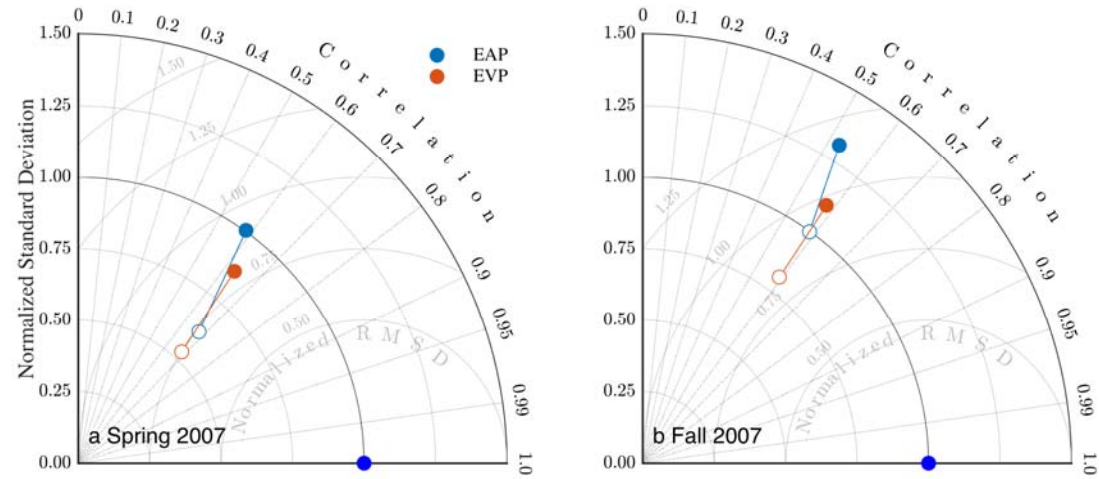


Figure 59. ICESat Emulator 2007: RASM model performance. The EAP results are in light blue, the EVP results are in red and the observations are indicated by the dark blue circle. The solid circles are calculations using freeboard with snow loading, the white circles are calculations using freeboard without snow loading.

THIS PAGE INTENTIONALLY LEFT BLANK

V. CONCLUSION: METRICS FOR EVALUATING SEA ICE MODELS USING SATELLITE ALTIMETRY

A. CULMINATION OF THIS THESIS: SKILL SCORES FOR SEA ICE MODELS USING LASER ALTIMETERS

Arctic sea ice continually undergoes physical changes and its characteristics are strongly seasonal, making it difficult to accurately simulate in models. Due to the effects of dynamics and thermodynamics discussed in Chapter II, sea ice model performance can be relatively poor, but seldom is this performance quantitatively characterized. In this thesis, we have seen that detailed, quantitative analysis of models can be achieved using LASER measurements of freeboard from space.

This thesis has developed a method for using a satellite emulator to maximize usefulness of satellite and aircraft altimetric observations with the intention of quantifying bias in sea ice models. Given the pattern estimates of $\langle \overrightarrow{fb}_{obs} \rangle$ and $\langle \overrightarrow{fb}_{model} \rangle$, across the Arctic basin, we can not only employ pattern Taylor Diagrams, but we can also use the associated skill scores suggested by Taylor (2001) to numerically rate model freeboard skill against comparable variance and correlation with observations. Moreover, for the first time, we are able to do this in a way that is physically consistent between models and observations, and that takes into account observational error.

To do this, we first need to quantify the maximum possible agreement one may expect between models and observations, based upon the measurement error. The maximum pattern correlation for the sampled observed freeboard at each model grid point $\langle \overrightarrow{fb}_{obs} \rangle$ is given by:

$$R_0 = \frac{\frac{1}{N} \sum_{n=1}^N \left(\langle \overrightarrow{fb}_{obs} \rangle \pm \langle \overrightarrow{fb}_{obs} \rangle_{err} - \overline{\langle \overrightarrow{fb}_{obs} \rangle \pm \langle \overrightarrow{fb}_{obs} \rangle_{err}} \right) \left(\langle \overrightarrow{fb}_{obs} \rangle - \overline{\langle \overrightarrow{fb}_{obs} \rangle_{err}} \right)}{\sigma_{f \pm f_{err}} \sigma_f}$$

where the large overbars indicate the basin-wide pattern mean, and we have abbreviated the pattern standard deviation with and without observational error as $\sigma_{f \pm f_{err}}$ and σ_f respectively. The observational error at each model grid cell for the Yi and Zwally (2009) datasets is 0.14 m for each observation, thus error for the arithmetic mean freeboard is

$$\left\langle \overline{fb}_{obs} \right\rangle_{err} = \frac{0.14}{\sqrt{N}},$$

given N ICESat freeboard samples within a model grid cell. Using this information, a weighted variance skill score (Taylor 2001), is given by:

$$S_v = \frac{4(1+R)}{(\hat{\sigma}_f + 1/\hat{\sigma}_f)^2 (1 - R_o)}$$

and weighted correlation skill score using Taylor (2001) equation:

$$S_c = \frac{4(1+R)^4}{(\hat{\sigma}_f + 1/\hat{\sigma}_f)^2 (1 - R_o)^4}$$

where $\hat{\sigma}_f = \sigma_{model} / \sigma_{obs}$ for the pattern standard deviations of model and observed freeboard along satellite tracks. Using these skill scores, one is able to summarize numerically the graphical representation of the results in Taylor diagrams at the end of Chapter IV.

The results from these skill scores are annotated in Table 7 and Table 8 for the model bias results presented and discussed in the last part of Chapter IV. The variance weighted skill scores are larger for the EAP simulations for both 2007 and 2004. For the weighted correlation skill scores, neither EAP nor EVP perform noticeably better than one-another. Importantly, R_o values ranged from 0.994-0.999 for all model runs, meaning that the best possible values one might expect are surprisingly close to the observed values on Taylor Diagrams presented in Chapter IV.

These skill scores are the most important outcome from this thesis, because, regardless of their exact values, they give a clear, concise, quantitative summary of the

performance of a sea ice model's ability to simulate the sea ice thickness distribution, $g(h_i)$ and snow distribution $g(h_s)$. Moreover, the basin-wide model biases associated with the skill scores are statistically significant across the entire basin, and represent a relatively slender period of time (about one month), making the score useable from just a short duration of satellite retrievals. This makes the methods described in this thesis equally applicable to Navy seasonal sea ice forecasts, and to evaluating centennial scale climate models.

Table 7. Variance and correlation weighted skill scores for fall 2004 and 2007

FALL		2004		2007	
		<i>fb</i>	<i>fb(hs=0)</i>	<i>fb</i>	<i>fb(hs=0)</i>
Variance Weighted	EAP	0.824	0.691	0.712	0.795
	EVP	0.720	0.507	0.785	0.763
Correlation Weighted	EAP	0.511	0.412	0.319	0.399
	EVP	0.413	0.308	0.390	0.388

Table 8. Variance and correlation weighted skill scores for winter 2004 and spring 2007

		2004 (WINTER)		2007 (SPRING)	
		<i>fb</i>	<i>fb(hs=0)</i>	<i>fb</i>	<i>fb(hs=0)</i>
Variance Weighted	EAP	0.786	0.670	0.793	0.676
	EVP	0.766	0.453	0.799	0.577
Correlation Weighted	EAP	0.394	0.351	0.396	0.400
	EVP	0.402	0.222	0.434	0.344

B. CONCLUSIONS

As the Arctic environment continues to change, maximizing the use of available observations is essential to understanding sea ice thickness and physical processes. Sea ice is a fundamental component of the Arctic and global climate systems, but is difficult

to accurately model due to the many physical processes influencing growth, drift, deformation and melt and there are limited observations of it across much of the Arctic region. As discussed in Chapter II, sea ice thickness measurements over large distances are difficult to obtain. With the current rapid climatic shift of the Arctic sea ice regime from multi-year to first-year ice, it is essential to accurately depict the sea-ice thickness distribution across the Arctic in sea-ice models.

For this thesis, we used freeboard as a proxy for evaluating the thickness distribution, $g(h_i)$, in one model (RASM), but the technique developed is broadly applicable to all sea ice models simulating at least a month of continuous thickness changes. This thesis has shown that altimetric freeboard observations from aircraft and from space, and with relatively small surface footprints, can be used with a high degree of statistical confidence in estimating model bias. In so doing, it has also been demonstrated, using planned ICESat-2 orbital tracks, that relatively small sample bias exists over the 91-day repeat orbits used for ICESat and, from next year, for ICESat-2. Using two independent observation datasets, OIB and ICESat, weak spatial noise relationships were exploited to improve the statistical significance of the final estimates of model bias, and model skill. High-resolution models, below 10 km grid cell size, can take advantage of the technique employed in this work to improve statistical confidence. However, global climate models typically operate outside the range of the weak spatial noise relation identified in ICESat and OIB data, and so can only employ single grid-point sampling when comparing observed and modeled freeboard.

A primary objective of this thesis was to arrive at a basic design criteria for an ICESat/ICESat-2 emulator that can be instituted in CICE, and used by the ice prediction community. This objective has been achieved. The techniques presented in this thesis can be used to routinely output model statistics that compare simulations of $g(h_i)$ with ICESat-2 observations when the satellite is launched next year. This will put the research community a step closer to producing intercomparable metrics, and to properly accounting for model skill, or the lack thereof. These efforts will support both national and U.S. Navy strategies within the Arctic region, by pursuing scientific advancements to

reduce uncertainty and further understand why the Arctic environment is changing at an unprecedented rate.

C. RECOMMENDATIONS FOR FUTURE STUDIES

This research did not investigate total volume distribution of the Arctic, nor variations in sea ice and snow density on skill. Therein rests work to be undertaken to extend on the results presented here. Instead, this research focused on deriving skill metrics applicable to a broad range of sea ice models and freeboard measurements. Hence, techniques developed in this thesis can also be applied to other Arctic sea ice freeboard and draft data collections, such as CryoSat-2 and submarine profiles, in addition to OIB and other measurements across the Antarctic. The methodology may even be applied to different geophysical variables predicted by models to quantify model skill.

From here, the next step is to institute the ICESat/ICESat-2 emulator design into a version of CICE so that the calculated metrics can be automatically output. Realistically, density varies significantly across the pack. Seasonal variation in brine pockets, first year ice distribution and ridged ice rubble can also significantly impact bulk sea ice density and hence overall Arctic sea ice volume estimated from freeboard in observations. Consequently, different assumptions about ice densities, as well as about snow cover, used in converting freeboard to ice thickness can strongly impact sea ice thickness estimates, and hence estimates of total Arctic sea ice mass. Therefore, future research building upon the work here needs to account for density heterogeneity. With the projected launch of ICESat-2 in December 2017, there is no better time to proceed with this research than the present.

THIS PAGE INTENTIONALLY LEFT BLANK

APPENDIX ADDITIONAL ICESAT-2 EMULATOR RESULTS

The following Figures are the $Bias(\overline{fb}_{ICESat-2})$ and Welch's t-test results for the ICESat-2 emulator for the summer and winter season of 2007 and full series for 1996. As seen in Chapter IV, both the single grid point and multiple grid point results are provided. The freeboard bias was calculated by using snow in the freeboard measurements for all Figures 60 to 71.

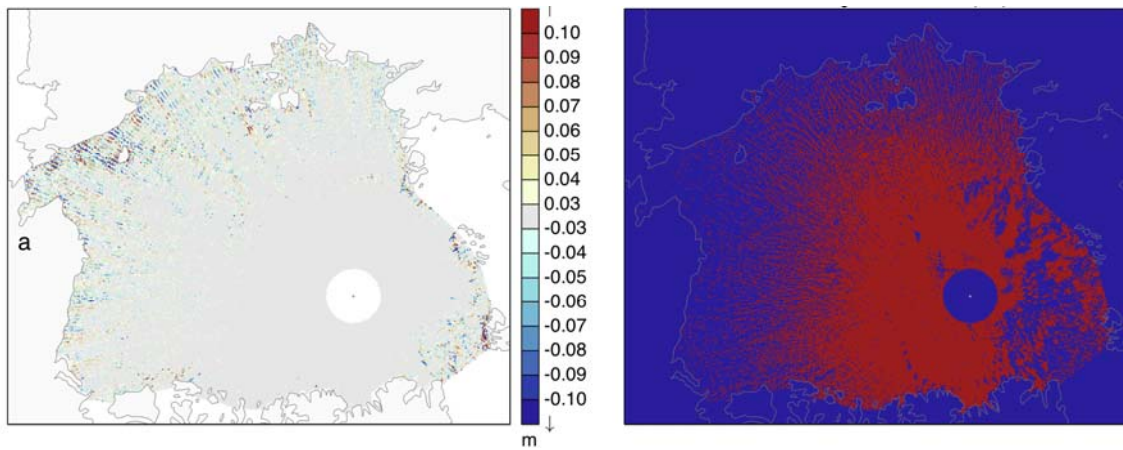


Figure 60. a) 2007 $Bias(\overline{fb}_{ICESat-2})$ for freeboard sampled along ICESat-2 tracks for one complete 91-day repeat orbit period over the winter for January to March using the ICESat-2 emulator and RASM described in Chapter III. b) Differences in (a) that are statistically significant at the 95% confidence interval (red). In this case, only model grid cells were sampled directly under each satellite track with ± 1 hour of the satellite pass as shown in Figure 30.

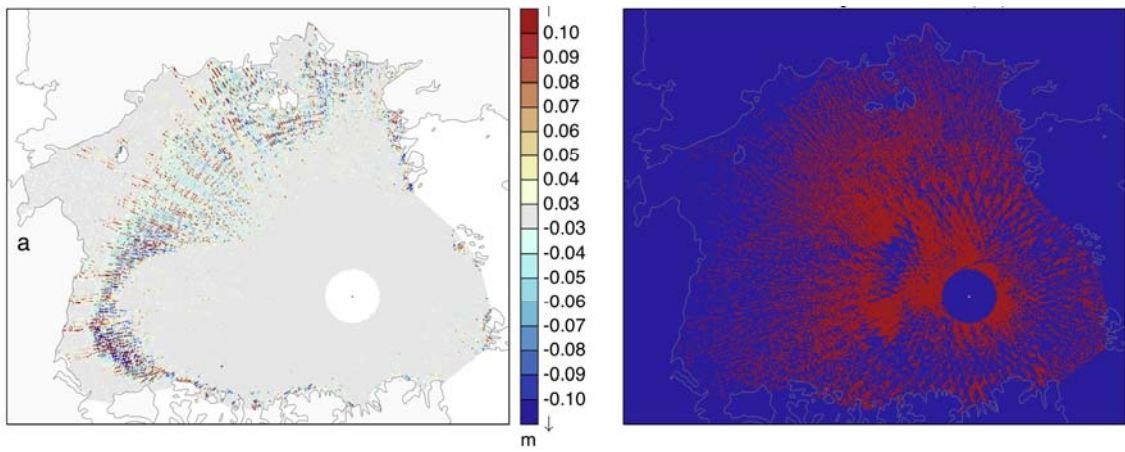


Figure 61. a) For a more detailed description, see Figure 60. This data is for summer months July to September 2007 over one complete 91-day repeat orbital period.

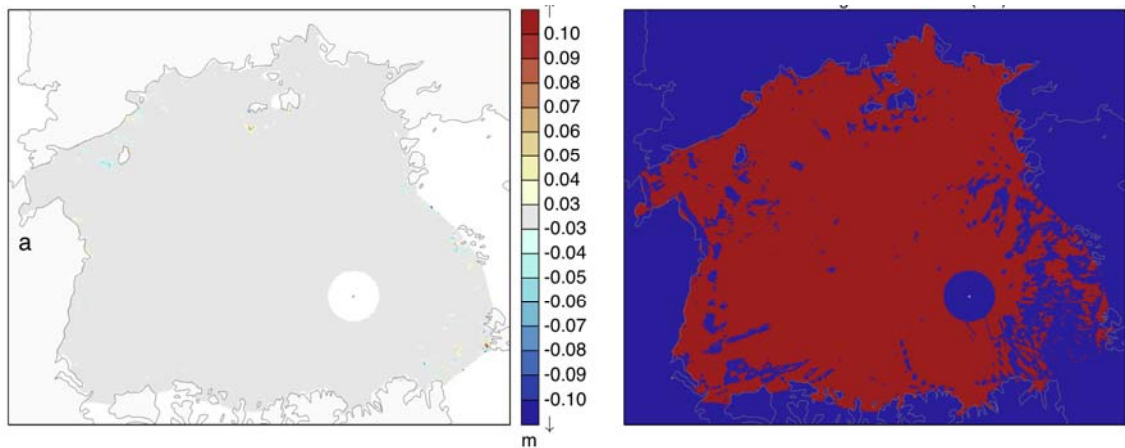


Figure 62. 2007 $Bias(\bar{fb}_{ICESat-2})$ for freeboard sampled along ICESat-2 tracks for one complete 91-day repeat orbit period over the winter for January to March using the ICESat-2 emulator and RASM described in Chapter III using multiple grid-point sampling. b) Differences in (a) that are statistically significant at the 95% confidence interval (red).

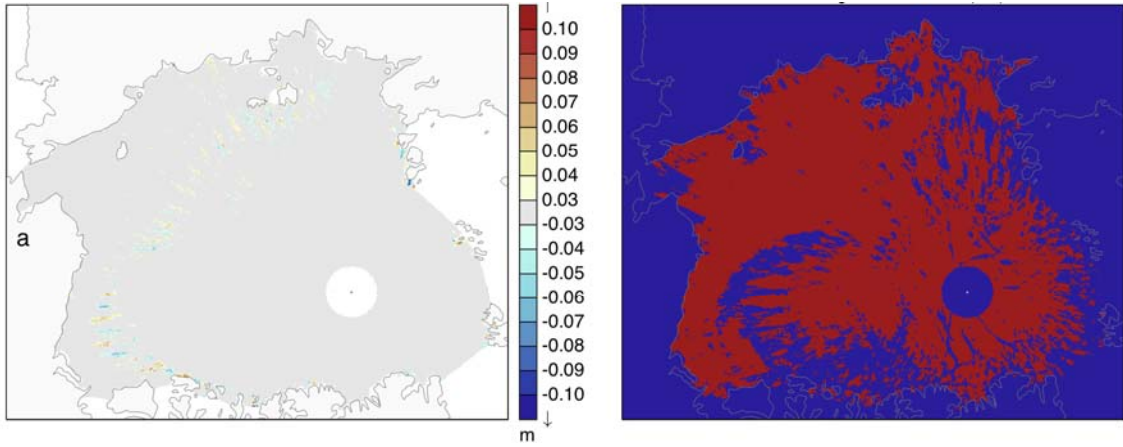


Figure 63. For a more detailed description, see Figure 62. This data is for summer months July to September 2007 over one complete 91-day repeat orbital period.

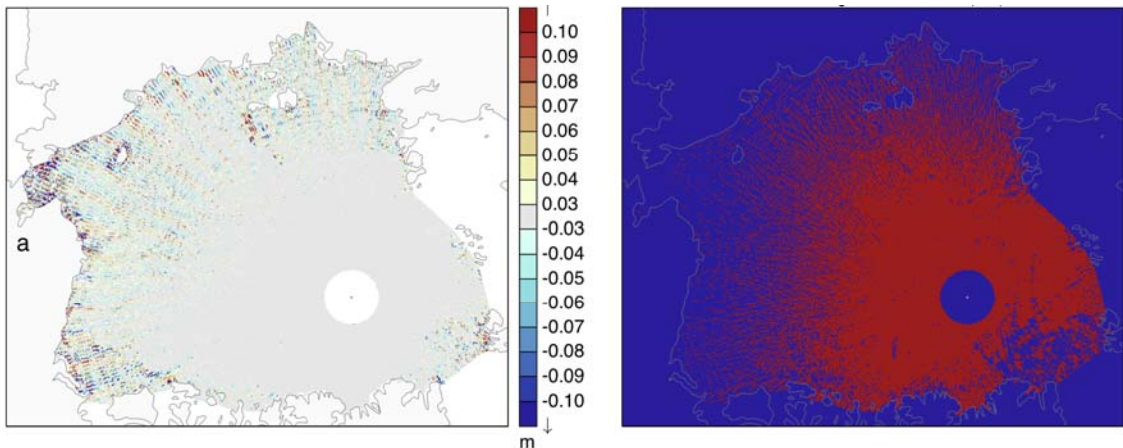


Figure 64. a) 1996 $Bias(\bar{fb}_{ICESat-2})$ for freeboard sampled along ICESat-2 tracks for one complete 91-day repeat orbit period over the winter for January to March 1996 using the ICESat-2 emulator and RASM described in Chapter III. b) Differences in (a) that are statistically significant at the 95% confidence interval (red). In this case, only model grid cells were sampled directly under each satellite track with ± 1 hour of the satellite pass as shown in Figure 30.

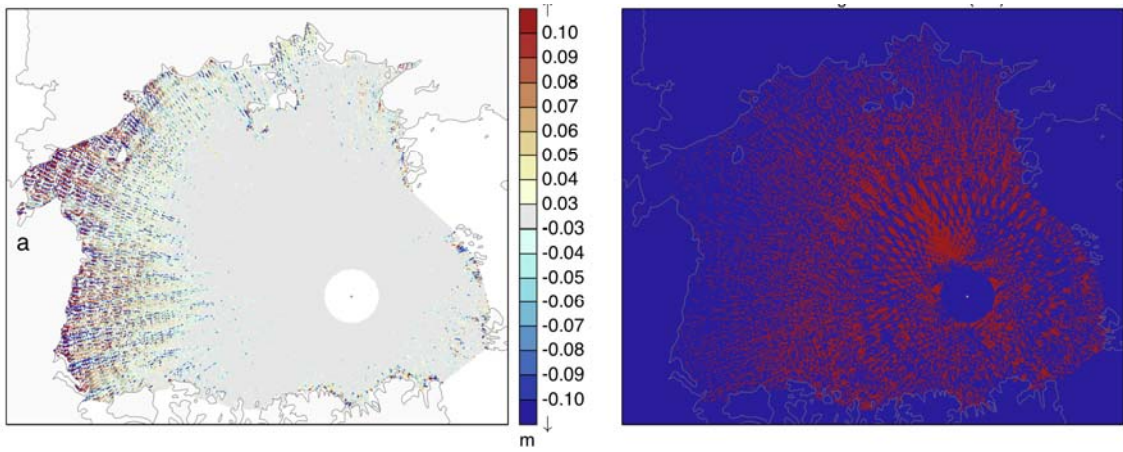


Figure 65. a) For a more detailed description, see Figure 64. This data is for spring months April to June 1996 over one complete 91-day repeat orbital period.

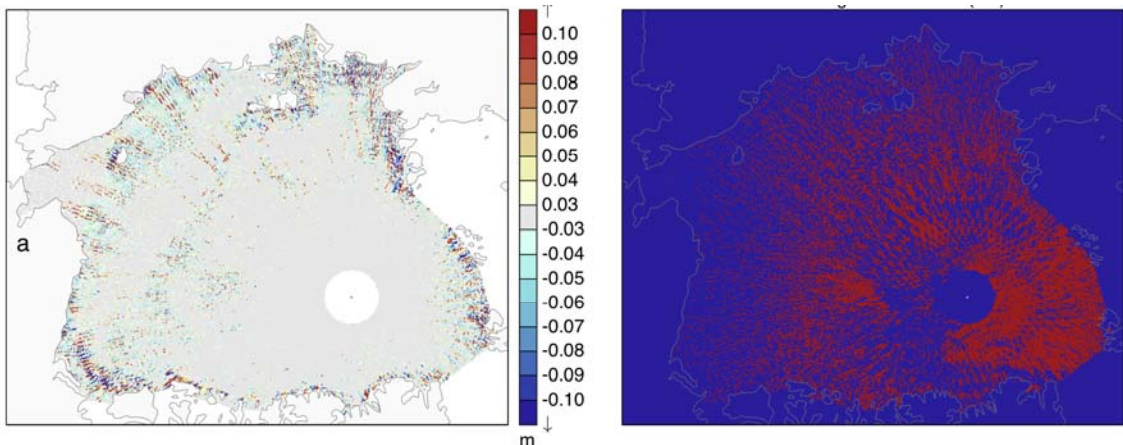


Figure 66. a) For a more detailed description, see Figure 64. This data is for but for fall months July to September 1996 over one complete 91-day repeat orbital period.

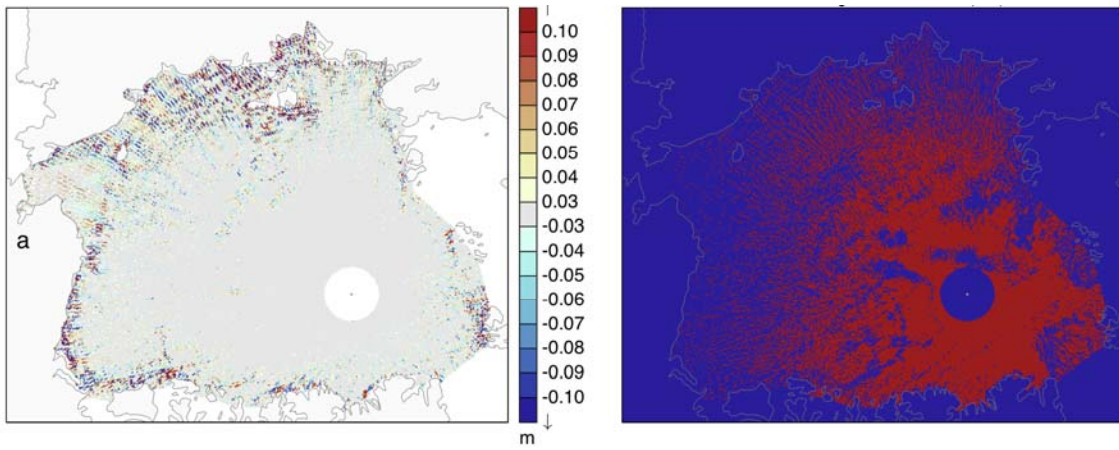


Figure 67. For a more detailed description, see Figure 64. This data is for fall months October to December 1996 over one complete 91-day repeat orbital period.

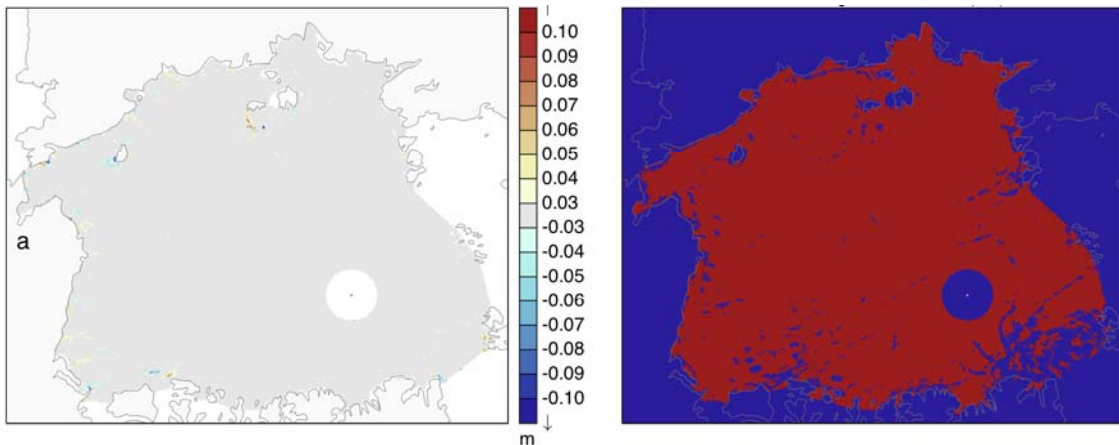


Figure 68. a) 1996 $Bias(\bar{fb}_{ICESat-2})$ for freeboard sampled along ICESat-2 tracks for one complete 91-day repeat orbit period over the winter for January to March using the ICESat-2 emulator and RASM described in Chapter III using multiple grid-point sampling. b) Differences in (a) that are statistically significant at the 95% confidence interval (red).

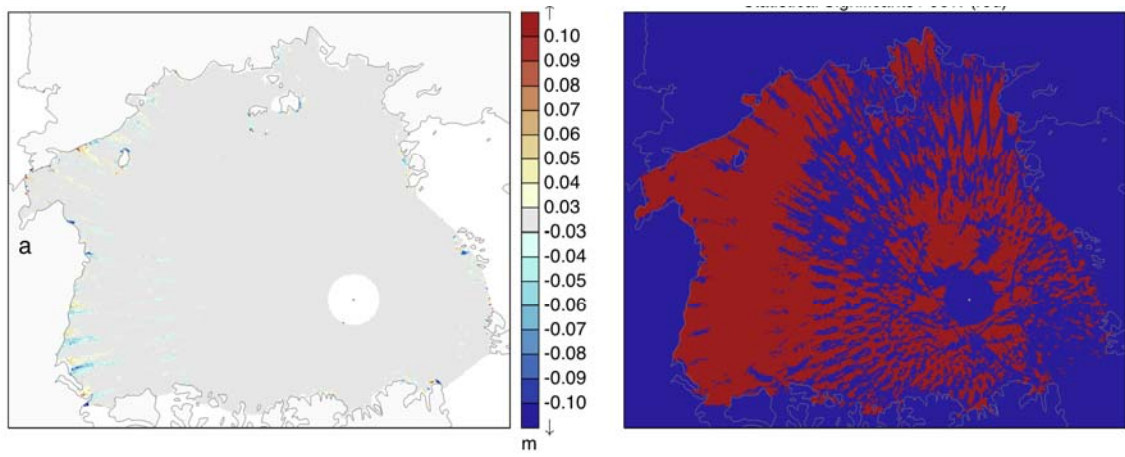


Figure 69. For a more detailed description, see Figure 68. This data is for spring months April to June 1996 over one complete 91-day repeat orbital period.

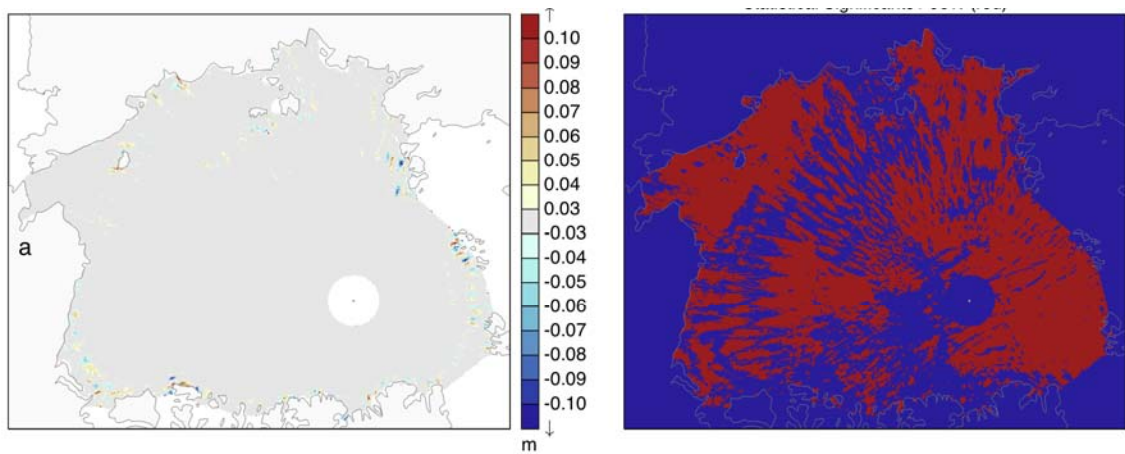


Figure 70. For a more detailed description, see Figure 68. This data is for summer months July to September 1996 over one complete 91-day repeat orbital period.

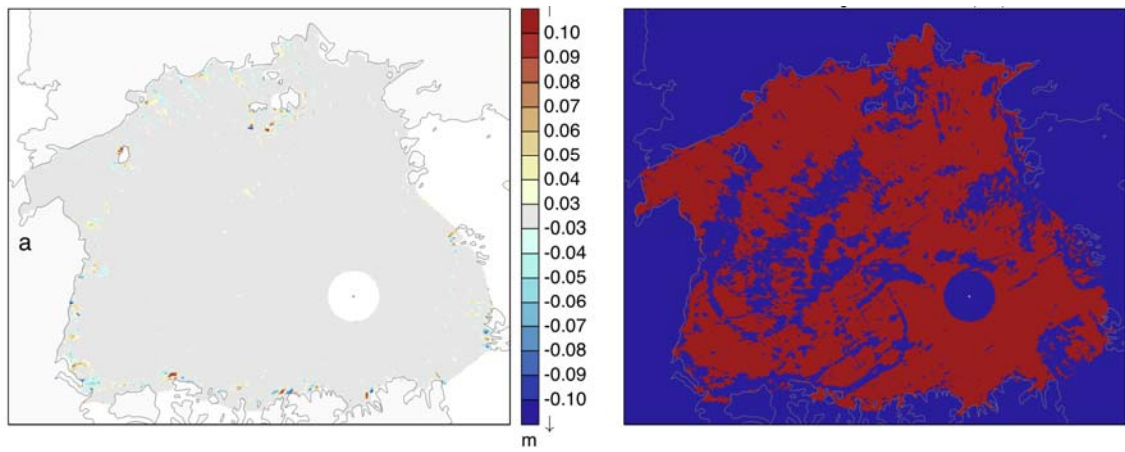


Figure 71. For a more detailed description, see Figure 68. This data is for fall months October to December 1996 over one complete 91-day repeat orbital period.

THIS PAGE INTENTIONALLY LEFT BLANK

LIST OF REFERENCES

Abdalati, W., and Coauthors, 2010: The ICESat-2 laser altimetry mission. *Proc. IEEE*, **98**, 735–751, doi:10.1109/JPROC.2009.2034765.

Alexadrov, V., J. Wahlin, and O. M. Johannessen, 2010: The relation between sea ice thickness and freeboard in the Arctic. *The Cryosphere*, **4**, 373–380, doi:10.5194/tc-4-373-2010.

America's Navy, 2016: ICEX 2016 Camp Operations Conclude Successfully; Submarine Ops Continue. Accessed May 2016. [Available at http://www.navy.mil/submit/display.asp?story_id=93833.]

Arctic Council, 2016: The Arctic Council: A backgrounder. Accessed February 2016. [Available online at <http://www.arctic-council.org/index.php/en/about-us/member-states>.]

Arrigo, K.R., and Coauthors, 2012: Massive phytoplankton blooms under Arctic Sea ice. *Science*, **336**, 1408, doi:10.1126/science.1215065.

Bitz, C. M., and W. H. Lipscomb, 1999: An energy-conserving thermodynamic model of sea ice. *J. Geophys. Res.*, **104**:15669–15677.

Briegleb, B. P and B. Light, 2007: A delta-eddington multiple scattering parameterization for solar radiation in the sea ice component of the Community Climate System Model. NCAR Tech Note TN-472+STR, 100 pp.

Cassano, J., A. DuVivier, A. Roberts, M. Hughes, M. Seefeldt, M. Brunke, A. Craig, B. Fisel, W. Gutowski, J. Hamman, M. Higgins, W. Maslowski, B. Nijssen, R. Osinski, and X. Zeng (2016), Near surface atmospheric climate of the Regional Arctic System Model (RASM), conditionally accepted for *Journal of Climate*.

Clement, J. L., W. Maslowski, L. W. Cooper, J. M. Grebmeier, and W. Walczowski, 2005: Ocean circulation and exchanges through the northern Bering Sea—1979–2001 Model results. *Deep. Res. Part II Top. Stud. Oceanogr.*, **52**, 3509–3540, doi:10.1016/j.dsr2.2005.09.010.

Climate Policy Oberver, 2016: Accessed January 2016. Arctic shipping-Commercial opportunities and challenges. [Available at: <http://climateobserver.org/reports/arctic-shipping-commercial-opportunities-and-challenges/>.]

CMIP, 2009: CMIP3-Overview. Accessed 26 April 2016. [Available at http://cmip-pcmdi.llnl.gov/cmip3_overview.html?submenuheader=1.]

Cohen, J., and Coauthors, 2014: Recent Arctic amplification and extreme mid-latitude weather. *Nature Geoscience*, **7**, 627–637, doi: 10.1038/ngeo2234.

Comiso, J.C., 2011: Large decadal decline of the Arctic multiyear ice cover. *Journal of Climate*, **25**, 1176–1193, doi:10.1175/JCLI-D-11-00113.1.

Davis, N. R., and P. Wadhams, 1995: A statistical analysis of Arctic pressure ridge morphology, *J. Geophys. Res.*, **100**(C6), 10915–10925.

Donghui, Yi, J. P. Harbeck, S. S. Manizade, N. T. Kurtz, M. Studinger, and M. Hofton, 2015: Arctic Sea ice freeboard retrieval with waveform characteristics for NASA's airborne topographic mapper (ATM) and land, vegetations, and ice sensor (LVIS). *Geoscience and Remote Sensing, IEEE Transactions on*, **53**, 1403–1410.

Dukowicz, J. and R. Smith, 1994: Implicit free-surface formulation of the bryan-cox-semtner ocean model. *J. Geophys. Res.*, **99**, 7991–8014.

EIA, 2009: Arctic Oil and Natural Gas Potential. Accessed May 2016. [Available at <http://www.eia.gov/oaif/analysispaper/arctic/>.]

Farrell, S. L., and Coauthors, 2012: A first assessment of IceBridge snow and ice thickness data over Arctic sea ice. *IEEE Trans. Geosci. Remote Sens.*, **50**, 2098–2111, doi:10.1109/TGRS.2011.2170843.

Farrell, S. L., S. W. Laxon, D. C. McAdoo, D. Yi, and H. J. Zwally, 2009: Five years of Arctic sea ice freeboard measurements from the Ice, Cloud and Land Elevation Satellite. *J. Geophys. Res. Ocean.*, **114**, C04008, doi:10.1029/2008JC005074.

Feltham, D. L, 2008: Sea Ice Rheology. *Annu. Rev. Fluid Mech.*, **40**, 91–112, doi: 10.1146/annurev/fluid.40.111406.102151.

Fichefet, T., and M. a. M. Maqueda, 1997: Sensitivity of a global sea ice model to the treatment of ice thermodynamics and dynamics. *J. Geophys. Res.*, **102**, 12609–12645, doi:10.1029/97JC00480.

Francis, J. A. and S. J. Vavrus, 2012: Evidence linking Arctic amplification to extreme weather in mid-latitudes. *Geophys. Res. Lett.*, **39**, L06801, doi: 10.1029/2012GL051000.

Geiger, C., P. Wadhams, H.-R. Müller, J. Richter-Menge, J. Samluk, T. Deliberty, and V. Corradina, 2015: On the uncertainty of sea-ice isostasy. *Ann. Glaciol.*, **56**, 341–352, doi:10.3189/2015AoG69A633.

Gloersen, P., W. J. Campbell, D. J. Cavalieri, J. C. Comiso, C. L. Parkinson, and H. J. Zwally, 1993: Satellite passive microwave observations and analysis Arctic and Antarctic Sea Ice, 1978–1987. *Ann. Glaciol.*, **17**, 149–154.

Hamman, J., B. Nijssen, M. Brunke, J. Cassano, A. Criag, A. DuVivier, M. Hughes, D. Lettenmaier, W. Maslowski, R. Osinski, A. Roberts and X. Zeng (2016), The land surface climate in the Regional Arctic System Model, conditionally accepted for *Journal of Climate*.

Heath, T. L., 1837: *The Works of Archimedes*. Cambridge University Press, 257 pp.

Hibler, W. D., 1979: A Dynamic Thermodynamic Sea Ice Model. *J. Phys. Oceanogr.*, **9**, 815–846, doi:10.1175/1520-0485(1979)009<0815:ADTSIM>2.0.CO;2.

Hunke, E. C., and J. K. Dukowicz, 1997: An elastic–viscous–plastic model for sea ice dynamics. *J. Phys. Oceanogr.*, **27**, 1849–1867, doi:10.1175/1520-0485(1997)027<1849:AEVPMF>2.0.CO;2.

Hunke, E. C., and W. H. Lipscomb, A. K. Turner, N. Jeffery, and S. Elliot, 2015: *CICE: the Los Alamos Sea Ice Model Documentation and Software User's Manual* Version 5.1 LA-CC-06-012.

Hutchings, J., and Coauthors, 2008: Role of ice dynamics in the sea ice mass balance, *Eos. Trans. AGU*, **89**, 515–516, doi: 10.1029/2008EO500003.

IPCC, 2013: Climate Change 2013: The physical science basis: Contribution of working group 1 to the fifth assessment report of the intergovernmental panel on climate change, edited by T. F. Stocker, D. Qin, G.-K. Plattner, M. Tignor, S. K. Allen, J. Boschung, A. Nauels, Y. Xia, V. Bex, and P. M. Midgley, Cambridge University Press.

Jeffries, M. O., J. E. Overland, and D. K. Perovich, 2013: The Arctic shifts to a new normal, *Phys. Today*, **66**, 35–40.

Kinnard, C., C. M. Zdanowicz, D. a. Fisher, E. Isaksson, A. de Vernal, and L. G. Thompson, 2011: Reconstructed changes in Arctic sea ice over the past 1,450 years. *Nature*, **479**, 509–512, doi:10.1038/nature10581. <http://dx.doi.org/10.1038/nature10581>.

Kurtz, N. T., and S. L. Farrell, 2011: Large-scale surveys of snow depth on Arctic sea ice from Operation IceBridge. *Geophys. Res. Lett.*, **38**, L20505, doi:10.1029/2011GL049216.

Kurtz, N. T., S. L. Farrell, M. Studinger, N. Galin, J. P. Harbeck, R. Lindsay, V. D. Onana, B. Panzer, and J. G. Sonntag, 2013: Sea ice thickness, freeboard, and snow depth products from Operation IceBridge airborne data. *The Cryosphere*, **7**, 1035–1056. doi:10.5194/tc-7-1035-2013.

Kurtz, N. T., T. Markus, D. J. Cavalieri, L. C. Sparling, W. B. Krabill, A. J. Gasiewski, and J. G. Sonntag, 2009: Estimation of sea ice thickness distributions through the combination of snow depth and satellite laser altimetry data. *J. Geophys. Res.*, **114**, C10007, doi:10.1029/2009JC005292. papers2://publication/doi/10.1029/2009JC005292.

Kurtz, N., M. S. Studinger, J. Harbeck, V. Onana, and D. Yi., 2015: IceBridge L4 sea ice freeboard, snow depth, and thickness, Version 1. [IDCS14]. Boulder, Colorado USA. NASA National Snow and Ice Data Center Distributed Active Archive Center. doi: <http://dx.doi.org/10.5067/G519SHCKWQV6>. Date Accessed: March 2016.

Kwok, R., and D. A. Rothrock, 2009: Decline in Arctic sea ice thickness from submarine and ICESat records: 1958–2008. *Geophys. Res. Lett.*, **36**, L15501, doi:10.1029/2009GL039035.

Kwok, R., and G. F. Cunningham, 2008: ICESat over Arctic sea ice: Estimation of snow depth and ice thickness. *J. Geophys. Res. Ocean.*, **113**, 1–17, doi:10.1029/2008JC004753Kwok, R, G. F. Cunningham, H. J. Zwally, and D. Yi, 2006: ICESat over Arctic sea ice: Interpretation of altimetric and reflectivity profiles. *J. Geophys. Res. Ocean.*, **111**, C06006, doi:10.1029/2005JC003175.

Kwok, R., B. Panzer, C. Leuschen, S. Pang, T. Markus, B. Holt, and S. Gogineni, 2011: Airborne surveys of snow depth over Arctic sea ice. *J. Geophys. Res. Ocean.*, **116**, C11018, doi:10.1029/2011JC007371.

Kwok, R., G. F. Cunningham, H. J. Zwally, and D. Yi, 2007: Ice, Cloud, and land Elevation Satellite (ICESat) over Arctic sea ice: Retrieval of freeboard. *J. Geophys. Res. Ocean.*, **112**, C12013, doi:10.1029/2006JC003978.

Kwok, R., G. F. Cunningham, M. Wensnahan, I. Rigor, H. J. Zwally, and D. Yi, 2009: Thinning and volume loss of the Arctic Ocean sea ice cover: 2003–2008, *J. Geophys. Res.*, **114**, C07005, doi:10.1029/2009JC005312.

Kwok, R., G. F. Cunningham, S. S. Manizade, and W. B. Krabill, 2012: Arctic sea ice freeboard from IceBridge acquisitions in 2009: Estimates and comparisons with ICESat. *J. Geophys. Res. Ocean.*, **117**, C02018, doi:10.1029/2011JC007654.

Kwok, R., H. J. Zwally, and D. Yi, 2004: ICESat observations of Arctic sea ice: A first look. *Geophys. Res. Lett.*, **31**, L16401, doi:10.1029/2004GL020309.

Laxon, S. W., and Coauthors, 2013: CryoSat-2 estimates of Arctic sea ice thickness and volume. *Geophys. Res. Lett.*, **40**, 732–737, doi:10.1002/grl.50193.

Liang, X., 1994: A two-layer variable infiltration capacity land surface representation for general circulation models, *Water Resour. Series*, **TR140**, 208 pp., Univ. of Washington, Seattle.

Lindsay, R., 2010: New unified sea ice thickness climate data record, *Eos Trans. AGU*, **91**, doi:10.1029/2010EO440001.

Lipscomb, W. H., 2001: Remapping the thickness distribution in sea ice models. *J. Geophys. Res.*, **106**, 13989, doi:10.1029/2000JC000518

Maslowski, W., J. Clement Kinney, M. Higgins, and A. Roberts, 2012: The future of Arctic sea Ice. *Annu. Rev. Earth Planet. Sci.*, **40**, 625–654, doi:10.1146/annurev-earth-042711-105345.

Maykut, G. A. and N. Untersteiner, 1971: Some results from a time-dependent thermodynamic model of sea ice. *Journal of Geophysical Research*, **76**, 1550–1575, doi: 10.1029/JC076i006p01550.

Meier, W., F. Fetterer, M. Savoie, S. Mallory, R. Duerr, and J. Stroeve. 2013, updated 2015. *NOAA/NSIDC Climate Data Record of Passive Microwave Sea Ice Concentration, Version 2*. [g02202_v2]. Boulder, Colorado USA. NSIDC: National Snow and Ice Data Center. doi: <http://dx.doi.org/10.7265/N55M63M1>. Date Accessed: May 2016.

NASA, 2007: NASA's ICESat: One billion elevations served. Accessed 26 April 2016. [Available at http://www.nasa.gov/vision/earth/lookingatearth/icesat_billion.html.]

NASA, 2012: Airborne topographic mapper. Accessed 05 January 2016. [Available at <https://airbornescience.nasa.gov/instrument/ATM> 2012.]

NASA, 2015: ICESat Cryospheric Sciences Lab. Accessed 31 May 2016. [Available at <http://icesat.gsfc.nasa.gov/icesat/glas.php>.]

NASA, 2016a: ICESat-2: Instrument. Accessed 22 February 2016. [Available at <http://icesat.gsfc.nasa.gov/icesat2/instrument.php> 2016.]

NASA, 2016b: LASER operational periods. Accessed 23 April 2016. [Available at http://nsidc.org/data/icesat/laser_op_periods.html.]

Naval Postgraduate School, 2016: Regional Arctic System Model. Accessed 01 March 2016. [Available at <http://www.oc.nps.edu/NAME/RASM.htm>.]

New York Times, 2007: Russians plant flag on the Arctic seabed. Accessed 11 May 2016. [Available at <http://www.nytimes.com/2007/08/03/world/europe/03arctic.html>.]

New York Times, 2015: Russia rearms for a new era. Accessed 01 May 2016. [Available at <http://www.nytimes.com/interactive/2015/12/24/world/asia/russia-arming.html>.]

New York Times, 2016: Russia presents revised claim of Arctic territory to the United Nations. Accessed 20 March 2016. [Available at [http://www.nytimes.com/2016/02/10/world/europe/russia-to-present-revised-claim-of-arctic-territory-to-the-united-nations.html?_r=0.\]](http://www.nytimes.com/2016/02/10/world/europe/russia-to-present-revised-claim-of-arctic-territory-to-the-united-nations.html?_r=0.)

NOAA, 2014: Air Temperature. Accessed 03 May 2016. [Available at [http://www.arctic.noaa.gov/report14/air_temperature.html.\]](http://www.arctic.noaa.gov/report14/air_temperature.html.)

NOAA, 2015: Sea ice. Accessed 22 February 2016. [Available at [http://www.arctic.noaa.gov/reportcard/sea_ice.html.\]](http://www.arctic.noaa.gov/reportcard/sea_ice.html.)

NSIDC, 2014: LASER operational periods. Accessed 21 March 2016. [Available at [https://nsidc.org/data/icesat/laser_op_periods.html.\]](https://nsidc.org/data/icesat/laser_op_periods.html.)

NSIDC, 2016: All about sea ice. Accessed January 2016. [Available at [http://nsidc.org/cryosphere/seoice/index.html.\]](http://nsidc.org/cryosphere/seoice/index.html.)

Nolin, A. W., and Coauthors, 2002: Surface roughness characterizations of sea ice and ice sheets: case studies with MISR data, *IEEE Transactions on Geoscience and Remote Sensing*, **40**, 1605–1615, doi: 10.1109/TGRS.2002.801581.

Office of the Secretary of Defense, 2013: Arctic strategy. [Available online at [http://www.defense.gov/pubs.2013_Arctic_Strategy.pdf.\]](http://www.defense.gov/pubs.2013_Arctic_Strategy.pdf.)

Parkinson, C. L., and W. M. Washington, 1979: A large-scale numerical model of sea ice. *J. Geophys. Res.*, **84**, 311–337, doi:10.1029/JC084iC01p00311.

Perovich, D. K., 1996: The optical properties of sea ice. *U.S. Army Corps of Engineers Cold Regions Research and Engineering Laboratory*, **96-1**, 25.

Perovich, D. K. and C. Polashenski, 2012: Albedo evolution of seasonal Arctic sea ice. *The Cryosphere*, **39**, L08501, doi: 10.1029/2012GL051432.

Perovich, D. K., and Coauthors, 2007: Increasing solar heating of the Arctic Ocean and adjacent seas, 1979–2005: Attribution and role in the ice-albedo feedback. *Geophysical Research letters*, **34**, L19505, doi: 10.1029/2007GL031480.

Perovich, D. K., and Coauthors, 2015: Arctic report card. Accessed March 2016. [Available at [http://www.arctic.noaa.gov/reportcard/sea_ice.html.\]](http://www.arctic.noaa.gov/reportcard/sea_ice.html.)

Perovich, D. K., and J. A. Richter-Menge, 2009: Loss of sea ice in the Arctic. *Ann. Rev. Mar. Sci.*, **1**, 417–441, doi:10.1146/annurev.marine.010908.163805.

Perovich, D. K., and M. Sturm, 2014: Interdecadal changes in snow depth on Arctic sea ice. *Journal of Geophysical Research: Oceans*, **119**, 5395–5406, doi:10.1002/2014JC009985.

Priestley, M. B., 1981: *Spectral Analysis and Time Series*. Academic Press, 104–216 pp.

Richter-Menge, J. A., and S. L. Farrell, 2013: Arctic sea ice conditions in spring 2009–2013 prior to melt. *Geophys. Res. Lett.*, **40**, 5888–5893, doi:10.1002/2013GL058011.

Roberts, A., and Coauthors, 2015: Simulating transient ice-ocean Ekman transport in the Regional Arctic System Model and Community Earth System Model. *Annals of glaciology*, **56**, 211–228, doi: 10.3189/2015AoG69A760.

Rothrock, D. A. and A. S. Thorndike, 1980: Geometric properties of the underside of sea ice. *Journal of Geophysical Research*, **85**, 3955–3963, doi: 10.1029/JC085iC07p03955.

Rothrock, D. A., and A. S. Thorndike, 1984: Measuring the sea ice floe size distribution, *J. Geophys. Res.*, **89**, 6477–6486.

Schutz, B. E., H. J. Zwally, C. A. Shuman, D. Hancock, and J. P. DiMarzio, 2005: Overview of the ICESat mission. *Geophys. Res. Lett.*, **32**, 1–4, doi:10.1029/2005GL024009.

Schweiger, A., R. Lindsay, J. Zhang, M. Steele, H. Stern, and R. Kwok, 2011: Uncertainty in modeled Arctic sea ice volume. *J. Geophys. Res.*, **116**, C00D06, doi:10.1029/2011JC007084.

Showstack, R., 2013: Pentagon strategy recognizes need for increased research in the Arctic. *Eos. Trans. Am. Geophys. Union*, **94**, 485–486, doi:10.1002/2013EO500002.

Singarayer, J. S., J. L. Bamber, and P. J. Valdes, 2006: Twenty-first-century climate impacts from a declining Arctic sea ice cover. *J. Clim.*, **19**, 1109–1125, doi:10.1175/JCLI3649.1.

Smith, L. C. and S. R. Stephenson, 2013: New Trans-Arctic shipping routes navigable by midcentury. *Proceedings of the National Academy of Sciences*, **110**, 1191–1195, doi: 10.1073/pnas.1214212110.

Smith, R., J. Dukowicz, and R. Malone, 1992: Parallel ocean general circulation modeling. *Physical D.*, **60**, 38–61.

Sprott, J. C, 2003: *Chaos and Time-Series Analysis*. Oxford University Press. 226–229, pp.

Stroeve, J. C., V. Kattsov, A. Barrett, M. Serreze, T. Pavlova, M. Holland, and W. N. Meier, 2012: Trends in Arctic sea ice extent from CMIP5, CMIP3 and observations. *Geophys. Res. Lett.*, **39**, L16502, doi:10.1029/2012GL052676.

Studinger, M., L. Koenig, S. Martin, and J. Sonntag, 2010: Operation IceBridge: Using instrumented aircraft to bridge the observational GAP between icesat and ICESAT-2. *International Geoscience and Remote Sensing Symposium (IGARSS)*, **2010**, 1918–1919, doi: 10.1109/IGARSS.2010.5650555.

Task Force Climate Change /Chief of Naval Operations, 2014: U.S. Navy Arctic Roadmap 2014–2030, 43 pp.

Taylor, K. E., 2001: Summarizing multiple aspects of model performance in a single diagram. *Journal of Geophysical Research*, **106**, 7183–7192, doi: 10.1029/2000JD900719.

Teleti, P. R., and A. J. Luis, 2013: Sea ice observations in polar regions: Evolution of. *International Journal of Geosciences*, **4**, 1031–1050, doi:10.4236/ijg.2013.47097.

Tilling, R. L., A. Ridout, A. Shepherd, and D. J. Wingham, 2015: Increased Arctic sea ice volume after anomalously low melting in 2013, *Nat. Geosci.*, **8**, 643–646, doi:10.1038/ngeo2489.

Thomson, R. E., and W. J. Emery, 2014: *Data Analysis Methods in Physical Oceanography*. Elsevier, 269–505 pp.

Thorndike, A. S., D. A. Rothrock, G. A. Maykut, and R. Colony, 1975: Thee. *J. Geophys. Res.*, **80**, 4501–4513, doi:10.1029/JC080i033p04501.

Tsamados, M., D. L. Feltham, and A. V. Wilchinsky, 2013: Impact of a new anisotropic rheology on simulations of Arctic Sea ice. *J. Geophys. Res. Ocean.*, **118**, 91–107, doi:10.1029/2012JC007990.

Turner, A. K., and E. C. Hunke, 2015: Impacts of a mushy-layer thermodynamic approach in global sea-ice simulations using the CICE sea-ice model, *J. Geophys. Res. Oceans*, **120**, 1253–1275, doi:10.1002/2014JC010358.

Turner, A. K., E. C. Hunke, and C. M. Bitz, 2013: Two modes of sea-ice gravity drainage: A parameterization for large-scale modeling. *J. Geophys. Res. Ocean.*, **118**, 2279–2294, doi:10.1002/jgrc.20171.

United Nations, 2016: Submissions, through the Secretary-General of the United Nations, to the Commission on the Limits of the Continental Shelf, pursuant to article 76, paragraph 8, of the United Nations Convention on the Law of the Sea of 10 December 1982. Accessed 30 April 2016. [Available at http://www.un.org/depts/los/clcs_new/commission_submissions.htm]

United Nation Environment Programme, 2016: Arctic Region. Accessed March 2016. [Available at <http://www.unep.org/regionalseas/programmes/independent/arctic/.>]

U.S. Department of State, 2016: U.S. Chairmanship of the Arctic Council. Accessed on April 12, 2016. [Available at <http://www.state.gov/e/oes/ocns/opa/arc/uschair/>.]

United States Energy Information Administration, 2016: Arctic oil and natural gas resources. Accessed March 2016. [Available at <https://www.eia.gov/todayinenergy/detail.cfm?id=4650>.]

Von Storch, H. and F. Zwiers, 1999: *Statistical Analysis in Climate Research*. Cambridge University Press, 112–118 pp.

Wadhams, P., 2000: *Ice in the ocean*. Gordon and Breach Science Publishers, 37–54 pp.

Wadhams, P. and N. R. Davis, 1994: The fractal properties of the underside of Arctic Sea Ice. *Transactions on the Built Environment*, **5**, 353–363.

Wall Street Journal, 2015: The Arctic front in the battle to contain Russia. Accessed 2016. [Available at <http://www.wsj.com/articles/the-real-arctic-threat-1441149448>.]

Wall Street Journal, 2016a: U.S. Navy begins Arctic exercise amid stepped-up criticism of Russia. Accessed on 05 May 2016. [Available at <http://blogs.wsj.com/brussels/2016/03/02/u-s-navy-begins-arctic-exercise-amid-stepped-up-criticism-of-russia/>]

Wall Street Journal, 2016b: The real Arctic threat. Accessed 2016. [Available at <http://www.wsj.com/articles/the-arctic-front-in-the-battle-to-contain-russia-1457478393>.]

Warren, S. G., I. G. Rigor, N. Untersteiner, V. F. Radionov, N. N. Bryazgin, Y. I. Aleksandrov, and R. Colony, 1999: Snow depth on Arctic sea ice. *Journal of Climate*, **12**: 1814 - 1829. doi: [http://dx.doi.org/10.1175/1520-0442\(1999\)012%3C1814:SDOASI%3E2.0.CO;2](http://dx.doi.org/10.1175/1520-0442(1999)012%3C1814:SDOASI%3E2.0.CO;2).

Webster, M. a., I. G. Rigor, S. V. Nghiem, N. T. Kurtz, S. L. Farrell, D. K. Perovich, and M. Sturm, 2014: Interdecadal changes in snow depth on Arctic sea ice. *J. Geophys. Res. Ocean.*, **119**, 5395–5406, doi:10.1002/2014JC009985.

Weiss, J., 2001: Fracture and fragmentation of ice: A fractal analysis of scale invariance. *Eng. Fract. Mech.*, **68**, 1975–2012, doi:10.1016/S0013-7944(01)00034-0.

White House, 2013: National strategy for the Arctic Region. [Available online at http://www.whitehouse.gov/sites/default/files/docs/nat_arctic_strategy.pdf].

WHOI, 2010: Jack Cook illustration of Arctic currents. Accessed 01 April 2016. [Available at <http://www.whoi.edu/vanishingarctic/page.do?pid=47395>.]

Wilks, D. S., 2006: *Statistical Methods in the Atmospheric Sciences Second Edition*. Elsevier, 27 pp.

Yi, D. and H. J. Zwally. 2009, 2014-04-15. *Arctic Sea Ice Freeboard and Thickness, Version 1*. [NSIDC-0393]. Boulder, Colorado USA. NSIDC: National Snow and Ice Data Center. doi: <http://dx.doi.org/10.5067/SXJVJ3A2XIZT>. Date Accessed: March 2016.

Zwally, H. J., and Coauthors, 2002: ICESat's Laser measurements of polar ice, Atmosphere, Ocean, and Land. *Journal of Geodynamics*, **34**, 405–445, doi: 10.1016/S0264-3707(02)00042-X.

Zwally, H. J., D. Yi, R. Kwok, and Y. Zhao, 2008: ICESat measurements of sea ice freeboard and estimates of sea ice thickness in the Weddell Sea. *Journal of Geophysical Research* **113**, C02S15, doi: 10.1029/2007JC004284.

Zygmuntowska, M., P. Rampal, N. Ivanova, and L. H. Smedsrud, 2014: Uncertainties in Arctic sea ice thickness and volume: New estimates and implications for trends. *Cryosphere*, **8**, 705–720, doi:10.5194/tc-8-705-2014.

INITIAL DISTRIBUTION LIST

1. Defense Technical Information Center
Ft. Belvoir, Virginia
2. Dudley Knox Library
Naval Postgraduate School
Monterey, California